5-2003

“Applications of Coherent Electron Beams

Alexander Erwin Thesen
University of Tennessee - Knoxville

To the Graduate Council:

I am submitting herewith a dissertation written by Alexander Erwin Thesen entitled ""Applications of Coherent Electron Beams." I have examined the final electronic copy of this dissertation for form and content and recommend that it be accepted in partial fulfillment of the requirements for the degree of Doctor of Philosophy, with a major in Physics.

Dr. Marianne Breinig, Major Professor

We have read this dissertation and recommend its acceptance:

Dr. John J. Quinn, Dr. James R. Thompson, Dr. David C. Joy

Accepted for the Council:

Carolyn R. Hodges

Vice Provost and Dean of the Graduate School

(Original signatures are on file with official student records.)

To the Graduate Council:

I am submitting herewith a dissertation written by Alexander Erwin Thesen entiltled "Applications of Coherent Electron Beams". I have examined the final electronic copy of this dissertation for form and content and recommend that it be accepted in partial fulfillment of the requirement for a degree of Doctor of Philosophy, with major in Physics.

Dr. Marianne Breinig
Major Professor

We have read this thesis
and recommend its acceptance:

Dr. John J. Quinn

Dr. James R. Thompson

Dr. David C. Joy

Accepted for the Council:

Dr. Anne Mayhew
Vice Provost and
Dean of Graduate Studies

(Original signatures are on file with official student records.)

Applications of Coherent Electron Beams

Alexander E. Thesen

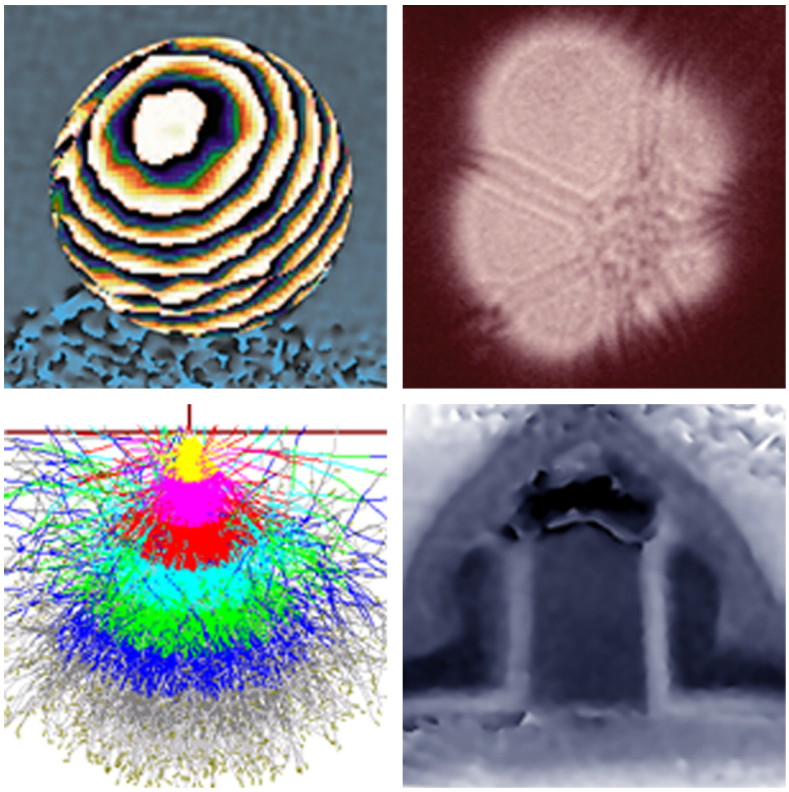

A Dissertation Presented for the
Doctor of Philosophy Degree

The University of Tennessee, Knoxville
May, 2003

Acknowledgments

During the years of my dissertation I had the great fortune of to work with an exceptional scientist and educator, my advisor Professor David C. Joy. I cannot thank him enough for all the encouragement and help I received and the opportunities he has opened up for me. I also had the great pleasure to work hand in hand with Dr. Bernhard Frost, whom I want to thank for sharing his profound knowledge of electron holography with me and helping me with his advice and guidance numerous times.
I greatly benefited from the many stimulating discussions with the scientists at the High Temperature Materials Laboratory at the Oak Ridge National Laboratory, who have taught me so much. I would like to thank a few of these colleagues directly: First and foremost Dr. Lawrence Allard, Larry Walker, Dr. Douglas Blom, Dr. Harry Meyer, Dr. Ian Anderson, Dr. Karren More, Dr. Edgar Völkl (now at nLine), Dr. Frank Kahl (now at CEOS GmbH), Professor Emeritus Wilbur Bigelow, Professor Emeritus Harald Rose, who was visiting our group in 2001, Shawn Reeves, Dorothy Coffey, and Carolyn Wells.
During my thesis work I benefited from my interaction with many exceptional scientists in the semiconductor industry. I acknowledge the continued support our group and me have received from Dr. Bryan Tracy at AMD, who has helped me in so many ways. In his group I also want to acknowledge Sheila Morgan, Liliana Thompson, Ashik Ali, Dr. Ercan Adem, and many others. I thank SRC and International SEMATECH for their continued financial support, and I especially want to acknowledge the help from Dr. Alain Diebold, Dr. Brendan Foran, and Dr. Robin Tichy at SEMATECH. At ST Microelectronics I thank Geoffroy Auvert for sharing his samples. I gratefully acknowledge the help I received from Professor James Wittig at Vanderbilt University, who shared his samples and made his FIB available to me.
At the University of Tennessee I had the pleasure of working together with a group of enthusiastic young scientists among them Dr. Yeong-Uk Ko, Young Choi, Jing He, Satya Prasad, Dr. Carolyn Joy, Dr. John Dunlap, Xiaohu Tang, Jon Lillestolen, Toshihide Agemura, who was a visiting scientist from Hitachi High Technology, Steven Randolph, Yuepeng Deng, Jason Fowlkes, and Professor Phillip Rack. At the University of Tennessee I also want to thank my committee members Professor John Quinn, Professor James Thompson, and especially my committee chair Professor Marianne Breinig. Much of this work would not have been possible without the dedicated help of our group secretary Jennifer Trollinger, who I thank very much.
My deepest thanks go to my wife Asmaâ and my parents for their trust, encouragement, and support in so many ways.

This research was sponsored in part by the Assistant Secretary for Energy Efficiency and Renewable Energy, Office of Transportation Technologies, as part of the High Temperature Materials Laboratory User Program at the Oak Ridge National Laboratory, Oak Ridge, Tennessee, managed by UT-Battelle LLC for the U.S. Department of Energy under contract DE-AC05-00OR22725. It was also supported by International SEMATECH with Dr. A. Diebold (holography project) and Dr. H. Bogardus (point projection microscope project) as contract monitors. Additional funds were provided by SRC with Dr. D. Herr as the project monitor under contract 99-LJ-413.004.

Abstract

The use of coherent beams for interferometric measurements has gained great popularity in light optics over the last several decades. The availability of coherent electron sources has now opened the door to apply the concept of holographic imaging in many new areas. Off-axis holograms can now be recorded in field emission transmission electron microscopes equipped with the electron optical equivalent of a biprism. This technique allows the accurate retrieval of phase and amplitude of the electron wave, which has been transmitted through a sample. The sensitivity of the phase of the electron wave to electrical potentials makes it possible to map out potential distributions on the specimen with sub-micron resolution.

As part of this thesis, off-axis electron holography has been applied to map out the small potential changes, which occur over pn-junctions in doped semiconductor devices. To this end a special alignment of the electron microscope has been devised, and new methods for preparing electron transparent samples of semiconductor devices, specially tailored for electron holography, have been developed. Also, new ways to improve on the existing electron biprism technology have been investigated. The observed voltage signals could be linked to active dopants in silicon by annealing experiments, and the viability of the method for voltage profiling of real-world semiconductor devices has been demonstrated.

The use of coherent electron emitters also allows the recording of in-line electron holograms in a lens-less projection microscope at ultra-low beam energies. Such a point projection microscope, which is capable of recording in-line holograms in transmission imaging, has been built. With defect review on silicon wafers as a possible application for in-line electron holography in mind, the feasibility of point projection imaging in a reflection geometry has been demonstrated. In this context the elastic backscattered yield for electrons in different materials and under different geometries has been calculated using Monte Carlo simulations. Several problems, which occur in reflection imaging, are pointed out and possible solutions are presented.

Contents

1 Introduction **1**
1.1 Why Use Coherent Electron Beams? . . . 1
1.1.1 The Beginning of Optical Interferometry . . . 1
1.1.2 Off-Axis Electron Holography . . . 2
1.1.3 In-Line Electron Holography . . . 3
1.2 Outline . . . 4

2 Off-Axis Electron Holography **6**
2.1 Hologram Formation with the Möllenstedt Biprism . . . 6
2.2 Coherence of Electron Waves . . . 9
2.2.1 Coherent Electron Beams . . . 9
2.2.2 Coherence of Scattered Electrons . . . 12
2.2.3 Coherence and Illumination in the Electron Microscope . . . 16
2.3 Field Emission of Electrons . . . 17
2.4 The Möllenstedt Biprism . . . 20
2.5 Electric and Magnetic Fields . . . 25
2.6 The Inner Potential of Crystals . . . 27
2.7 Hologram Reconstruction . . . 30
2.7.1 The Basic Reconstruction Process . . . 30
2.7.2 Using Reference Holograms . . . 31
2.8 Recording of Holograms . . . 32
2.9 Artifacts in Electron Holography . . . 35
2.9.1 Fresnel Fringes . . . 36
2.9.2 Fringe Branching . . . 37
2.9.3 Diffraction Effects . . . 38

3 In-line Electron Holography **41**
3.1 Low Voltage In-Line Electron Holography . . . 41
3.2 In-Line Hologram Formation . . . 43
3.3 The Reconstruction Problem . . . 46
3.4 The Point Projection Microscope - Experimental Setup . . . 48
3.5 Reflection Mode . . . 50
3.5.1 Monte Carlo Simulations of Elastic Electron Backscattering . . . 51
3.5.2 Problems and Solutions for Reflection Imaging . . . 56
3.5.3 Outlook – Possible Application for Defect Review . . . 58

4 Off-Axis Holography in the Field Emission TEM **61**
4.1 The HF-2000 Field Emission TEM 61
4.2 Low Magnification Holography Mode 63
4.3 Medium Magnification Holography Mode 64

5 TEM Sample Preparation **68**
5.1 Requirements for Holography Samples 68
5.1.1 Optimum Sample Thickness 68
5.1.2 Geometrical Limitations 69
5.1.3 Surface Amorphization 70
5.2 Methods for Sample Preparation 70
5.2.1 De-Layering of Semiconductor Samples 70
5.2.2 Tripod Polishing 71
5.2.3 Dimpling and Ion Polishing 72
5.2.4 Sample Preparation with Focused Ion Beam Systems 74

6 Holography on Doped Semiconductor Devices **80**
6.1 Voltage Contrast in Doped Semiconductor Devices 80
6.2 Different Approaches to Thickness Correction 84
6.2.1 Thickness Correction using the Amplitude Image 84
6.2.2 Extrapolation 86
6.2.3 Convergent Beam Electron Diffraction 86
6.2.4 Electron Energy Loss Spectroscopy 88
6.3 A Brief Overview of CMOS Technology 89
6.4 Assessing the Sample Quality 91
6.5 Activation of Dopants in Silicon 93
6.6 A Real World Example 94
6.7 Alternative EM Methods for 2D Dopant Profiling 99

7 Summary and Outlook **101**
7.1 Room for Improvement 102
7.2 Limitations 104

References **105**

Appendices **115**

Appendix A: Fresnel Fringe Removal **117**

Appendix B: Thickness Correction **130**

Appendix C: Removal of Linear Phase Changes **132**

Appendix D: Index **134**

Vita 136

List of Tables

2.1 Comparison of different electron sources 18

4.1 Typical parameters for low magnification setup 64
4.2 Typical parameters for improved low magnification setup 65

6.1 Summary of 2D dopant profiling requirements 81

List of Figures

1.1 Comparison between a conventional bright field image and a phase image . 4

2.1 Hologram formation with the Möllenstedt biprism 7
2.2 Hologram formation in the presence of a sample 8
2.3 Biprism interferometer. 10
2.4 Fringe contrast dependence on the source size. 11
2.5 Field emission of electrons 19
2.6 Energy distributions of different emission processes 21
2.7 How to make an electron biprism 22
2.8 The electron biprism after Möllenstedt 23
2.9 The plate biprism 23
2.10 Defocus effect of the plate biprism 24
2.11 Potential distribution about the plate biprism. 25
2.12 Change in fringe spacing - plate versus fiber biprism 26
2.13 Phase dependence of the electron wave on the enclosed magnetic flux 28
2.14 Thickness map of a silicon wedge 29
2.15 Reconstruction of holograms 31
2.16 Removal of phase jumps 32
2.17 Phase image from an empty hologram 33
2.18 Correct centering of the sideband 33
2.19 Number of fringes required to resolve two points. 34
2.20 Relationship between noise and recording time 35
2.21 Dependence on the interference width on the biprism excitation 36
2.22 Elimination of Fresnel Fringes 37
2.23 Artifacts caused by fringe branching 38
2.24 Thickness fringes caused by diffraction effects 39

3.1 Operating principle of the point projection microscope 42
3.2 Series of point projection micrographs 43
3.3 Simple point projection interference patterns 45
3.4 Numerical simulation of point projection imaging 46
3.5 In-line hologram reconstruction 47
3.6 Setup of the point projection microscope 49
3.7 Basic geometry in reflection mode 50
3.8 Electron trajectory in a solid 51

3.9 Dielectric loss function of silicon and copper 54
3.10 Inelastic mean free paths of silicon, copper, platinum, and gold 55
3.11 Monte Carlo simulation of elastically backscattered electrons - angular dependence 55
3.12 Monte Carlo simulation of elastically backscattered electrons - energy dependence 56
3.13 Reflection images at off-normal incidence 57
3.14 First reflection images in the PPM 58
3.15 Prospective electron gun for the PPM 59

4.1 The HF-2000 field emission TEM 62
4.2 Ray paths for low magnification holography 63
4.3 Holography in the normal operation mode of the TEM 65
4.4 Ray paths for medium magnification holography 67

5.1 Polishing fixtures 71
5.2 Sample in a dimpler 72
5.3 Sample preparation by dimpling 73
5.4 Single and dual beam FIB system 75
5.5 Silicon lattice damage from platinum deposition 76
5.6 Curtaining effects in FIB-milled samples 77
5.7 FIB-milled sample for holography (version 1) 79
5.8 FIB-milled sample for holography (version 2) 79

6.1 The pn step-junction 82
6.2 Dependence of the voltage drop over a pn-junction on the dopant concentration 83
6.3 Phase change of an electron wave penetrating a doped semiconductor . . . 83
6.4 Elimination of thickness contributions to the phase 1 85
6.5 Elimination of thickness contributions to the phase 2 87
6.6 CMOS device process flow 89
6.7 Sample charging 92
6.8 Differential milling or doping? 93
6.9 Activation of boron doped silicon 94
6.10 Phase image of a transistor. 96
6.11 Phase image after linear thickness correction 96
6.12 Raw data and fit to a phase image 97
6.13 Voltage and carrier density profile 98
6.14 Secondary electron doping contrast in the SEM. 100

7.1 Gas injector for e-beam etching 102
7.2 Silicon dioxide etched with e-beam 103

In the land of the blind the one-eyed man is king.

George Bernhard Shaw

1 Introduction

1.1 Why Use Coherent Electron Beams?

As conventional imaging techniques merely record intensity distributions, all information about the phases of the recorded waves is lost. In order to obtain a complete record of a wave field it is necessary to convert the phase information into variations of intensity. One way of doing this is by using coherent illumination and producing on the recording medium an interference pattern between the wave field, which has been scattered by the illuminated object, and an unscattered reference wave. The interference pattern then contains a complete record of the phase and amplitude of the wave front. This record is called a *hologram*.

1.1.1 The Beginning of Optical Interferometry

Gabor's goal, when he first proposed holographic imaging, was to increase the resolution, that can be obtained in an electron microscope. [35] As it is difficult to correct for spherical aberrations of electron lenses, he suggested recording the scattered field of an object illuminated by electrons and to reconstruct the image from this record with visible light. Lens aberrations could then be corrected for during the reconstruction process. He demonstrated his idea by recording in-line holograms using visible light and presenting the reconstruction of the recorded interference pattern. Optical holography was not successful initially as the twin image problem and the lack of highly coherent light sources produced holographic images of poor quality. An important step of overcoming these limitations was the invention of the off-axis reference beam technique by Leith and Upatnieks. [59] The wide spread availability of lasers as a highly coherent light source finally resulted in numerous applications for interferometric measurements, in which small displacements to a fraction of a micron can be mapped out. Because a recorded interferogram could be compared to previously stored ones, holography soon became a widely used method in product inspection and quality monitoring. Novel

applications range from high-resolution imaging, information processing, holographic optical elements, security coding, strain analysis, and non-destructive testing. Introductions into the large field of optical interferometry have been compiled by Hariharan [45] and many others. Apart from the great popularity of optical interferometry and the recent developments in using coherent electron beams for a variety of different applications in electron holography, which we will discuss later, the use of coherent beams for interferometrical measurements has been demonstrated in other areas, such as x-ray holography [107] and holographic imaging using neutrons [17].

1.1.2 Off-Axis Electron Holography

Early attempts to produce holograms with an electron microscope were bound to fail because of the lack of both a coherent electron source and the electron optical equivalent of a prism. With Möllenstedt's invention of the electron biprism in 1955 [75] the recording of off-axis electron holograms became possible. With no field emission electron source available, the first biprism interference patterns obtained by Möllenstedt required long exposure times and showed only weak fringe contrast. To improve the quality of the holograms a new interferometer was designed in the following year, which allowed more efficient usage of the available coherent current by astigmatic illumination. Early experiments focused mainly on verifying basic concepts of quantum mechanics. The improved interferometer setup allowed the verification of the famous de Broglie relation $\lambda = h/p$, which was gratefully acknowledged by de Broglie himself in the following letter to Möllenstedt [74]:

Paris, 19 June 1956

Monsieur and dear Colleague,

I was extremely pleased to receive your kind letter and to learn of your beautiful experiments in which you have obtained electron interference by a method analogous to Fresnel's biprism. It was, of course, a great pleasure to see that you have obtained a new and particularly brilliant proof of the formula $\lambda = h/mv$, and I shall not fail to make known your experiments to my students. Thanking you most gratefully for your communication I beg you to accept, Monsieur and dear colleague, the expression of my devoted sentiments,

Louis de Broglie

Further important milestones marked the design of the first electron interference microscope by Rainer Buhl [12] and the experimental verification of the Arahanov-Bohm effect by Akira Tonomura and others [8, 111]. Only recently, with the availability of electron microscopes with coherent field emission type electron sources, electron interferometry has found widespread acceptance in the microscopy community and a variety of different applications have emerged. The group around Hannes Lichte, following the original idea

of Gabor, pioneered the field of using electron holography to correct transmission electron microscope (TEM) micrographs for the spherical aberrations of the electron lenses and extended the point resolution of the microscope to the information limit. [34, 58, 60] Frost and others established electron holography as a technique to observe electric and magnetic fields on a micron scale and to study charging effects. [27, 31, 32, 69] Others have used holography for exact specimen thickness determination, determination of inner potentials or compositional imaging [39, 66, 116, 119], as well as observing magnetic properties of TEM specimens and domain imaging [10, 65, 71, 80]. Recent work by Lehmann has shown that, because it is a true zero-loss imaging technique, off-axis TEM holography could potentially solve the Stobbs factor problem in high resolution microscopy. [57] Finally, very recently the ability of electron holography to map out potential changes caused by active dopants in semiconductors has received great interest as a technique for two-dimensional dopant profiling of semiconductor devices. [26, 70, 72, 90, 109, 110, 117] The work conducted as part of this thesis is meant to advance this young area of dopant profiling, especially with its application to commercial, state-of-the-art semiconductor devices in mind. To this end a medium magnification setup for a field emission electron microscope equipped with a Möllenstedt biprism has been devised and a new, more stable kind of electron biprism has been developed. In addition to this I will present a variety of new methods for TEM sample preparation of semiconductor device specimens, which are especially tailored to the requirements of electron holography. The observed voltage contrast is undoubtedly linked to activated dopants by annealing experiments. Examples of the application of holography to commercial devices will be shown and limitations of the method will be discussed.
Compared to conventional bright-field imaging, the ability of holographic imaging to obtain quantifiable information about the phase and amplitude of the electron wave has opened a wide new area of electron microscopy with many novel applications. Figure 1.1 summarizes several of the many advantages of holographic imaging over conventional TEM bright-field imaging, which will be put to use in this thesis.

1.1.3 In-Line Electron Holography

With the recent availability of highly coherent nanotip field emitters, Gabor's original idea of in-line holography [35] has received new attention in connection with a low-voltage lens-less point projection electron microscope, which was first proposed by Morton and Ramberg in 1939 [79]. In the point projection microscope the electron-transparent sample is located in close proximity to a field-emission emitter and a magnified image of the sample is projected onto a screen a large distance away from the tip. As the magnification is achieved without the use of any lenses the image is free of lens aberrations. Because the electron source is coherent, the image will be an in-line hologram, as proposed by Gabor. Since imaging of samples at ultra low electron beam energies as low as 7 eV has been demonstrated in the point projection microscope, it has attracted interest as a tool for imaging of biological samples and macromolecules, which are severely damaged in conventional microscopes operating at higher

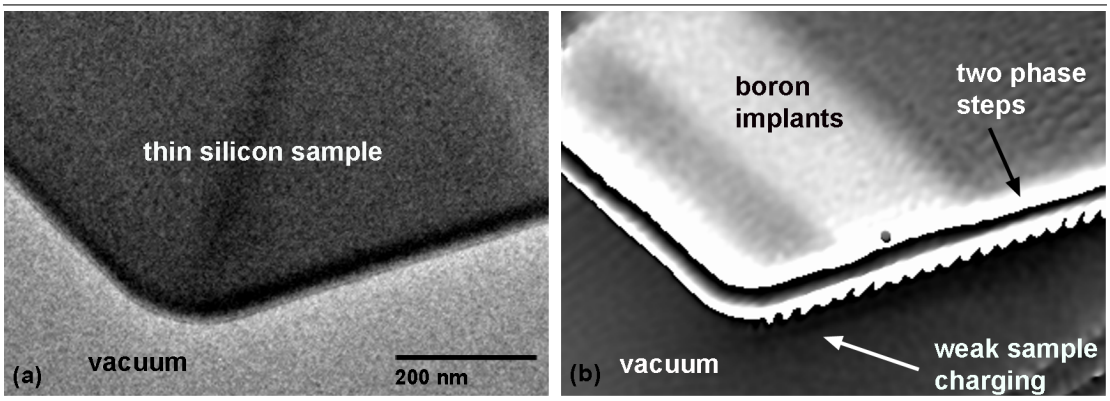

Figure 1.1: Comparison between a conventional bright field TEM image (a) and a phase image obtained by electron holography (b). While the bright field image is almost featureless apart from some diffraction effects and reveals little information about the sample, the phase image, which has been reconstructed from an electron hologram, shows a variety of interesting features: Clearly visible as bright areas across the sample are phase changes of the electron wave due to active boron dopants in the silicon. A faint shadow around the sample edges indicates that the sample is charging up slightly under the beam and that potential distributions reach out into the vacuum. From the two phase jumps along the edges of the specimen a sample thickness of about 150 nm can be estimated.

beam energies.[42, 43, 100, 118] We have successfully built a prototype of such a microscope for transmission imaging, but it is our main goal to develop a setup, which allows projection imaging in a reflection geometry. Such an instrument would be ideally suited for defect review on silicon wafers. The necessary steps in developing the reflection microscope and initial results in reflection imaging mode will be presented in this thesis.

1.2 Outline

In the following chapters the two topic main areas using coherent electron beams will be presented: Off-axis electron holography and in-line electron holography. The main goal will be to demonstrate how these methods can be applied to solve real world problems as they occur in the semiconductor industry. Special attention will be given both to the application of off-axis electron holography as a tool for voltage profiling of doped semiconductor devices and to associated problems such as thin sample preparation for holography.
The following chapter of this thesis will introduce the reader to the basic theory of off-axis electron holography, image reconstruction and the influence of electromagnetic fields and objects on the electron wave. A detailed discussion will explain how the con-

cept of coherence known from light optics transfers into the world of electron optics. The third chapter is dedicated exclusively to in-line holography. In-line hologram formation and the reconstruction problems specific to in-line holography will be discussed. Recent progress in the design of a point projection microscope in both transmission and reflection mode will be presented as well as Monte Carlo studies of elastic backscattering, in order to optimize the reflection microscopy setup. The remaining chapters of the thesis focus exclusively on off-axis holography and its application to voltage profiling of semiconductor devices. Chapter four deals with details of the electron optical setup for off-axis holography in the HF-2000 field emission TEM. Chapter five introduces the reader to TEM sample preparation techniques, which have been developed especially for electron holography as part of this thesis. In chapter six the technique is finally applied to map potential distributions caused by active implants in silicon devices. Examples for the application to voltage profiling of state-of-the-art devices are given. In the final chapter this thesis is concluded with a brief summary and a discussion on future areas of research as well as limitations and problems electron holography may face in the future.

It is the theory that decides what we can observe.

Albert Einstein

Off-Axis Electron Holography 2

In this chapter we will present an introduction into off-axis electron holography in the field emission electron microscope (FE-TEM). Details of hologram formation, recording, and reconstruction will be discussed as well as aspects of coherence of electron beams, electron biprism technology and the interaction of the coherent electron beam with both the specimen and electro-magnetic fields.

2.1 Hologram Formation with the Möllenstedt Biprism

To be capable of generating electron holograms, the microscope must be equipped with an electron biprism, which is capable of splitting the incident beam into two parts and bringing them into interference. We assume that the illumination system of the electron microscope produces a plane electron wave, which travels down the microscope column. In off-axis electron holography typically only one part of the plane wave is transmitted through a sample, which is inserted only half-way into the electron beam, while the other part of the wave continues to travel past the sample through vacuum only. The electron biprism then overlaps these two parts and an interference pattern is formed in an image plane of the microscope. For simplicity we will first describe the generation of the interference pattern with no sample inserted and then later discuss how the presence of the sample changes this pattern.
Let $\psi = e^{ikz}$ be a plane wave traveling towards a biprism, which is located at $z = 0$ and extends in the y-direction (see figure 2.1 (a)). The biprism splits the wave into two parts, $\Psi_\mathrm{l} = e^{ik(z\sin\gamma + x\cos\gamma)}$ on the left side and $\Psi_\mathrm{r} = e^{ik(z\sin\gamma - x\cos\gamma)}$ on the right side. The two parts are deflected towards each other by an angle γ on either side. On a screen a distance z away from the biprism fiber they will form an interference pattern

$$\begin{aligned} I &= |\Psi_\mathrm{l} + \Psi_\mathrm{r}|^2 \\ &= 2\Big(1 + \cos(2kx\cos\gamma)\Big). \end{aligned} \tag{2.1}$$

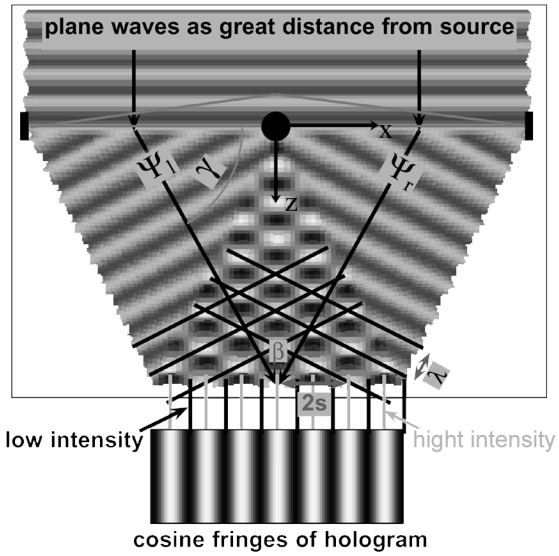

Figure 2.1: Hologram formation with the Möllenstedt biprism. (a) The part of the electron wave traveling on the left side of the fiber Ψ_l is overlapped with the part of the electron wave on the right side Ψ_r. A cosine fringe pattern is formed in the image plane.

The spacing of the interference fringes s is given by

$$s = \frac{\lambda}{2\cos\gamma} = \frac{\lambda}{2\sin(\beta/2)} \approx \frac{\lambda}{\beta}, \tag{2.2}$$

since β is small. The effect of the biprism can also be described by replacing electron source and biprism with two mutually coherent electron sources. These are the sources an observer on the recording plane sees, if he traces back the incident electron rays.
If an object is inserted on the right side of the biprism (figure 2.2), the deflected wave on this side will change to

$$\Psi_\mathrm{r} = A_\mathrm{obj}\, e^{ik(z\sin\gamma - x\cos\gamma) + \phi_\mathrm{obj}} \tag{2.3}$$

and the interference pattern will become

$$I = 1 + A_\mathrm{obj}^2 + 2A_\mathrm{obj}\cos(2kx\cos\gamma + \phi_\mathrm{obj}). \tag{2.4}$$

Here A_obj and ϕ_obj are the amplitude and phase of the electron wave at the exit surface of the sample: $\Psi_\mathrm{obj} = A_\mathrm{obj} e^{i\Phi_\mathrm{obj}}$. According to equation (2.4) the intensity contains information about the phase and the amplitude of the object wave. The changes in phase will shift the the interference fringes while the amplitude impacts the fringe contrast, as shown in the following paragraph. In section 2.7 we will discuss how both amplitude and phase information can be extracted from a hologram given by equation (2.4). If

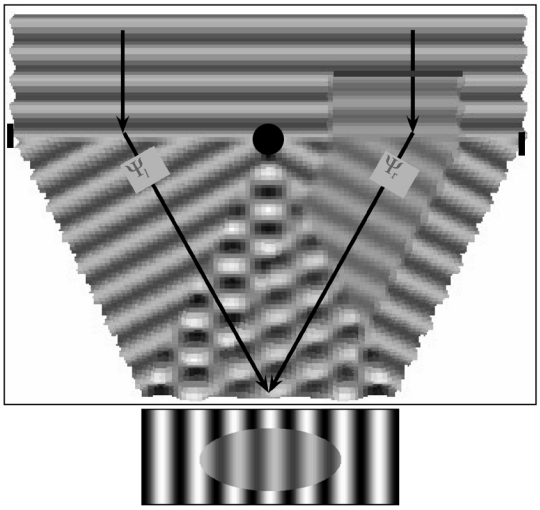

Figure 2.2: The presence of a sample changes the appearance of the fringe pattern. The decrease in wave amplitude behind the sample causes a decrease in fringe contrast. Phase changes due to the sample cause a displacement of the holographic fringes.

the biprism is mounted in an arbitrary direction in the xy-plane, equation (2.4) has to be modified to

$$I(\vec{r}) \;=\; 1 + A_{\mathrm{obj}}^2(\vec{r}) \;+\; 2A_{\mathrm{obj}}(\vec{r}) \cos\Big(2\pi\vec{q}_{\mathrm{c}} \cdot \vec{r} + \Delta\phi(\vec{r})\Big). \tag{2.5}$$

where the vector $\vec{q}_{\mathrm{c}}$ points perpendicular to the direction of the biprism in the xy-plane and is of magnitude $|\vec{q}_{\mathrm{c}}| \;=\; 2\cos\gamma/\lambda$. We also replaced the phase of the object wave ϕ_{obj} by the phase difference $\Delta\phi = \phi_{\mathrm{obj}} - \phi_{\mathrm{ref}}$ to account for any phase changes the reference wave could encounter.

We define the fringe contrast of the interference fringes as

$$C \;=\; \frac{I_{\mathrm{max}} - I_{\mathrm{min}}}{I_{\mathrm{max}} + I_{\mathrm{min}}}. \tag{2.6}$$

Here I_{max} denotes the intensity at the fringe maximum, i.e. the intensity if the cosine function in equation (2.4) becomes 1, and I_{min} the minimum intensity, with the cosine becoming -1. With no object present the fringe contrast evaluates to $C_{\mathrm{no\ object}} = 1$ using equation (2.1), while with an object present the fringe contrast deteriorates to

$$C \;=\; \frac{2A_{\mathrm{obj}}}{1 + A_{\mathrm{obj}}^2} \tag{2.7}$$

using equation (2.4). So far we have assumed that the incident electron wave is perfectly coherent. This is not the case in reality and the fringe contrast will be weaker than described by equation (2.7). The following section will address this issue.

2.2 Coherence of Electron Waves

2.2.1 Coherent Electron Beams

Two waves are called coherent if they are capable of interference. The capability of interference between two waves is characterized by the visibility of the interference effect. Whether or not such an interference effect can be observed depends on the time dependence of the phase relation of the two waves.
While in light optics lasers provide beams, in which photons from different points of the source have fixed phase relations with one another over long periods of time, no such source is available for electron beams. In order to generate a bright beam of electrons modern electron microscopes use field emission sources. In such a field emission source electrons are extracted from the conduction band of a solid through a tunneling process. As the wave functions of different electrons in the conduction band of a solid are believed to have chaotic phase relations [122], the electrons emitted from the source will have no fixed phase relationship, i.e. they are mutually incoherent. Moreover no more than two electrons have the same energy in the conduction band according to the Pauli principle. We can conclude that *electrons emitted from a source with the same as well with different energies have no fixed phase relationships, i.e. they are mutually incoherent. No interference between electrons emitted from two different points of such a source can be observed.* This can be summarized in Dirac's words: *"Each electron interferes only with itself."*
Such an electron source compares to a hot light bulb, where photons are emitted from different oscillators with no fixed phase relations, equipped with an energy filter, which limits the emitted wavelengths to a narrow range. Interference effects from such a source can only be observed if it is virtually split into two sources using, for example, a biprism. The interference pattern generated this way is the sum of all interference patterns of all mutually incoherently emitted electron waves. Let the function $i_s(\xi, k)$ describe the normalized intensity distribution of the source, where ξ denotes the coordinate in the source plane, x are the coordinates in the plane of the hologram, and k is the wave vector of the emitted electron (see figure 2.3). The resulting intensity distribution is then given by summing up equation (2.1) for each point of the source:

$$I \;=\; 2 \iint i_s(\xi, k) \left(1 + \cos(k\beta x + \theta(\xi, q))\right) d\xi dk. \tag{2.8}$$

Here we used equation (2.2) to substitute $\cos\gamma$, and θ gives the lateral position of the resulting interference fringes with respect to the optical axis. To simplify this expression we assume that each point of the source ξ emits the same spectrum $s(k)$, which we assume to be narrowly peaked about a value k_0. We can then factorize i_s into

$$i_s(\xi, k) \;=\; i(\xi)\, s(k), \qquad \text{with } \int i(\xi) d\xi = 1, \int s(k) dk = 1. \tag{2.9}$$

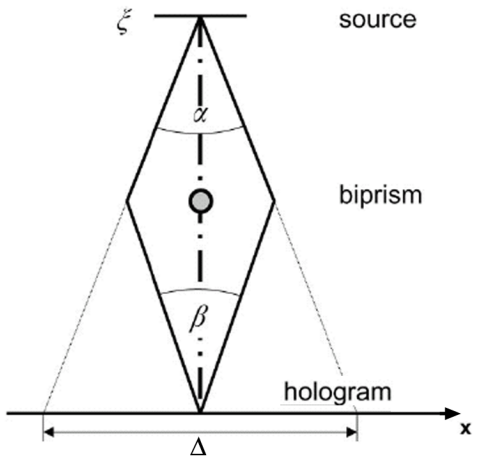

Figure 2.3: Sketch of a biprism interferometer. The electron paths shown define the angles α and β. The angle α gives the spatial coherence, i.e. the diameter Δ of the coherently illuminated area, while β determines the fringe spacing and, in product with the coordinate x, the temporal coherence.

Following Lichte [62] the resulting interference pattern can then be written as

$$I = 2\left(1 + \int i(\xi,k) \int s(k)\cos(k\beta x + \theta)\right) d\xi dq \tag{2.10}$$

$$= 2\Big(1 + |\mu|\cos(k_0\beta x + \delta)\Big). \tag{2.11}$$

We define

$$\mu = |\mu| e^{i\delta} = \mu_{\mathrm{sc}}\,\mu_{\mathrm{tc}} \tag{2.12}$$

as the complex degree of coherence. It is the product of spatial coherence μ_{sc} and temporal coherence μ_{tc}, which are related to the spatial and spectral intensity distribution by Fourier transformations according to

$$\mu_{\mathrm{sc}}(\alpha) = |\mu_{\mathrm{sc}}| e^{i\delta_{\mathrm{sc}}} = FT[i(\xi)] \tag{2.13}$$

$$= \int i(\xi) e^{ik_0\alpha\xi}\, d\xi \tag{2.14}$$

and

$$\mu_{\mathrm{tc}}(x) = |\mu_{\mathrm{tc}}| e^{i\delta_{\mathrm{tc}}} = FT[s(\kappa)] \tag{2.15}$$

$$= \int s(\kappa) e^{i\kappa\beta x}\, d\kappa \tag{2.16}$$

with $\kappa = k - k_0$ and x, α, and β defined in figure 2.3. [62] This is the van Cittert-Zernike theorem, which is well known from light optics. It relates the size and shape of a source

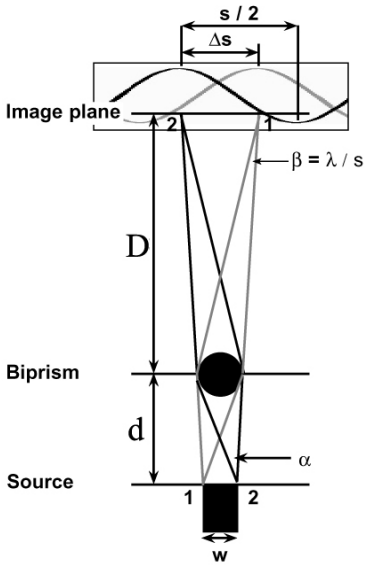

Figure 2.4: A source of width w illuminates a biprism under an angle α. A distance D away from the biprism a hologram can be observed on a recording plane with fringe spacing s.

as well as its spectral intensity distribution to its coherence. Its validity for electron sources has been tested experimentally by Burge et al. [13]. The theorem states that the spatial coherence increases with decreasing source size and the temporal coherence increases with decreasing width of the spectral distribution of the source. A detailed derivation of the theorem can be found in optics textbooks such as Born and Wolf [11]. To understand its implications it is instructive to work out the following simple example: Let us consider a source, which consists of an array of emitting points of length w as shown in figure 2.4. The biprism is located a distance d away. An image or recording plane is located a distance D below the biprism. As seen from the source the biprism subtends an angle α, and as seen from the recording plane, an angle β. Interference fringes

$$I_{\mathrm{p}}(x) = \cos\left(\frac{2\pi}{s}(x+\varphi)\right) \tag{2.17}$$

caused by different source points will have their maxima at different positions $x = -\varphi$. Let the maxima of the interference fringes caused by the leftmost source point be spaced from the ones caused by the rightmost by a distance Δs on the recording plane. To account for the contribution of every source point in the image plane we need to integrate over all possible angles φ.

$$I = \int_{-\Delta s/2}^{\Delta s/2} I_{\mathrm{i}} = \frac{s}{\pi}\sin\left(\pi\frac{\Delta s}{s}\right)\cos\left(\frac{2\pi}{s}x\right) + \Delta s \tag{2.18}$$

Note that the resulting intensity is again a cosine fringe pattern. We can now calculate the fringe contrast as defined in (2.6):

$$C = |\mu_{\mathrm{sp}}| = \frac{\sin(\pi\frac{\Delta s}{s})}{\pi\frac{\Delta s}{s}} \tag{2.19}$$

Using equation (2.2) and from geometrical considerations $d/D = \beta/\alpha$ and $d/D = w/\Delta s$ we obtain

$$\alpha w = \lambda\frac{\Delta s}{s} \tag{2.20}$$

and therefore

$$|\mu_{\mathrm{sp}}| = \frac{\sin(\pi\frac{\alpha w}{\lambda})}{\pi\frac{\alpha w}{\lambda}}. \tag{2.21}$$

We can obtain the same result using the van Citter-Zernike theorem (2.13) by calculating the Fourier transformation of the source described above:

$$\mu_{\mathrm{sc}}(\alpha) = \int_{-w/2}^{w/2} 1\, e^{ik\alpha\xi}\, d\xi \tag{2.22}$$

$$= \frac{2}{k\alpha}\sin\left(\frac{k\alpha w}{2}\right)$$

$$= \frac{\sin(\pi\frac{\alpha w}{\lambda})}{\pi\frac{\alpha w}{\lambda}}. \tag{2.23}$$

2.2.2 Coherence of Scattered Electrons

We now have to consider how the coherence of electrons is affected through interactions with the specimen. The following questions arise:

1. Can electrons interfere with each other after they have been scattered elastically?
2. Can electrons interfere with each other after they have been scattered inelastically?
3. Can we observe interference between unscattered or elastically scattered electrons of energy E and electrons of energy $E-\Delta E$, which have lost an amount of energy ΔE in an inelastic scattering event?
4. Can an electron of energy $E-\Delta E$, which has lost an amount of energy ΔE in an inelastic event, interfere with an unscattered electron of energy $E-\Delta E$, which has been emitted from the same source as the other electron, assuming the energy spread of the source is large enough?

These questions have been subject of a lively and controversial discussion in the literature and many different opinions have been voiced. [16, 23, 62, 104, 122] Part of the problem causing the confusion is that some authors try to answer the questions using classical arguments while others attempt a quantum mechanical treatment, and even

mixtures of both approaches can be found. In the following I will mainly argue similar to the treatment of Zhou [122] and assume a specimen, which can be in three possible states: A ground state $|0\rangle$ and two excited states $|1\rangle$ and $|2\rangle$. As the two excited states have different energies from the ground state, they are orthogonal to the ground state, $\langle 0|1\rangle = \langle 0|2\rangle = 0$, but not necessarily orthogonal to each other. We will neglect in the following all transitions from the excited states into the ground state such as emission of X-rays or any other decay processes. Initially the system consists of the specimen in the ground state $|0\rangle$ and the incident electron wave Ψ_{in}. The final state of the system, after the scattering, is given by

$$\Psi_{\text{final}} = C_0\Psi_0(r)|0\rangle + C_1\Psi_1(r)|1\rangle + C_2\Psi_2(r)|2\rangle \tag{2.24}$$

where $\Psi_1(r)$ and $\Psi_2(r)$ denote the electron wave functions after the object has been excited by an energy transfer $\Delta E_{1,2}$ into the states $|1\rangle$ and $|2\rangle$ respectively. $\Psi_0(r)$ is the elastically scattered wave function, where the initial state of the object has not been changed. With a biprism we can split the incident wave into two waves, one incident onto the sample and one reference wave Ψ_{ref}, which does not interact with the sample at all. Alternatively, instead of leaving the specimen only on one side of the optical axis as shown in figure 2.2, we can move it to the middle of the column so that all illumination penetrates the sample. In this case the reference wave goes through and interacts with the sample as well. In our model this equates to splitting Ψ_0 through Ψ_2 into pairs of two waves each. We can then denote one wave of each pair by Ψ_0 through Ψ_2, and one by $\Psi_{0,\text{ref}}$ through $\Psi_{2,\text{ref}}$. (When incorporating reference waves we will omit proper normalization of the wave functions in order to avoid lengthy normalization factors.)
On a detector outside the object we observe without the use of any biprism the probability density

$$\begin{aligned}
\varrho(r) &= |\Psi_{\text{final}}|^2 \qquad (2.25)\\
&= |C_0\Psi_0(r)|^2 \langle 0|0\rangle \qquad \text{term 1}\\
&\quad + |C_1\Psi_1(r)|^2 \langle 1|1\rangle \qquad \text{term 2}\\
&\quad + |C_2\Psi_2(r)|^2 \langle 2|2\rangle \qquad \text{term 3}\\
&\quad + 2\,\mathrm{Re}[C_1C_2^*\Psi_1(r)\Psi_2^*(r)] \langle 2|1\rangle \qquad \text{term 4}\\
&\quad + 2\,\mathrm{Re}[C_0C_1^*\Psi_0(r)\Psi_1^*(r)] \langle 0|1\rangle \qquad \text{term 5}\\
&\quad + 2\,\mathrm{Re}[C_0C_2^*\Psi_0(r)\Psi_2^*(r)] \langle 0|2\rangle \qquad \text{term 6.}
\end{aligned}$$

(A rigorous derivation requires us to explicitly write out the time dependence. The result, however, is the same: The observed probability amplitude does not depend on time.) A detailed discussion of the terms 1 through 6 including a reference wave will allow us to answer the questions above:

Question 1: We know, of course, that the answer to this question is yes, otherwise I would not be writing this thesis. But it is instructional to consider it anyway, to

see how our model system works. Elastic scattering is characterized by the fact that the system remains in its ground state $|0\rangle$ and no energy is transfered from the incident wave into the system. If we are using a biprism as illustrated in figure 2.2 the final state in (2.24) becomes

$$\Psi_{\text{final}} = \Big(\Psi_{\text{ref}}(r) + C_0\Psi_0(r)\Big)|0\rangle + C_1\Psi_1(r)|1\rangle + C_2\Psi_2(r)|2\rangle.$$

This changes term 1 in equation (2.25) into

$$\varrho_{\text{elastic}} = |\Psi_{\text{ref}}(r) + C_0\Psi_0(r)|^2 \underbrace{\langle 0|0\rangle}_{=1} \tag{2.26}$$

This is identical to our original description of the interference pattern in equation (2.5) if we assume plane waves and C_0 is the amplitude of the object wave.

Question 2: To assess whether inelastically scattered electrons can interfere with each other we have to move the sample onto the optical axis so that all incident electrons, including the ones for the reference wave pass through the sample. With the biprism in place, the total wave function will become

$$\begin{aligned}\Psi_{\text{final}} &= C_0\Big(\Psi_{0,\text{ref}}(r) + \Psi_0(r)\Big)|0\rangle \\ &\quad + C_1\Big(\Psi_{1,\text{ref}}(r) + \Psi_1(r)\Big)|1\rangle \\ &\quad + C_2\Big(\Psi_{2,\text{ref}}(r) + \Psi_2(r)\Big)|2\rangle.\end{aligned} \tag{2.27}$$

Terms 1 through 3 in equation (2.25) now become

$$\varrho_{\text{wave } i} = |C_i|^2\,|\Psi_{i,\text{ref}}(r) + \Psi_i(r)|^2 \underbrace{\langle i|i\rangle}_{=1}, \quad \text{i=0,1,2.} \tag{2.28}$$

Apparently, not only the elastically scattered electrons (i=0) can interfere but also the inelastically scattered electrons (i=1,2), which have lost energy and excited the specimen from the ground state $|0\rangle$ into an excited state $|1\rangle$ or $|2\rangle$. This effect has been observed by Lichte and Freitag. [62] In their experiment electrons, which had lost 15.5 eV after being inelastically scattered at a plasmon in an aluminum sample, were brought to interference using a biprism. The dominant contribution to the interference pattern from the elastically scattered electrons was removed by using an energy filter, which transmitted only electrons that had lost energy to a plasmon.

To find out if electrons which have excited different object states can interfere, we have to discuss term 4 in equation (2.25), which now becomes

$$\varrho_{\text{mix}} = 2\text{Re}\Big[C_1C_2^*(\Psi_1\Psi_2^* + \Psi_{1,\text{ref}}\Psi_{2,\text{ref}}^*)\Big]\,\langle 1|2\rangle. \tag{2.29}$$

Apparently this term is only nonzero if the object states $|1\rangle$ and $|2\rangle$ overlap. (This implies that they occupy the same energy level!)
We can conclude that *only electrons which have lost energy to the same or overlapping object states are capable of interference. Electrons, which have excited different, non-overlapping states will not contribute to the interference pattern.* This result implies also that in order to observe interference of inelastically scattered electrons, the object states, which are excited, have to be delocalized over the interference width Δ of the hologram. In this context it would be interesting to repeat the experiments described in reference [62] not only with electrons which have lost energies to strongly delocalized plasmon excitations, as they occur in aluminum, but also with electrons which have lost energy to other excitations for example during generation of x-rays or Cherenkov radiation.

Question 3: In order to answer whether an unscattered electron can interfere with an inelastically scattered one and produce moving interference fringes, as known from light optics, we need to consider term 5 or 6 in equation (2.25). The final wave will be of the form

$$\Psi_{\text{final}} = (\Psi_{\text{ref}} + \Psi_0)|0\rangle + \Psi_1|1\rangle. \tag{2.30}$$

We have omitted any normalization factors for simplicity and assumed that only state one is being excited. To compare our treatment with the one of Van Dyck et al. [23] we need to write out the time dependence of the wave function while assuming an energy loss ΔE to the first excited state. We will omit the distinction between Ψ_{ref} and Ψ_0, which is not relevant to answer question 3:

$$\Psi_{\text{final}}(t) = e^{-iE/\hbar t}\Psi_0(r)|0\rangle + e^{-i(E-\Delta E)/\hbar t}\Psi_1(r)\, e^{-i\Delta E/\hbar t}|1\rangle. \tag{2.31}$$

The cross term number five in the probability density (2.25) then becomes

$$\varrho(r,t)_{\text{mix}} = \underbrace{e^{+iE/\hbar t}\Psi_0^*(r)e^{-i(E-\Delta E)/\hbar t}\Psi_1(r)}_{\text{part 1}}\underbrace{\langle 0|e^{-i\Delta E/\hbar t}1\rangle}_{\text{part 2}}. \tag{2.32}$$

In their discussion Van Dyck et al. consider only part 1 of the last equation. To find out the signal measured by a detector, which collects electrons over a time T, they integrate part 1 over time and obtain

$$\varrho(r)_{\text{part 1 only}} = \frac{\sin(\pi\Delta E/\hbar\, T)}{\Delta E/\hbar\, T}\Psi_0^*(r)\Psi_1(r). \tag{2.33}$$

The $\sin(\pi x)/x$ function is strongly peaked around the origin and contributes only significantly if

$$\Delta E < \frac{\hbar}{T}. \tag{2.34}$$

Hence, they conclude that for a typical recording time of $T = 1s$ only energy losses of less than 10^{-15} eV are be permissible for interference. If we, however, consider

the full equation (2.32) we see that (a) the probability density is time independent and (b) that the term is always zero, because the ground state does not overlap with any excited state. We can conclude that *unscattered and inelastically scattered electrons do not interfere with each other.*
It is still possible to produce moving interference fringes if the energy difference between the two electron waves are not produced by inelastic scattering. To this end electrons could for example be reflected at a moving electron mirror and change their energy according to the Doppler effect or could be guided through a drift tube, to which a time dependent potential is applied. [77, 95]

Question 4: This question remains the most controversially discussed issue in the literature. While Cowley [16] answers the question with yes, arguing along the original work of Gabor [36] and using optical arguments, others deny the possibility by employing quantum mechanical arguments. In section 2.2.1 we stated that *an electron can only interfere with itself* unless there was an electron source available, which could emit two electrons with a fixed phase relationship. So far no source with this property has been discovered. Because of this no interference is possible between an electron wave which has left the source with an energy $E - \Delta E$ and another electron wave, which has left the source with an energy E and lost an amount of energy ΔE by inelastic scattering.

For the following work we will only consider the interference of elastically scattered electrons and the unscattered reference wave. We can now rewrite equation (2.5) to include both the effect of the partial coherence μ of the source and inelastic electrons.

$$\begin{aligned} I(\vec{r}) &= 1 + A_{\mathrm{obj}}^2(\vec{r}) + I_{\mathrm{inel}}(\vec{r}) + \\ &\quad 2\mu A_{\mathrm{obj}}(\vec{r}) \cos\Big(2\pi\vec{q}_{\mathrm{c}}\vec{r} + \Delta\phi(\vec{r})\Big). \end{aligned} \tag{2.35}$$

The inelastically scattered electrons do not contribute to the interference term and appear as background, because the reference wave in our case does not travel through the sample and is therefore not scattered.

2.2.3 Coherence and Illumination in the Electron Microscope

Cold field emitters used in modern microscopes have an energy spread of only 300 meV at a beam energy of several hundreds of kilo electron volts. Hence the energy spectrum $s(k)$ in equation (2.15) is extremely narrow and electron interferences of the order of 160 000 have been observed experimentally as early as 1985. [95] Since usually only a few hundred fringes are recorded in an electron hologram the modulus of the temporal coherence μ_{tc} can be assumed to be 1 and the fringe contrast $\mu = |\mu_{\mathrm{sc}}||\mu_{\mathrm{tc}}|$ is essentially equal to the spatial coherence for an empty hologram.
The lateral coherence of the electron source, however, imposes a severe limitation to electron holography. As we will see in the following the lateral coherence is limited by

the brightness of the electron gun. Brightness is defined as the current density per unit solid angle emitted by an electron source and is conserved under optical imaging:

$$\mathrm{B} = \frac{I}{A\Omega}. \tag{2.36}$$

Here I is the total current emitted by the source with an emitting area A into a solid angle Ω. Following the discussion by Lichte [60] we assume an electron source with a Gaussian intensity distribution

$$i(\xi,\eta) = \frac{1}{\pi r_0^2} e^{-(\xi^2+\eta^2)/r_0^2}. \tag{2.37}$$

According to the van Cittert-Zernike (2.13) theorem the spatial coherence between two points illuminated by this source at an angle α is given by the Fourier transformation of the intensity distribution

$$\mu \approx |\mu_{\mathrm{sc}}(\alpha)| = e^{-\pi k \alpha r_0^2}. \tag{2.38}$$

Taking $A = \pi r_0^2$ as the area of the source and $\Omega = \pi\alpha^2$ as the solid angle the coherent current available for recording a hologram at a fringe contrast μ is given using equation (2.36)

$$I(\mu) = -B \ln(\mu)/k^2. \tag{2.39}$$

The coherent current is limited by the brightness of the electron source for a given fringe contrast. Note that this coherent current cannot be increased by increasing the energy of the electron beam and therefore decreasing k because the brightness B increases proportional to k^2. Table 2.1 summarizes key properties of sources used in electron microscopes and the superiority of field emission sources due to their high brightness, small energy spread, and small source size is obvious. This is the main reason why the success of electron holography went hand in hand with the development of field emission or Shottky emission electron microscopes. As the structure of the electron source perpendicular to the biprism has no influence on the fringe contrast, it can in some cases be beneficial to use the electron gun stigmators to create a strongly stigmatic illuminating beam perpendicular to the biprism. By doing so the coherent current available can be used more efficiently. [76]

2.3 Field Emission of Electrons

Field emission is the process in which electrons leave the surface of a material under the influence of a strong electric field. In order to overcome the potential barrier at the surface these electrons require energy. In conventional electron sources this energy is furnished in form of thermal energy by heating the source. In the field emission source, however, the potential step at the surface is deformed into a barrier by the strong external field, through which electrons can tunnel outside the electron source. Figure

Table 2.1: Comparison of electron sources commonly used in transmission electron microscopes. Compared to conventional sources, cold field emission guns as well as Schottky emitter guns are the best available choice for electron holography due to their high brightness and small source size. (compare [120] and [106])

	Tungsten	LaB_6	Schottky	Cold Field
Operating Temperature in K	2700	1900	1800	300
Source Size in nm	$50 \cdot 10^3$	$5 \cdot 10^3$	500	5
Brightness in $A/(m^2sr)$	10^9	$5 \cdot 10^{10}$	$5 \cdot 10^{12}$	10^{13}
Energy spread in eV	3	1.5	0.75	0.3
Vacuum requirement in Pa	10^{-2}	10^{-4}	10^{-6}	10^{-8}
Lifetime in hours	100	500	>6000	>1000

2.5 shows the form of such a potential barrier. Without any additional fields electrons have to overcome a potential step Φ in order to reach the vacuum energy level V_V from the Fermi level V_F. An external field F lowers this barrier by the amount $-eFx$. A further contribution to the potential barrier proportional to $-e^2/4x$ results from the positive mirror charge the electron "sees" when leaving the surface. The resulting barrier has then the form

$$V(x) = -eFx - \frac{1}{4\pi\epsilon_0} \cdot \frac{e^2}{4x} \tag{2.40}$$

and is shown in figure 2.5 as a solid line. Hence, the original barrier is lowered by an amount

$$\Delta\Phi = \sqrt{\frac{e^3F}{4\pi\epsilon_0}}. \tag{2.41}$$

The probability, with which electron tunnel through the barrier, can be calculated using the WKB (Wentzel, Kramer, Brillouin) approximation [82]

$$P(E, V(x)) = \exp\left\{ -\left(\frac{8m}{\hbar^2}\right)^{\frac{1}{2}} \cdot \int_{x_1}^{x_2} [V(x) - E]^{1/2} \right\}. \tag{2.42}$$

Here $V(x)$ and E denote the potential and kinetic energy of the electron, and x_1 and x_2 are the points at which the electron enters and leaves the potential barrier. In order to calculate the emission current density, the probability P has to be multiplied by the number of electrons, which hit a unit area of the surface of the electron source per unit time. This problem has been worked out by Fowler and Nordheim for $T = 0$ K [25], resulting in the following equation for the emission current density

$$j_F = \frac{1.54 \cdot 10^{-6}}{t^2(y)} \cdot \frac{F^2}{\Phi} \cdot \exp\left(-6.8 \cdot 10^{-7} \cdot v(y) \cdot \frac{\Phi^{3/2}}{F} \right). \tag{2.43}$$

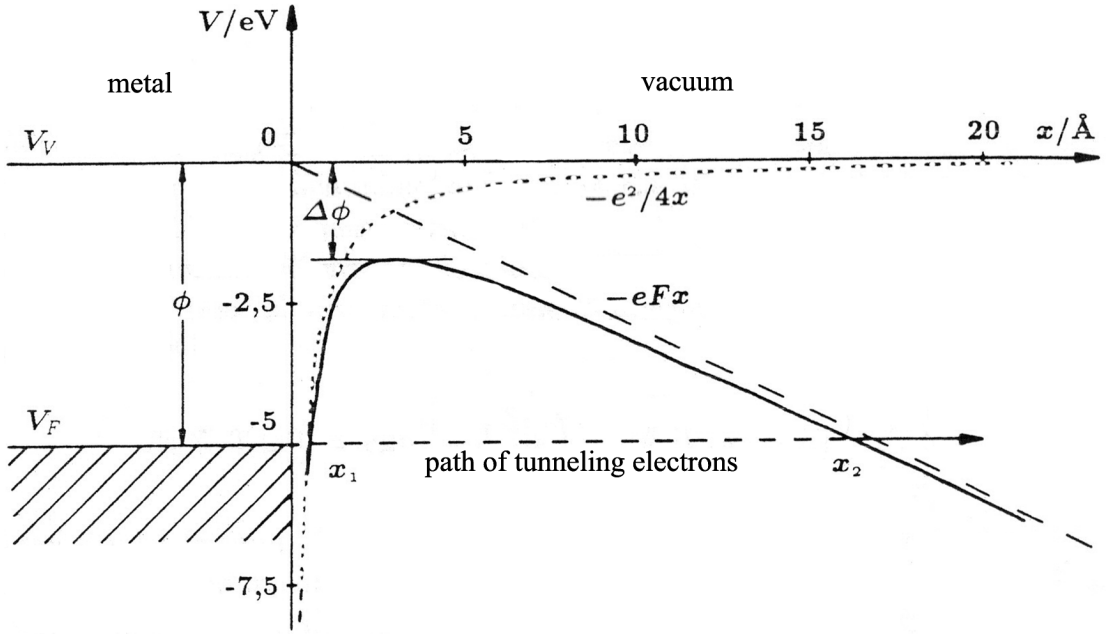

Figure 2.5: Potential at the surface of a metal with an external field of $F = 3 \cdot 10^7$ V/cm. V_F is the Fermi level and V_V denotes the vacuum energy level. The contribution of the external field to the barrier is shown as a dashed line, the contribution of the image charge as a dotted line. The resulting potential barrier is drawn as a solid line. The figure also shows the path $\overline{x_1 x_2}$ on which the electrons tunnel through the barrier (adapted from [82]).

The functions $t(y)$ and $v(y)$ of the dimensionless parameter

$$y = \sqrt{\frac{1}{4\pi\epsilon_0} \cdot \frac{e^3 F}{\Phi^2}} \tag{2.44}$$

have been tabulated in reference [44]. Assuming a field of $2 - 3 \cdot 10^7$ V/cm and a work function Φ of 4.5 eV, current densities of $10^2 - 10^4$ A/cm^2 can be obtained. In order to achieve the high electric fields, field emission sources need to be as sharp as possible. They usually consist of a tungsten wire, which is etched into a sharp tip at one end with an apex radius of 5 nm or less. As molecules are deposited on this tip the emission current falls. Because of this, field emission tips have to be operated under ultra high vacuum conditions and flashed before operation in order to remove any contamination. Nevertheless, even under ultra high vacuum conditions an exponential decay of the emission current can be observed with decay constants of 10 to 90 minutes.
For non-zero temperatures the probability for electrons to occupy an energy level above the Fermi energy will increase, which in turn increases the current density as well as the energy spread of the emitted electrons. In the case of thermal field emission the

Fowler-Nordheim equation can be modified to

$$j_{\mathrm{TF}} = j_{\mathrm{F}} \cdot \frac{\pi p}{\sin(\pi p)}. \tag{2.45}$$

Here $p = kT/d$ with $d = e\lambda F/(4\pi t(y))$ and λ the de Broglie wavelength of an electron with energy Φ.[82] The above equation works well for $p < 0.7$. For example one obtains $j(300K) = 1.03 \cdot j(0K)$ and $j(1000K) = 1.5 \cdot j(0K)$.[44]
The process, in which both field-emitted electrons and electrons emitted by thermal emission contribute significantly to the emission current at high enough temperatures, is called extended Schottky emission. In case of a small extraction field a broad potential barrier will result, which decreases the tunneling probability, and the contribution of tunneling electrons to the emission current becomes negligible. However, the potential barrier is still lowered by the extraction field, which increases the number of thermaly emitted electrons significantly as compared to the zero external field case. Such a process is called Schottky emission. Recently, Schottky emitters based on cathodes containing ZrO to lower the work function to a value of $\Phi = 2.95$ eV have become extremely popular as an alternative to cold field emission guns. Their brightness is typically an order of magnitude lower than the one of cold field emitters and the energy spread is increased by a factor 2-3. However, their significantly greater stability, their ability to work at higher pressures and their high current densities make them an ideal compromise (see table 2.1). Figure 2.6 summarizes the energy distributions for the different emission processes.

2.4 The Möllenstedt Biprism

As we have seen in the section 2.2.1, an electron can only interfere with itself. Therefore, in order to generate an interference pattern, the electron source needs to be split into two virtual sources using the electron optical equivalent of a biprism. Gottfried Möllenstedt's idea of an electron biprism was born in 1950 and first results were published in 1955 in the journal *Naturwissenschaften*.[75, 76] The accidental discovery of the electron biprism can be best described in Möllenstedt's own words:[74]

> "In 1950, at the Süddeutsche Laboratorien in Mosbach/Baden, when working with dark field micrographs in the electrostatic electron microscope, I had observed that a thin tungsten wire I used to intercept the primary beam in the focal plane of the electrostatic objective lens had charged up. I also observed that this charging led to double images on the final image screen. At that time I thought that such double images were of no physical interest unless they were coherent."

The electron biprism used in our microscope consists of a quartz fiber, typically of less than 1 μm diameter, which is coated with a thin gold-palladium layer. The fiber is mounted between two grounded plates. Figure 2.7 shows how such a fiber is made and

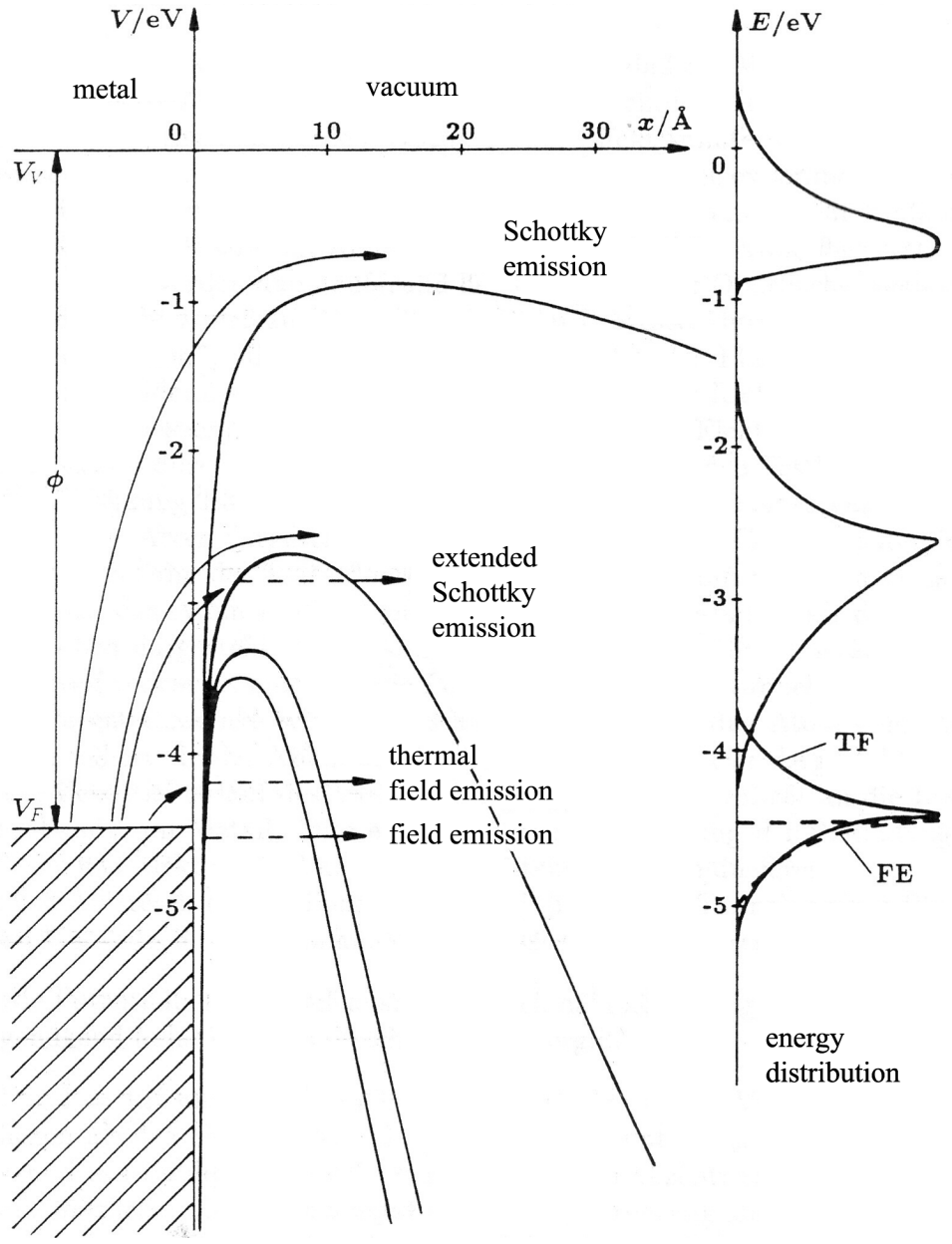

Figure 2.6: Energy distributions of different emission processes. The extended Schottky emission shows the biggest energy spread because two emission mechanisms overlap.

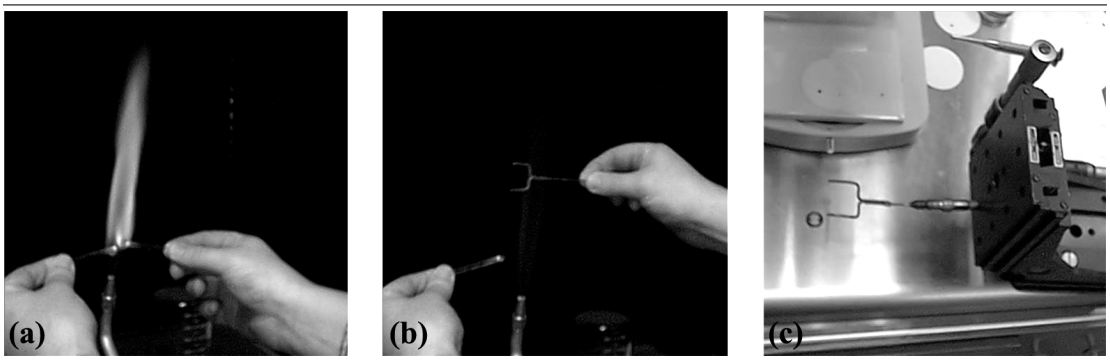

Figure 2.7: Making of an electron biprism: (a) Two quartz glass rods are rubbed in a blue burning hydrogen-oxygen flame until they melt together. The rods are then pulled apart slowly and a thin fiber starts moving up the flame. (b) One of the most difficult parts of the procedure is to catch the thin moving fiber with a fork, which has been sprayed with sticky spray. (c) The fiber needs to be carefully stretched over the biprism holder and glued in place with a conductive carbon or silver paint. Finally the fiber is gold-palladium coated in a sputter coater. Fibers as thin as 300 nm can be produced with this method.

more details about making and mounting a biprism can be found in the literature. [50] The deflection δ of the incident ray away from its original path by a biprism is given by

$$\delta = \frac{\pi}{2\log(r/r_\mathrm{f})} \frac{U_\mathrm{f}}{U_\mathrm{a}} \frac{1 + U_\mathrm{a}/511\,\mathrm{kV}}{1 + U_\mathrm{a}/1022\,\mathrm{kV}}, \tag{2.46}$$

where U_a is the accelerating voltage and U_f the voltage applied to the fiber. [61] All other symbols are explained in figure 2.8. Note that the deflection angle of the electron wave is independent of the distance $|x|$ to the fiber. Frost has shown that the above formula implies that the product of fringe spacing and fiber voltage is a constant. On the microscope used in this thesis this has been verified to be true within 3%. [28]
The glass-fiber biprism has several drawbacks: The pulling of quartz fibers is an extremely uncontrolled procedure and it often involves more luck than skill to catch the sub-micron fibers, which often break when the attempt is made to stretch them over the holder. Because of their small diameter but macroscopic length (typically 1-3 mm) mechanical stability can be a problem if long-time exposures are required. The electrical stability of the biprism voltage supply can add to the problem, especially in in microscopes operating a very high acceleration voltages, where in some operation modes several hundred volts on the fiber are required. To overcome this problem we have developed a more stable plate biprism. This biprism consists of a 25 μm thick tungsten wire, which is thinned locally using a focussed ion beam system (FIB). Details on FIBs can be found in section 5.2.4. The procedure results in a 500 nm thin 22 μm high plate of about 15 μm length as shown in figure 2.9. The stiffness of tungsten and the

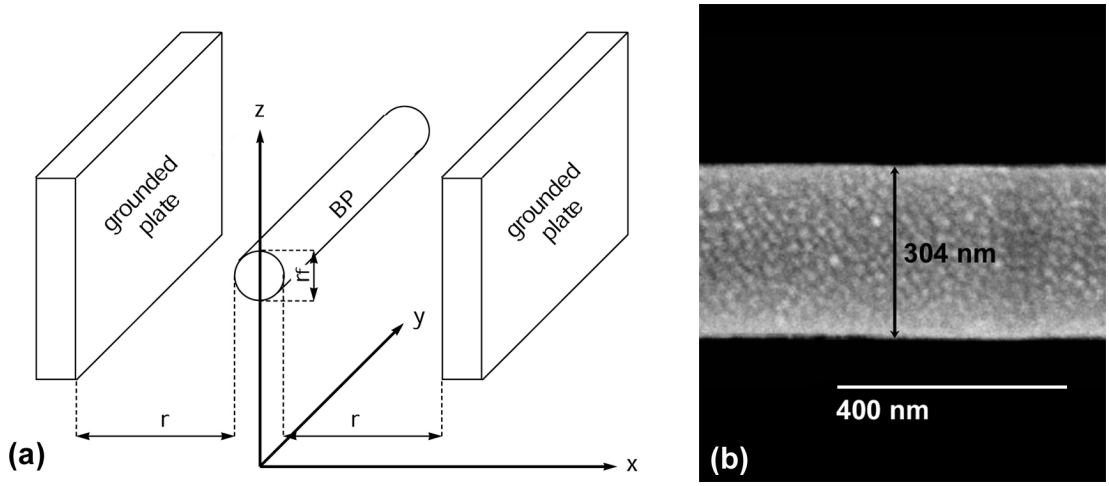

Figure 2.8: The electron biprism after Möllenstedt: (a) The electron biprism consists of a thin fiber between two grounded capacitor plates. (b) SEM image of a Au-Pd coated biprism fiber.

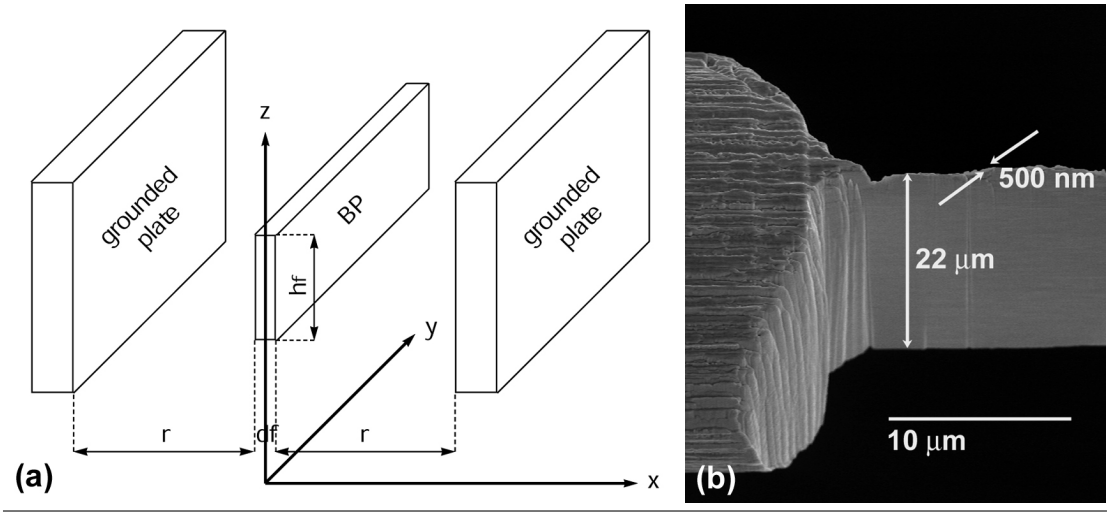

Figure 2.9: The plate biprism: (a) The plate biprism consists of a thick tungsten wire, which has been thinned into a thin plate using a focussed ion beam system, mounted between two grounded plates. (b) SEM image of the plate biprism

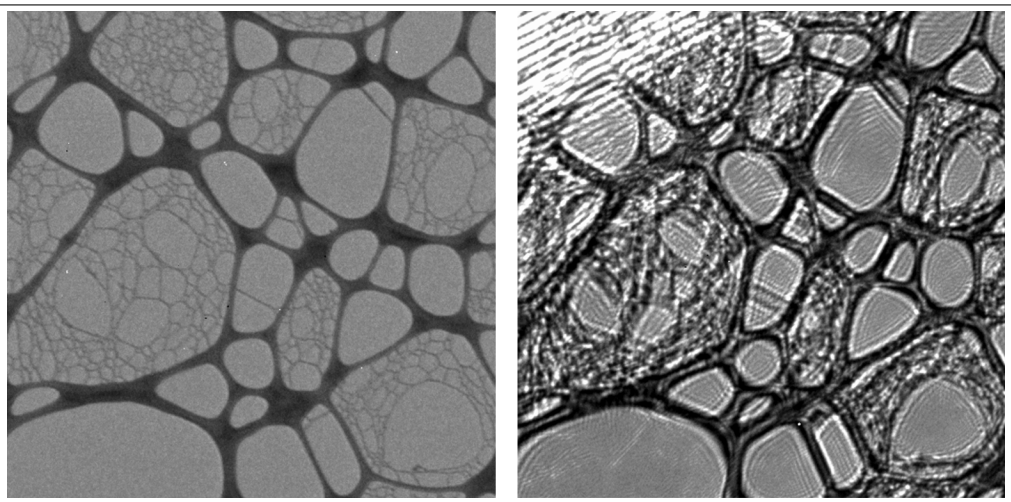

Figure 2.10: Defocus effect of the plate biprism. The figure on the left side shows a well focussed micrograph of a holey carbon foil without the biprism inserted. Once the biprism is inserted and a voltage applied to it, in this case -15 V, the image becomes clearly defocussed as shown in the right micrograph.

increased height of the plate with respect to the quartz fiber increases the mechanical stability. A major advantage is the fact that the tungsten wire can be mounted on the biprism holder before it is thinned, eliminating the awkward procedure of trying to stretch a sub-micron wire over a holder. We also predicted a much larger deflection of the electrons by the high plate than for the thin fiber for a given biprism voltage according to

$$\delta = \frac{h_\mathrm{f}}{2r}\,\frac{U_\mathrm{f}}{U_\mathrm{a}}\,\frac{1+U_\mathrm{a}/511\,\mathrm{kV}}{1+U_\mathrm{a}/1022\,\mathrm{kV}}. \tag{2.47}$$

There are drawbacks, however, associated with the new design: Since tungsten mills very slowly in the FIB, machining times can be of the order of half a day or longer. Below a thickness of 500 nm the fiber tends to break due to residual stress. Because of this for high resolution holography a thinner glass fiber will be better. We also observed that with the plate biprism inserted the image is defocussed, which is undesirable (figure 2.10). This problem, however, can be corrected by multiplying the sideband of the defocussed image with an appropriate phase plate during the reconstruction or by refocusing the image with the biprism inserted. Mohan has shown that a charged wire with a charged sphere in the back focal plane of an electron microscope can act as a phase plate and hence change the focus of the image. [73] We assume that the FIB-milled biprism, although not exactly in the back focal plane, can affect the electron wave in a similar way because simulated potential distributions for both the configuration used by Mohan and the plate biprism show similarities (figure 2.11). Our biggest surprise, however, was that the voltages needed to generate similar interference widths with the

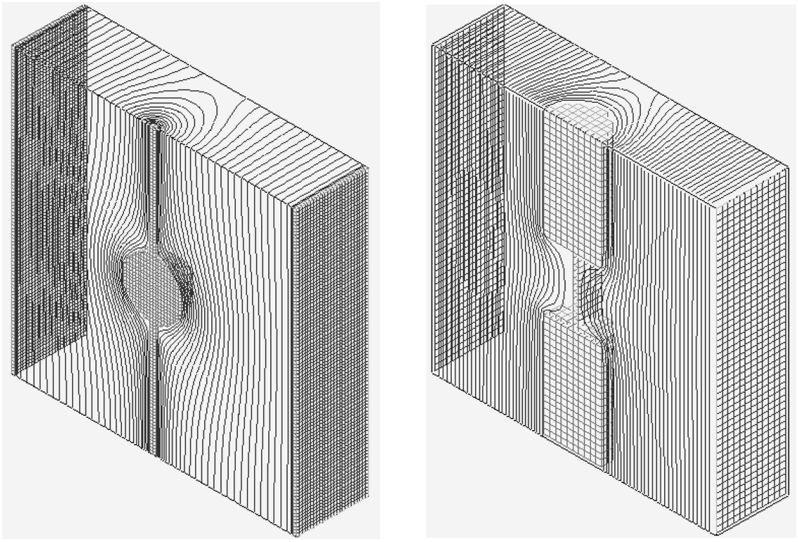

Figure 2.11: Comparisons of potential distributions. The configuration shown on the left side consisting of a charged fiber with a sphere is known to act as a phase plate in the back focal plane of a microscope. We believe that the similar potential distribution of the plate biprism shown on the right side can also defocus the electron wave.

plate biprism were the same as for the glass fiber, contradicting to our expectations (figure 2.12). These last two results need to be investigated further. A major problem is the fact that in order to carry out these experiments, the microscope was operated in a so-called free lens mode, which does not allow for accurate reproducibility of experimental conditions. We believe that it would be instructional to re-compare the two biprisms again in the high resolution mode of the microscope.

2.5 Electric and Magnetic Fields

In the previous chapters we have seen how we can produce two mutually coherent electron beams using a field emission source and a Möllenstedt biprism. These two beams are capable of forming an interference pattern on a screen as described by equation (2.35). We have also derived how the difference in phase between object and reference wave affects this interference pattern. Now we need to understand how these phase differences are created by the electric and magnetic field of the object under investigation: Let $V(\vec{r})$ describe the electric potential and let $\vec{A}(\vec{r})$ describe the magnetic vector potential the electron wave encounters as it travels down the column of the microscope. Furthermore, let L_{obj} denote the path of the object wave and L_{ref} the path of the reference wave. The elastic interaction of the electron wave Ψ of an energy E with these potentials is described by the Schrödinger's equation

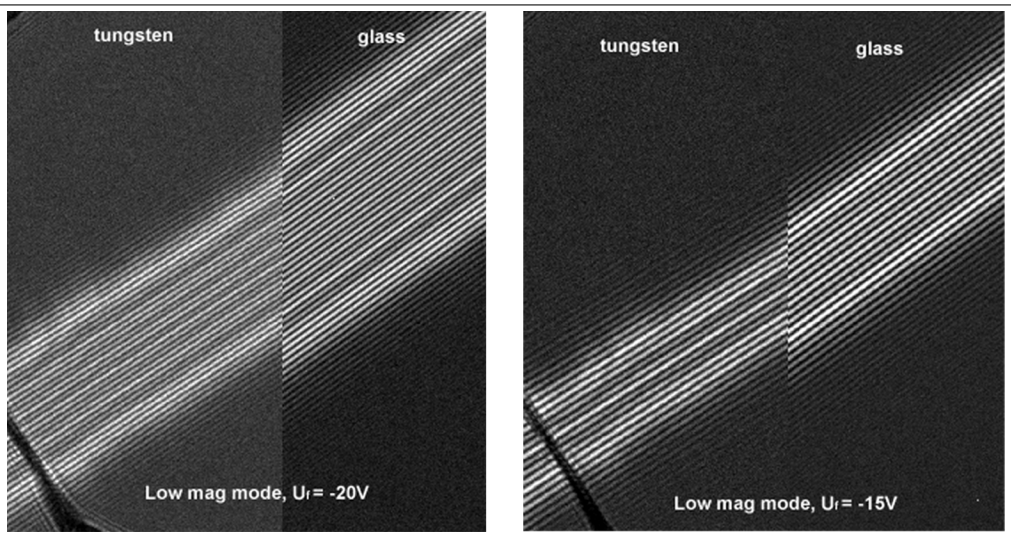

Figure 2.12: Comparison of the fringe spacing for the glass fiber and tungsten plate biprism. The images show interference fringes recorded at -20 V and at -15 V fiber voltage in low magnification mode. While the smaller overall interference width can be explained by the greater thickness of the tungsten plate biprism, the fringe spacing is essentially the same for both biprisms in contrast to our expectations.

$$\left\{\frac{1}{2m}\left(-i\hbar\vec{\nabla}-e\vec{A}\right)^2+eV\right\}\Psi = E\Psi. \tag{2.48}$$

We assume objects and reference waves of the form

$$\Psi(\vec{r}) = a(\vec{r})e^{i\phi(\vec{r})}. \tag{2.49}$$

Using the WKB approximation to solve Schrödinger's equation, the difference between the phase of the object wave and the reference wave can be shown to compute to

$$\begin{aligned}\Delta\phi(x,y) &= \frac{\pi}{\lambda E}\left(\int_{L_{\text{obj}}} V(\vec{r})ds - \int_{L_{\text{ref}}} V(\vec{r})ds\right) \\ &\quad -\frac{e}{\hbar}\left(\int_{L_{\text{obj}}} \vec{A}(\vec{r})\cdot d\vec{s} - \int_{L_{\text{ref}}} \vec{A}(\vec{r})\cdot d\vec{s}\right) \qquad (2.50)\\ &= \frac{\pi}{\lambda E}\oint V(\vec{r})ds - \frac{e}{\hbar}\oint \vec{A}\cdot d\vec{s}. \qquad (2.51)\end{aligned}$$

In order for the WKB approximation to be accurate the condition

$$\left|\frac{\lambda}{4\pi}\frac{d\lambda}{dx_i}\right| \ll \lambda \tag{2.52}$$

must be fulfilled, i.e. the change in λ over a distance $\lambda/(4\pi)$ should be small compared to λ. This holds if the potential varies slowly so that the momentum of the electron is nearly constant over several wavelengths. [93] Therefore, when investigating electric potentials on a nanometer and above scale with a 0.0251 Å electron wavelength, as in case of this thesis, where a 200 keV TEM was used, the WKB approximation holds.
In the following we assume that the electrons travel along the z-axis. The first ring integral in equation (2.51) describes that the phase difference is proportional to the difference of the projected potentials between the object and the reference wave. If we assume a constant potential for the reference wave, which we choose to be zero, and express the electron energy E in terms of the accelerating voltage V_a, the phase shift due to electric potentials becomes

$$\Delta\phi(x,y) = \frac{2\pi}{\lambda V_\mathrm{a}} \cdot \frac{2m_0c^2 + eV_\mathrm{a}}{m_0c^2 + eV_\mathrm{a}} \int_L V(\vec{r})dz \tag{2.53}$$

$$= C_E \int_L V(\vec{r})dz, \quad \text{where } C_E = \frac{2\pi}{\lambda V_\mathrm{a}} \cdot \frac{2m_0c^2 + eV_\mathrm{a}}{m_0c^2 + eV_\mathrm{a}}. \tag{2.54}$$

Here m_0c^2 is the electron rest energy. The energy dependent constant C_E has a value of 0.009245 rad/(V nm) for 100 keV electrons, 0.007282 rad/(V nm) for 200 keV electrons and 0.001039 rad/(V nm) for 300 keV electrons. In case of a constant potential V over a range t the last equation can be simplified further to

$$\Delta\phi(x,y) = C_E V t. \tag{2.55}$$

According to the second ring integral in equation (2.51) the electron waves acquire an additional phase difference if they encounter a non-zero magnetic vector potential. We have to note that there will even be a phase difference if the electron travels through a zero magnetic field as long as the vector potential does not vanish. This effect was first described by Aharonov and Bohm in 1959 [2] and experimentally verified by Bayh and Tonomura. [8, 111] We can write for the magnetic contribution to the phase difference

$$\Delta\phi(x,y) = \frac{e}{\hbar} \oint \vec{A} \cdot d\vec{s}$$

$$= \frac{e}{\hbar} \vec{B} \cdot \hat{n}\, dA \tag{2.56}$$

$$= \frac{e}{\hbar} F. \tag{2.57}$$

Here F denotes the magnetic flux the object and the reference enclose as illustrated in figure 2.13.

2.6 The Inner Potential of Crystals

The volume average of the scalar potential of a solid is known as its mean inner potential V_0. This potential is negative and ranges typically from -5 V to -30 V. According to

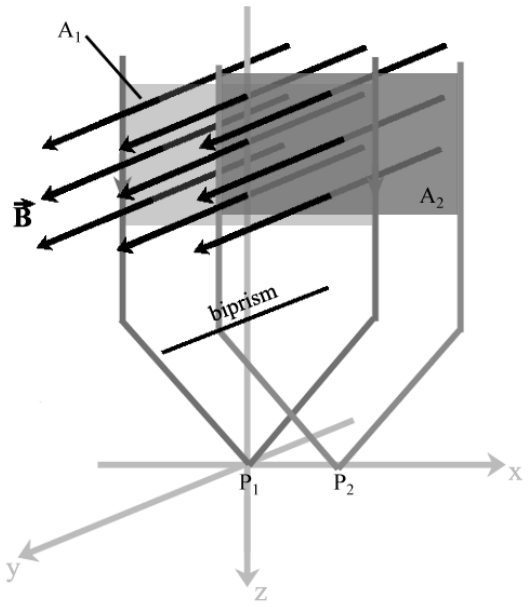

Figure 2.13: The phase difference between the object and the reference wave is directly proportional to the magnetic flux enclosed by the two beams. The light gray area A_1, which is centered about the z-axis, is penetrated by nine field lines, while the dark gray area A_2 is only crossed by six field lines. Hence the flux enclosed by the two rays, which interfere in point P_2, is 2/3 smaller than the flux enclosed by the rays, which interfere in point P_1. Due to this the phase resulting at P_1 will be larger than at P_2.

Reimer the mean inner potential is related to the electron-optical index of refraction

$$n = \frac{K}{k} = 1 + \frac{e|V_0|}{V_\mathrm{a}} \frac{m_0c^2 + V_\mathrm{a}}{2m_0c^2 + V_\mathrm{a}}, \tag{2.58}$$

where K is the electron wave-vector inside the material and k the wave vector in vacuum. [91] Due to the large difference between the mean inner potential and the kinetic energy of incident electrons, the index of refraction is only slightly larger than 1. Hence, detectable refraction effects occur only if the high energy electrons are incident at glancing angles like in RHEED. Because of this refraction effects are usually neglected in electron microscopy and the mean inner potential is taken as zero. However, V_0 can have several important implications, which have been summarized by Spence. [99] The effects of the mean inner potential on low energy electrons are discussed by the books on LEED. [67, 85] But in addition to changing the direction of the incident wave, the inner potential alters its phase according to equation (2.55). This effect can be measured by

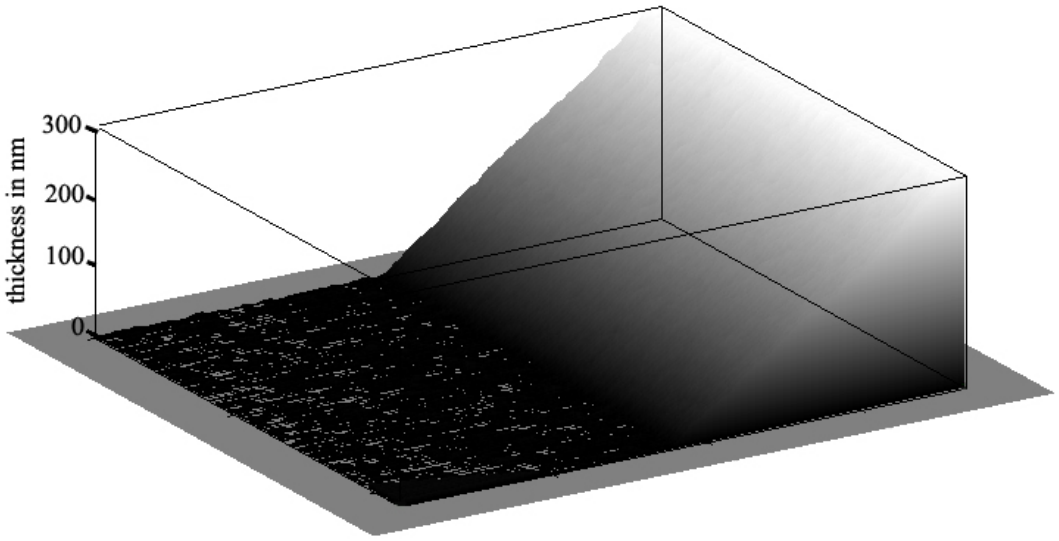

Figure 2.14: Using the mean inner potential of silicon and the known constant C_E the phase image obtained from a hologram can be converted into a thickness map. The image shows the thickness map of a polished silicon wedge.

electron holography.

$$\Delta\phi(x,y) = C_E V_0 t(x,y) = \frac{2\pi}{\lambda} \cdot (n-1)t(x,y) \tag{2.59}$$

If no additional electric or magnetic fields are present, holography can provide accurate maps of the projected sample thickness (see figure 2.14). While this method works well for amorphous materials, strong dynamical diffraction effects limit its use for crystals. In order to generate thickness maps of crystals, the latter have to be tilted away from any major zone-axis (see section 2.9.3).
Several different ways of calculating the inner potential have been published in the literature [88, 91, 92, 103] and a good summary can be found in reference [37]. This reference also contains a table of experimentally obtained values for the inner potential using different methods. The mean inner potential for silicon, which is of main interest for this work, has been determined by holography on cleaved wedges of known wedge angle and silicon spheres of known diameter as well as by RHEED experiments. Combining values from references [90, 116] an average value of $V_0 = (-11.96 \pm 0.58)V$ results, which will be used in this thesis.

2.7 Hologram Reconstruction

2.7.1 The Basic Reconstruction Process

As mentioned before, the recorded hologram, given by equation (2.35), contains both the full amplitude and phase information of the specimen exit wave. It is the goal of the reconstruction process to extract this information. This is achieved by a series of Fourier transformations of the hologram. In Fourier space equation (2.35) has the form

$$\begin{aligned}\mathbf{FT}\{I(\vec{r})\}(\vec{q}) &= \delta(\vec{q}) + \mathbf{FT}\{I_{\text{inel}} + A_{\text{obj}}^2(\vec{r})\} + \\ &\quad \delta(\vec{q} - \vec{q}_{\text{c}}) \otimes \mathbf{FT}\{\mu A_{\text{obj}}(\vec{r}) e^{i\phi_{\text{obj}}}\} + \\ &\quad \delta(\vec{q} + \vec{q}_{\text{c}}) \otimes \mathbf{FT}\{\mu A_{\text{obj}}(\vec{r}) e^{i\phi_{\text{obj}}}\} \end{aligned} \tag{2.60}$$

Apparently, the Fourier transformed hologram consists of three parts: A part located at the origin of the Fourier space (assuming that the sample does not contain any high frequency structures), which is simply the Fourier transform of a conventional bright field image of the object. Two parts corresponding to the cosine function are located at plus and minus the frequency of the periodic fringe pattern. These so called sidebands are essentially the Fourier transform of the object wave function. In order to retrieve the object wave function we need to cut out one of the two sidebands and center it in Fourier space to obtain

$$\mathbf{FT}\{A_{\text{obj}}(\vec{r}) e^{i\phi_{\text{obj}}(\vec{r})}\} \cdot B(\vec{q}). \tag{2.61}$$

Here $B(\vec{q})$ is the aperture function, which is used to cut out the sideband. An inverse Fourier transform allows us now to obtain the complex image wave function

$$\begin{aligned}\mathbf{FT^{-1}}\{\mathbf{FT}\{A_{\text{obj}}(\vec{r}) e^{i\phi_{\text{obj}}(\vec{r})}\} \cdot B(\vec{q})\} &= A_{\text{obj}}(\vec{r}) e^{i\phi_{\text{obj}}(\vec{r})} \otimes \mathbf{FT^{-1}}\{B(\vec{q})\} \\ &\approx A_{\text{obj}}(\vec{r}) e^{i\phi_{\text{obj}}(\vec{r})}. \end{aligned} \tag{2.62}$$

At this point the convolution with the aperture function B is usually ignored and the resulting function is taken as the complex electron wave-function. Artifacts introduced by the aperture function can be reduced to a negligible minimum by using a Butterworth filter as the aperture function

$$B(\vec{q}) = \frac{1}{1 + c \cdot (q/q_{\max})^{2\tau}} \tag{2.63}$$

as discussed in [115]. Figure 2.15 shows the complete reconstruction sequence. The size of the aperture selecting the sideband has to be chosen carefully in order not to include pixels belonging to the center part of the Fourier space on the one hand and to contain high enough spatial frequencies on the other hand in order not to filter out small details in the reconstructed phase image. The optimum choice for the fringe spacing of the holographic fringes in this context will be discussed in the section about recording of holograms, section 2.8.

Because the original phase information is contained within the cosine term representing

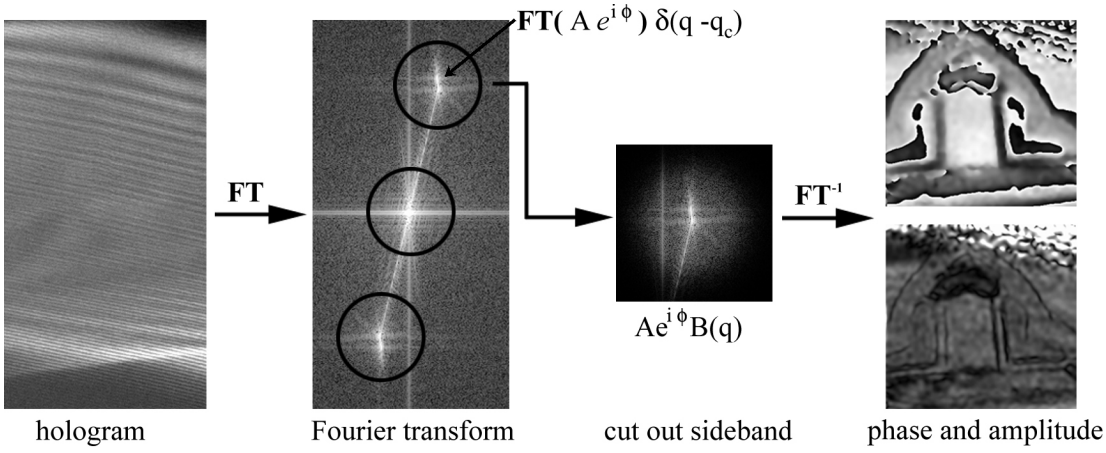

Figure 2.15: Reconstruction of holograms: The recorded hologram is Fourier transformed resulting in two distinct sidebands and a center part in Fourier space. One sideband is cut out and centered in Fourier space. The inverse Fourier transform of the centered sideband results in the complex object wave, which can be displayed as phase (top) and amplitude (bottom) image.

the interference fringes, it faces the ambiguity $\cos(\phi) = \cos(\phi + 2\pi)$. Hence the phase information can be only obtained modulo 2π and a phase jump results whenever the phase exceeds the 2π range. It is sometimes advantageous to display phase information without these 2π phase jumps, which makes it necessary to add or subtract multiples of 2π from certain areas of the image (see figure 2.16). Phase-unwrapping algorithms, which can perform this work to some extent automatically have recently become available. [51]

2.7.2 Using Reference Holograms

Typically the reconstructed phase image of an empty hologram, recorded with no sample in the field of view, will not be completely flat due to distortions and background fields. It is possible that electric and magnetic fields from the lenses of the microscope are not perfectly symmetric and will cause a phase shift as discussed in section 2.5. The projection lenses in the microscope are known as a likely source for distortions, as they have to image large areas. In addition to this, shear-distortion in the transfer fiber optics used in CCD cameras can contribute to the problem. Finally, local thickness and voltage variations of the biprism fiber can cause non-uniformity in the phase of the electron wave. In order to account for these distortions it is a good practice to record a reference hologram, which is a hologram with the sample removed from the field of view, with every hologram. The complex sideband of the hologram can then be divided by the one of the reference hologram in order to remove all distortions mentioned above.

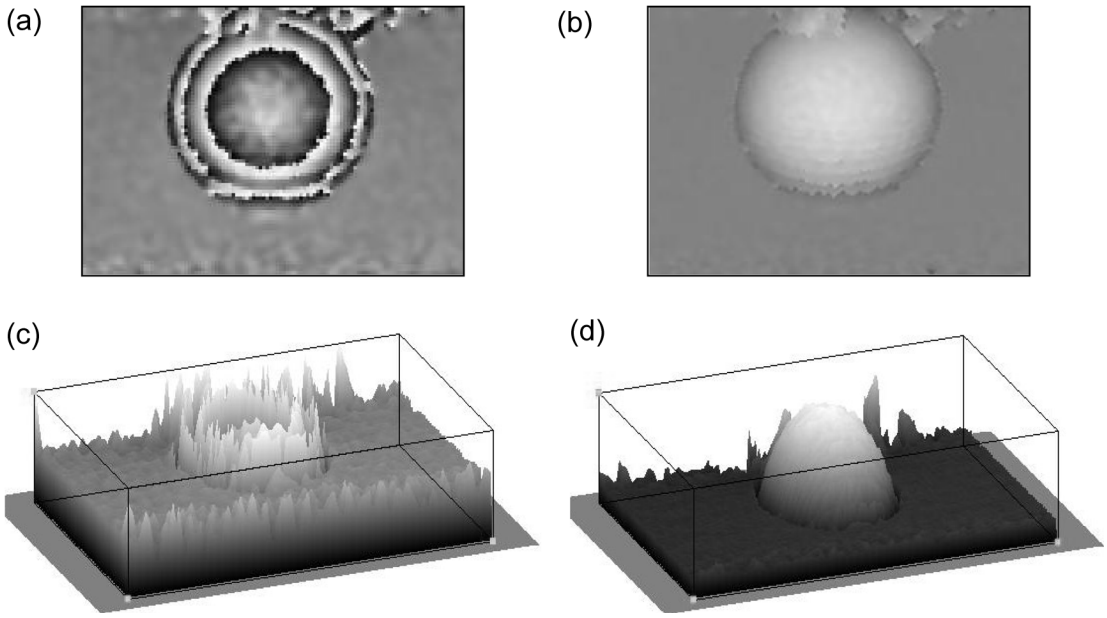

Figure 2.16: Phase-unwrapping of reconstructed phase images: (a) Phase image of a latex sphere. Phase jumps occur whenever the phase exceeds 2π. (b) Phase jumps have been removed by phase-unwrapping with an algorithm by Frank Karl [51]. (c) 3D-rendering of the phase image with phase jumps. (d) 3D-rendering of the unwrapped phase image.

An additional benefit of the reference hologram is that it facilitates locating the correct center of the sideband. It is a widespread practice to center the sideband about its brightest pixel. But for most holograms this is not necessarily the true center of the sideband, which is located at the frequency of the holographic fringes in Fourier space. The incorrect centering of the sideband will result in the phase of the reconstructed image being tilted. This problem can be avoided by using the highest amplitude pixel of the reference hologram sideband as the center of the sideband for both holograms (see figure 2.18).
All hologram reconstructions presented in this thesis have been done using a reference hologram unless otherwise noted.

2.8 Recording of Holograms

In order to resolve small details in the reconstructed holograms the smallest details to be resolved should be covered with at least three fringes, as demonstrated in figure 2.19. This will guarantee that the high spatial frequency components of the information in the center of Fourier space do not overlap with the ones of the sidebands. In order to adequately sample the interference fringes four pixels on the CCD camera per fringe

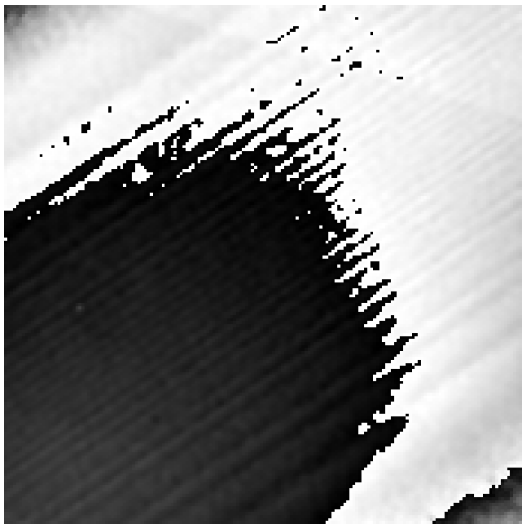

Figure 2.17: Even with the sample removed from the field of view when recording a hologram, the reconstructed phase image is not completely flat due to lens fields and fiber-optic shear of the CCD camera.

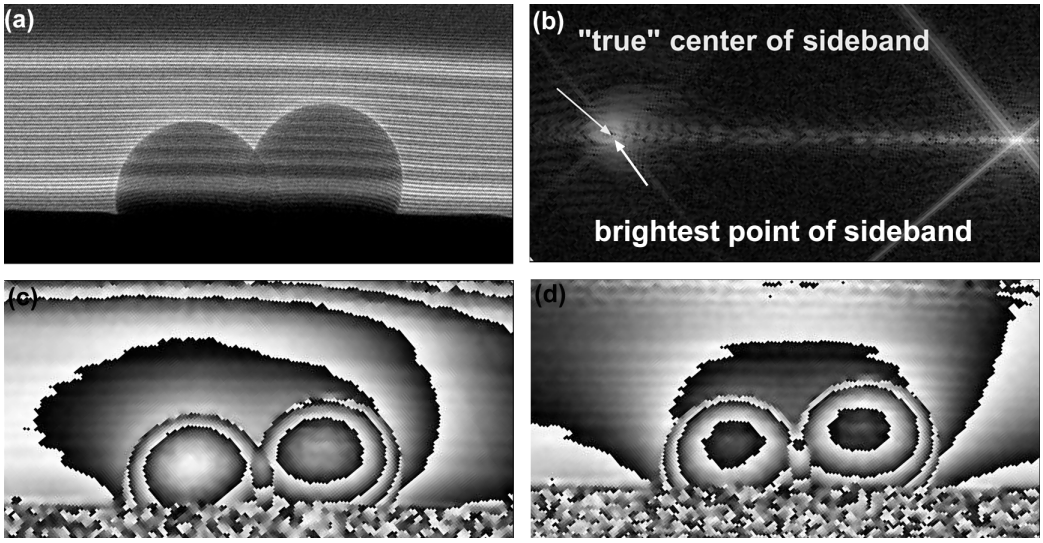

Figure 2.18: Correct centering of the sideband: (a) Hologram of two charging latex spheres. (b) The brightest pixel of the sideband is not necessarily its true center. (c) Phase image of two charging latex spheres reconstructed with the sideband centered about the brightest pixel. (d) Phase image reconstructed with a correctly centered sideband. (Images courtesy of Bernhard Frost.)

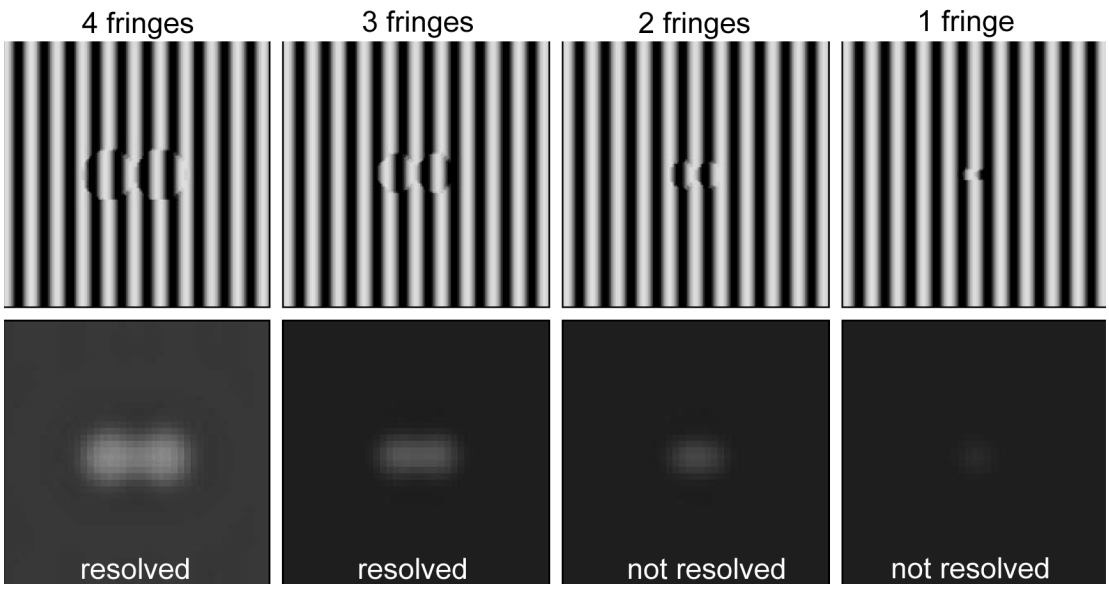

Figure 2.19: In order to resolve two points it is necessary to cover them with at least three fringes. The figure shows simulated holograms of two circles, which shift the phase of the electron wave by $\lambda/4$. An ideal fringes contrast of 100% is assumed. The upper row shows the simulated holograms, the lower one the corresponding reconstructed phase images.

are necessary. [89] With the electron detection following Poisson's statistics the phase detection limit of the hologram is given by

$$\delta\phi = \frac{C}{V}\frac{1}{\sqrt{N\,\mathrm{DQE}}}. \tag{2.64}$$

Here V is the fringe contrast given by the degree of coherence of the electron beam $|\mu|$, which is decreased by instrumental instabilities and the modulation transfer function of the recording medium as well as by inelastic scattering: $V = |\mu| V_{\mathrm{inst}} V_{\mathrm{MTF}} V_{\mathrm{inel}}$. N is the number of incident electrons and DQE is the detection quantum efficiency of the CCD camera. Values between $\sqrt{2}$ and $\sqrt{14}$ have been reported in the literature for the constant C. [19, 64] Since the overall fringe contrast usually cannot be changed for a given setup in a given instrument, long recording times are desirable to increase N and therefore the phase detection limit. Figure 2.20 shows holograms recorded at different exposure times and illustrates the statistical nature of the recording process. Instrumental stabilities, however, usually limit the recording time to below 30 seconds for our instrument. In order to avoid artifacts due to the drift of the biprism the reference hologram should be recorded immediately after each hologram. When recording holograms, it is necessary to balance several aspects: Part of the interference band needs to extend into the vacuum area outside the sample as a reference wave. Because of this the

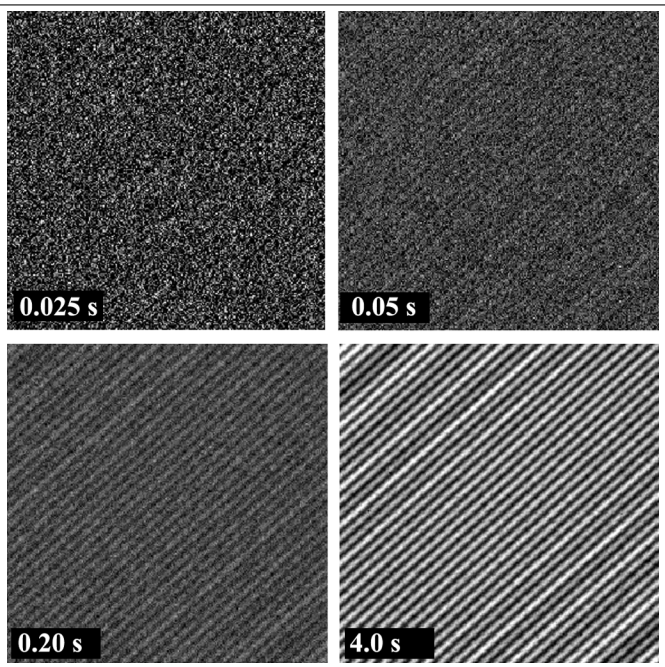

Figure 2.20: Series of exposures of increasing duration showing the build-up of the interference pattern. At a very short exposure of 0.025 seconds the image appears to consist of random noise only. But with increasing exposure time the fringe pattern becomes visible.

feature under investigation should be located very close to the sample edge. Since this is often not the case, the interference width Δ needs to be chosen as large as possible. This is done by increasing the voltage of the biprism fiber in order to increase the angle with which the left and right electron waves are deflected, which in turn increases the area over which both waves overlap (see figure 2.21). But this also decreases the fringe spacing since the product of fiber voltage and fringe spacing is a constant. [28] As we have seen, however, in the chapter on coherence 2.2.1, increasing the angle under which the image plane is illuminated decreases the coherence, which, as noted in the previous paragraph, deteriorates the phase resolution. In practice, the TEM operator needs to balance all these and additional instrument-specific aspects to achieve the optimum condition for a given case.

2.9 Artifacts in Electron Holography

In off-axis electron holography some artifacts can arise specific to the method. We will discuss at this point only the ones relevant to the medium and low magnification work done as part of this thesis. A detailed review of several additional artifacts, including the ones important for high resolution work, has been published by Lichte et al. [63]

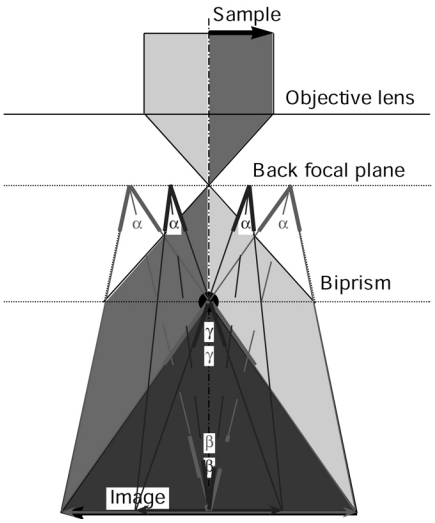

Figure 2.21: The biprism generates two virtual sources for an observer in the image plane. With increasing biprism voltage the electrons are being stronger deflected from their normal path. The virtual sources move apart, the interference width is increased and the fringe spacing decreases, together with the spatial coherence.

2.9.1 Fresnel Fringes

Since the incoming electron wave is Fresnel-diffracted at the edges of the biprism one finds that in the image plane both phase and amplitude of the image and reference waves are modulated by Fresnel fringes. These Fresnel fringes usually cause problems at the edge of the interference band, while the center remains unchanged. With the x direction chosen perpendicular to the edge and $x = 0$ at the geometric shadow of the edge, the intensity of the Fresnel-diffracted electron wave can be written as

$$I(x_f) \;=\; 0.5 I_0 \Big(\Big(C(x_f) + 0.5 \Big)^2 + \Big(S(x_f) + 0.5 \Big)^2 \Big) \tag{2.65}$$

and the phase as

$$\Phi(x_f) \;=\; \frac{\pi}{4} - \arctan\left(\frac{S(x_f) + 0.5}{C(x_f) + 0.5} \right). \tag{2.66}$$

Here x_f denotes the the dimensionless Fresnel coordinate

$$x_f \;=\; x \sqrt{\frac{2ka}{b(a+b)}} \tag{2.67}$$

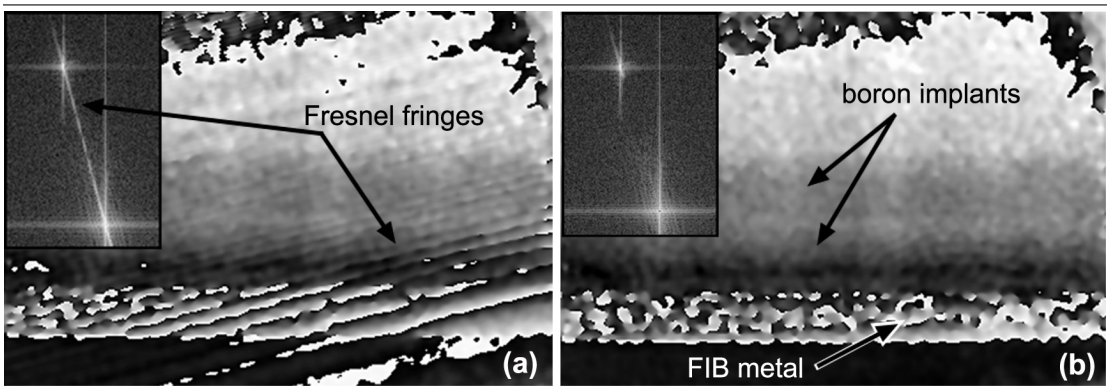

Figure 2.22: Because of Fresnel diffraction at the edges of the biprism, the hologram is modulated with Fresnel fringes. By carefully dampening the pixels between the center of Fourier space and the center of the sideband these Fresnel fringes can be removed.

with a the distance between the focal plane and the biprism and b the distance between the biprism and the image plane [63]. C and S are the Fresnel integrals

$$C(x_f) = \int_0^{x_f} \cos\left(\frac{\pi}{2}u^2\right)du, \tag{2.68}$$

$$S(x_f) = \int_0^{x_f} \sin\left(\frac{\pi}{2}u^2\right)du. \tag{2.69}$$

Fortunately, the reference hologram suffers from the same diffraction artifacts and the majority of problems caused by Fresnel diffraction can be eliminated by using reference holograms. But because the object tilts the image wave and because of biprism drift, Fresnel diffraction artifacts cannot be completely eliminated. In Fourier space Fresnel fringes as described by equation (2.65) correspond to a line from the center of Fourier space to the center of the sidebands. If these pixels are carefully dampened, Fresnel artifacts can be completely removed (see figure 2.22). A program in Digital Micrograph^{TM} has been written to conveniently dampen the corresponding pixels. A listing of this program can be found in appendix A. Great care has to be taken to avoid erasing any image information and the filtered image should be carefully compared to the original one.

2.9.2 Fringe Branching

A strong change in phase gradient in combination with a poor phase resolution can cause artificial branching of the interference fringes. The reconstructed phase of such branched interference fringes results in seemingly paradoxial phase images resembling the famous painting by M.C. Escher “Ascending and Descending” and make proper phase unwrapping impossible. The effect has been discussed by Frost and Matteuchi in

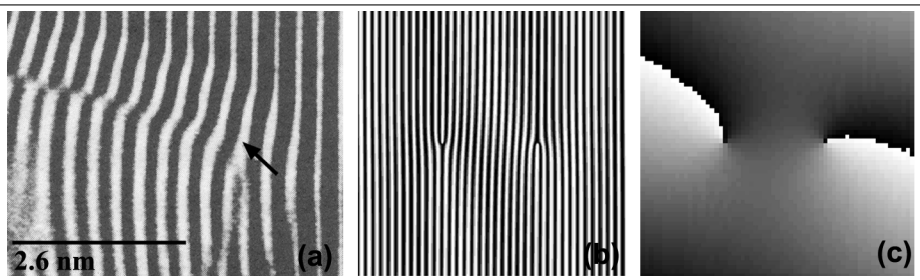

Figure 2.23: Artifacts caused by fringe branching: (a) Fringe branching near a magnetic CrO_2 needle. (b) Simulated hologram with fringe branching. (c) Reconstructed phase image of the hologram shown in part (b). (Images courtesy of Bernhard Frost.)

detail [30] and we will summarize the most important points. In case of a steep phase gradient over a small area the holographic fringes will become narrower as compared to an area with a more or less flat phase. Narrow fringes, however, suffer much stronger from instrumental instabilities than wider spaced fringes. Moreover, if the fringe spacing approaches the resolution limit of the detector, the apparent fringe contrast of the recorded hologram will weaken. Because of this, a slight decrease in fringe contrast in an area of slowly varying phase can correspond to a sharp drop in fringe visibility in an area with steep phase gradient. Frost has shown that this can lead to branching of the interference fringes as shown in figure 2.23 (a). The reconstructed phase image of such an artifact will show a point about which the phase spirals up continuously but reaches its original value again after one full turn (see figure 2.23 (b) and (c)). In order to avoid this artifact one should try to increase the fringe contrast and to decrease the overall fringe spacing to better sample small details while increasing the overall magnification of the hologram, if possible, to sample the fringes with more CCD pixels. Small changes in the geometry like rotating the sample or the biprism or moving the reference wave to the opposite side of the sample can in some cases eliminate this problem as well.

2.9.3 Diffraction Effects

Artifacts caused by diffraction effects are not a problem unique to off-axis holography. In fact, diffraction effects are known to cause problems in many other analytical TEM techniques such as EDS or EELS. To understand how diffraction of the electron beam by a crystalline sample can cause artifacts in the reconstructed phase image, we will consider a two-beam condition as is discussed in many textbooks on transmission electron microscopy, for example Williams and Carter [121]. In a two-beam condition the crystalline specimen is tilted such that only the direct beam $\phi_0 e^{ik_0 \cdot r}$ with the wave vector $\vec{k}_0$ and only one strongly diffracted beam $\phi_g e^{ik_g \cdot r}$ with the wave vector $\vec{k}_g$ contributes to the image. We assume that all other diffracted beams have an excitation error much larger or much smaller than zero and we can ignore their contribution. These assump-

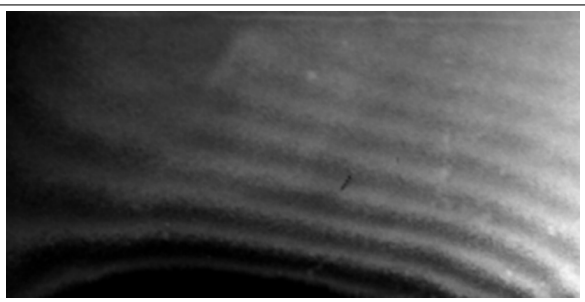

Figure 2.24: Under a two-beam condition the intensity oscillates between the transmitted and the diffracted beam. If the transmitted beam is blocked by an aperture in the back focal plane of the objective lens, an oscillating beam intensity can be observed on a wedge shaped sample as shown in the micrograph above.

tions together with the approximation that both the electron path and the excitation error s is parallel to the z-axis lead to the famous Howie-Whelan equations

$$\frac{d\phi_g}{dz} = \frac{\pi i}{\xi_g}\,\phi_0 e^{-2\pi i s z} + \frac{\pi i}{\xi_0}\,\phi_g \tag{2.70}$$

$$\text{and} \quad \frac{d\phi_0}{dz} = \frac{\pi i}{\xi_0}\,\phi_0 + \frac{\pi i}{\xi_g}\,\phi_g e^{2\pi i s z}. \tag{2.71}$$

Here ξ_0 and ξ_g denote the extinction distances for the transmitted and the deflected beam. The solution of these equations results in an amplitude of the wave function at the exit surface of a sample of thickness t of the form

$$\Phi_0 = \Big(\cos(\alpha t) - i\cos\beta\cdot\sin(\alpha t)\Big)e^{\pi i s t} \tag{2.72}$$

for the transmitted beam, and

$$\Phi_g = i\sin\beta\cdot\sin(\alpha t)\,e^{\pi i s t} \tag{2.73}$$

for the diffracted beam. The constants α and β depend on the extinction distance and the excitation error of the diffracted beam only. If for example the direct beam is stopped using an aperture in the back focal plane of the objective lens the image intensity will be given by

$$I_g = 1 - I_0 = \sin^2\beta\cdot\sin^2(\alpha t), \tag{2.74}$$

which will have the form of a series of dark and white fringes for a wedge shaped sample as shown in figure 2.24. For this work it is important to understand that in the two beam case the phase of both the diffracted and the transmitted beam become thickness dependent in a nonlinear manner and will result in a complicated phase dependence of

the total wave function on the sample thickness. In most cases more than one diffracted beam will be strongly excited, making the equations above even more complicated. Problems of dynamical diffraction effects can however be avoided by making sure the sample is tilted away from any major zone-axis. It is also a good practice to record a bright-field image before recording the hologram and carefully inspect it for any signs of dynamical diffraction effects over the area of interest, then tilt the sample further if necessary.

Thinking is more interesting than knowing, but not than beholding.

Johann Wolfgang Goethe

3 In-Line Electron Holography

In this chapter a short introduction to low voltage in-line holography is presented. Initial results obtained with a prototype for a low voltage point projection and reflection microscope (PPM) are shown. Parts of this chapter have been published in conference proceedings. [29, 108]

3.1 Low Voltage In-Line Electron Holography

The idea of a point projection electron microscope dates back to 1939 when Morton and Ramberg described the idea of an electron microscope consisting only of an electron point source, an electron transparent sample in close proximity of the source, and a viewing screen at a great distance from the sample as illustrated in figure 3.1. They noted that:

> "As this type of microscope involves no electron-optical elements, the images obtained are free from ordinary aberrations. The limit of resolution depends solely on the distribution of the initial velocities of the field electrons [...] making it possible to proceed beyond the resolution of the light microscope by some orders of magnitude."[79]

If the sample is located a distance z from the tip, the magnification of the sample will be $M = D/z$ on a screen a distance D away from the tip. Due to the extreme proximity between tip and sample it is hard to measure the tip-sample separation. But if the distance between the tip and the screen D is known (10 cm in our case) the magnification can be determined in the following way: We locate a feature on the sample of an unknown size l. For a given sample-tip distance z_1 this feature will appear with an M_1 times length $L_1 = M_1 l = D/(D-z)l$ on the screen. If we move the sample a distance Δz closer to the tip, the image of the feature is magnified further to a length L_2. The

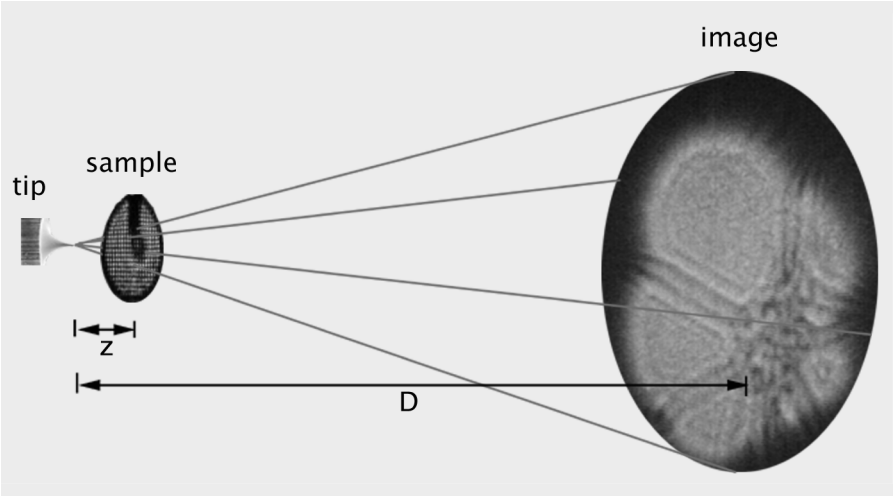

Figure 3.1: The figure above illustrates the simplicity of the point projection microscope. The sample is located a short distance z away from the nanotip and an $M = D/z$ times magnified image can be observed on a screen at a distance D from the tip.

displacement of the sample Δz can be accurately read off from the micrometer screw of the stage. The original tip-sample separation can then be easily calculated according to $z = \Delta z\, L_2/(L_2 - L_1)$ and the magnification is known.

As early as 1948 D. Gabor realized that by using a coherent electron source an in-line hologram containing both amplitude and phase information would result instead of the shadow images presented by Morton and Ramberg.[35] He explains:

> "The object is preferably smaller than the area which is illuminated in the object plane, and it must be mounted on a support which transmits an appreciable part of the primary wave. The photographic record is produced by the interference of the primary wave with the coherent part of the secondary wave emitted by the object. It can be shown that [...] interference maxima will arise very nearly where the phases of the primary and the secondary wave coincided."[35]

Figure 3.2 shows how interference effects will emerge with increasing magnification of the image. Apart from Fresnel fringes, which outline the holes of the carbon foil, part (c) of the figure also shows Young's fringes on the carbon bridges separating the holes. The fringe spacing over these bridges decreases with increasing width of the bridges, similar to a double slit experiment.
Point projection microscopy has recently received a lot of interest as a novel technique for the imaging of biological specimens and macro-molecules. [42, 43, 100, 118] At

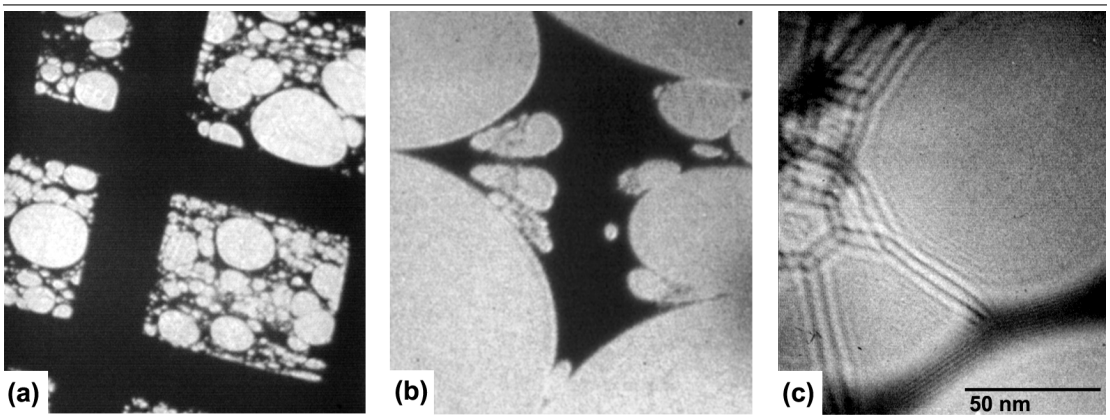

Figure 3.2: Series of point projection micrographs of a holey carbon film taken at 350 V beam energy. Part (a) shows an overview of the TEM grid with the carbon film. As the tip moves closer to the sample the magnification is increased (b) until interference fringes become visible (c). Part (c) shows two different kinds of fringes: Fresnel fringes, which outline the holes in the carbon film, and Young's fringes on the carbon bridges between the holes.

present, imaging of molecules and biological tissue in conventional transmission electron microscopes is greatly impeded by the rapid beam damage to these specimens. The capability of the point projection microscope to record images at beam energies as low as 7 eV [78] is expected to reduce beam damage. Unfortunately the inelastic mean free path of electrons in carbon falls to extremely low values of about 5-10 Å in the 80-300 eV energy range, in which most point projection microscopes are being operated at present. Therefore most samples, with the exception of thin macromolecules, have to be considered opaque or non-transparent masks. At energies below 10 eV and above 500 eV the mean free path increases to values above one nanometer. [68] Bardon et al. have shown that both conducting, semiconducting, and insulating objects can be observed by low-energy electron holography [5] and Georges et al. have used the method to observe charging objects.[40]

3.2 In-Line Hologram Formation

To understand the interference patterns produced by the point projection microscope a wave optical description of the image generation is necessary. The following treatment has been adapted from Spence et al. [102] With the nanotip a distance z away from the specimen a spherical wave of the form

$$t_z = e^{-i\pi\frac{x^2}{z\lambda}} \tag{3.1}$$

is incident on the sample. If the transmission of the electron wave through the sample is described by the transmission function $q(x)$ the wave at the exit surface of the sample

will be

$$\Psi_{\mathrm{s}}(x) \;=\; q(x)\cdot t_z(x). \tag{3.2}$$

The wave function in the far field can then be described by the Fourier transformation of the exit wave:

$$\Psi_{\mathrm{far}}(u) \;=\; \mathcal{F}\left\{\Psi_{\mathrm{s}}(x)\right\}. \tag{3.3}$$

The coordinate u in Fourier space is given by $u = \theta/\lambda$, where θ is the scattering angle of the electrons. Using known properties of the Fourier transformation $\mathcal{F}$ we can write

$$\begin{aligned}\Psi_{\mathrm{far}}(u) &= \mathcal{F}\left\{q(x)\cdot t_z(x)\right\} &(3.4)\\ &= Q(u)\otimes T_z(u). &(3.5)\end{aligned}$$

Here $Q(u)$ is the Fourier transformation of $q(x)$, $T_z(u)$ is the Fourier transformation of $t_z(x)$

$$T_z(u) \;=\; C\, e^{\pi i z\lambda u^2}, \tag{3.6}$$

and $\otimes$ denotes convolution of the two functions. The coordinate X on a view screen at a great distance D away from the tip is given by $X = \theta D$. Using $u = \theta/\lambda$ we can write

$$uz\lambda \;=\; X\cdot\frac{z}{D} \;=\; X/M, \tag{3.7}$$

where $M = D/z$ is the magnification. Using this result we can rewrite the equation for the wave function in the far field (3.5):

$$\begin{aligned}\Psi_{\mathrm{far}}(u) &= \int Q(v)\cdot T_z(v-u)\,dv &(3.8)\\ &= K\int Q(v)\cdot e^{i\pi z\lambda v^2}e^{-2\pi i X/Mv}\,dv. &(3.9)\end{aligned}$$

If we neglect the unimportant phase factor K this computes to

$$\begin{aligned}\Psi_{\mathrm{far}}(X) &= \mathcal{F}^{-1}\left\{Q(v)\cdot T_z(v)\right\}(X/M) &(3.10)\\ &= q(X/M)\otimes t_z(X/M). &(3.11)\end{aligned}$$

This important result shows that the point projection microscope produces an M times magnified image of the object, which is defocussed by the tip-to-sample distance z. Increasing the tip-to-screen separation D increases the overall magnification but does not change the defocus of the image. Finally, the intensity of the image on the micro-channel plate (MCP) is given by

$$I(X) \;=\; \Psi^*(X)\Psi(X) \;=\; \Big(q(X/M)\otimes t_z(X/M)\Big)^*\cdot\Big(q(X/M)\otimes t_z(X/M)\Big). \tag{3.12}$$

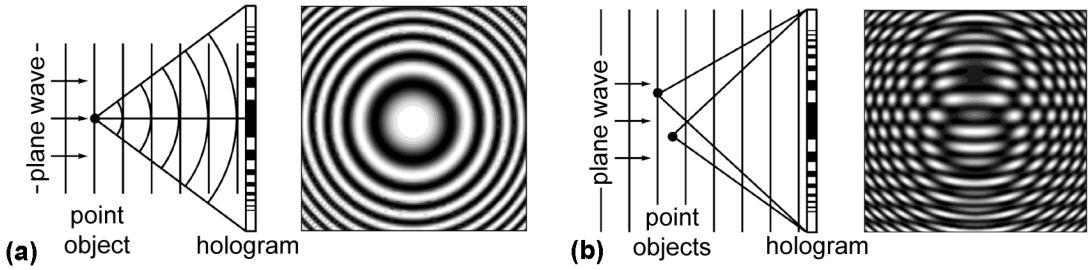

Figure 3.3: Simple point projection interference patterns: (a) A plane wave is coherently scattered by the sample, which consists of only one point. The spherical wave emitted from that point interferes with the part of the plane wave not influenced by the sample (reference wave) and forms a series of concentric circles. Since no lens is used, the interferogram represents an out of focus image. (b) If we add a second point object such that the distance to the image plane is different from the first one, the plane wave interferes with both the wave scattered by the first point and with the wave scattered by the second point creating a second system of concentric circles. The interference of the waves scattered from the two points has to be also taken into account. The different distance from the two points to the image plane results in a different spacing of the circles and in different centers, which reveals the three dimensional structure of the sample.

In the literature, the sample is often not described by the transmission function $q(x)$ but by an absorption function $p(x) = 1 - q(x)$. The resulting far field image wave is then given by

$$\Psi_{\text{far}}(X) \;=\; T_z\!\left(u = \frac{X}{Mz\lambda}\right) \;-\; p(X/M) \otimes t_z(X/M) \tag{3.13}$$

and the intensity by

$$\begin{aligned} I(X) \;\;=\;\; 1 \;-\; \Big(p(X/M) \otimes t_z(X/M)\Big) \;-\; \Big(p(X/M) \otimes t_z(X/M)\Big)^* \\ + \Big|p(X/M) \otimes t_z(X/M)\Big|^2 . \end{aligned} \tag{3.14}$$

Figure 3.3 illustrates the simplest possible case for forming an interferogram with the point projection microscope: A single point object is illuminated by the incident spherical wave and forms an out of focus image of the point on the screen, which is a series of concentric rings. If a second point object is added, an additional system of concentric circles will appear. The different distances between the two points and the image plane result in different spacings of the circles and in different center positions, which reveals the three dimensional structure of the sample. While these examples can be easily calculated from Huygen's principle, point projection images of more complex objects can

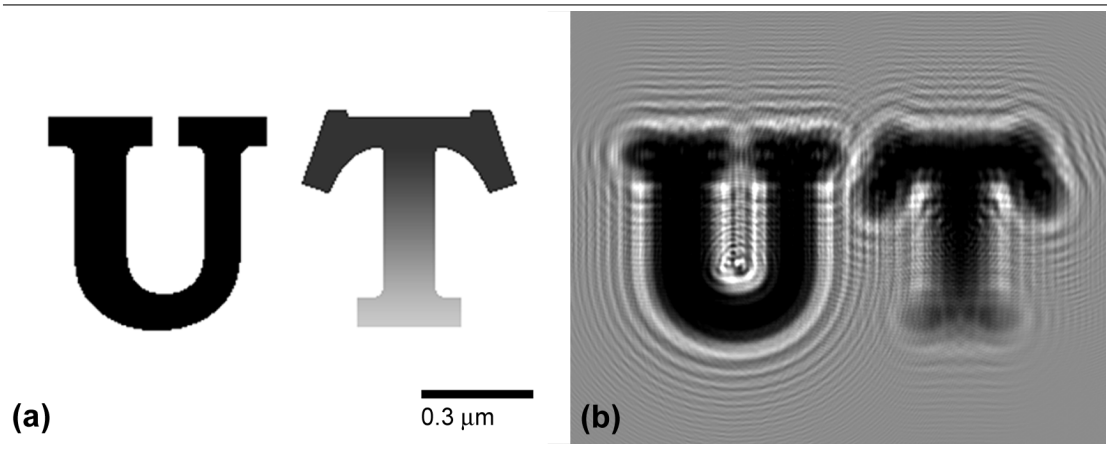

Figure 3.4: Numerical simulation of point projection imaging: (a) An object consisting of the letter U with a zero transmission function and an opaque "Power T". The transmitivity of the "Power T" decreases from 78% at the base to only 20 % at the top. (b) Simulated point projection hologram of the mask at 200 eV beam energy and 60 μm tip-sample separation according to equation (3.12).

be conveniently computed using the equations (3.12) or (3.14), which were derived in this section. An example familiar to the enthusiastic Volunteer is shown in figure 3.4. Simulation of point projection images of atomic clusters has been presented in detail by Kreuzer et al. [55] and will not be discussed here again.

3.3 The Reconstruction Problem

Unlike off-axis electron holography, the reconstruction of in-line holograms suffers from fundamental problems, that make an accurate retrieval of the object wave function difficult. According to the basic reconstruction algorithm discussed by Spence [102] the recorded in-line hologram is multiplied with the complex conjugate of the Fourier transform of the incident wave described in equation (3.1)

$$T_z^*(u) \;=\; \Big(\mathcal{F}(t_z(x))\Big)^* \;=\; C\, e^{-i\pi z\lambda u}. \tag{3.15}$$

The resulting product is inverse Fourier transformed and we obtain

$$\tilde{q}(x) \;=\; \mathcal{F}^{-1}\Big(T_z^*(x)\cdot I(x)\Big) \tag{3.16}$$

$$\;=\; \underbrace{q(x)}_{\text{term 1}} \;-\; \underbrace{p^*(x)\otimes t_{2z}^*(x)}_{\text{term 2}} \;+\; \underbrace{\left|p(x)\otimes t_z(x)\right|^2\otimes t_z^*(x)}_{\text{term 3}} \tag{3.17}$$

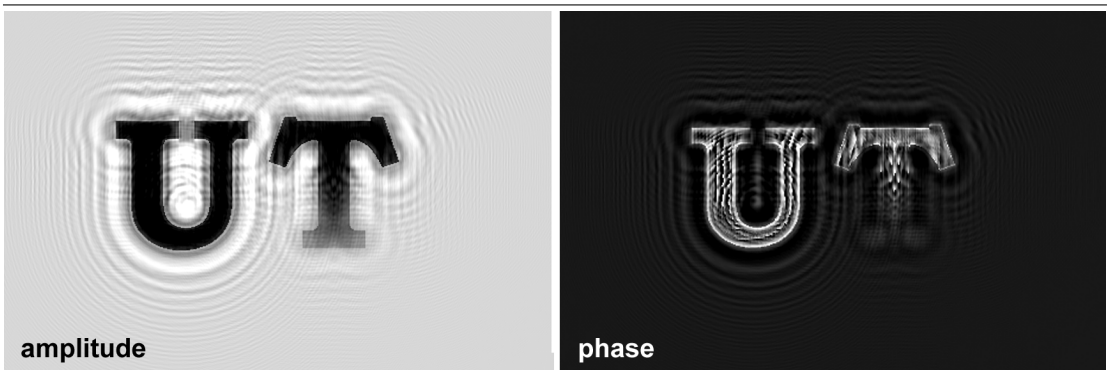

Figure 3.5: In-line hologram reconstruction after Spence [102]: The original object can be clearly recognized in the amplitude image. But the defocussed twin image is visible in the background. Also the phase shifts associated with the mask appear in the phase image. However, it is obscured by the twin image similarly to the amplitude image.

This result consists of three terms. The first term is the object wave, which we desired to obtain in this reconstruction process. The second term, which is known as the twin image, is the complement of the object defocussed by twice the the tip-sample distance. Note that the index z is a variable and thus $t_{2z} = \exp(i\pi x^2/(2z\lambda))$. The third and last term is a second order term, which describes the reconstruction of the hologram of the complementary object. In several publications on this topic a lengthy discussion usually follows at this point, which is aimed at making the second and third term disappear in order to finally declare the problem as solved. We have to understand, however, that these terms can contribute substantially to the reconstructed image: As the twin image is defocussed by twice the tip-sample separation it produces a slowly varying background, which allows the real image to be separated only if the condition $z \gg d^2/\lambda$ is fulfilled.[102] The third term, despite being a second order term, is not necessarily small either. For weak phase objects ($p \approx 0$) it is certainly small and can be neglected. But we have to note that at the low beam energies used in point projection microscopes the electron inelastic mean free path is extremely small and the transmitted wave will be attenuated strongly even for very thin objects and thus p will be non-zero. Figure 3.5 shows the reconstructed amplitude and phase image of the in-line hologram shown in figure 3.4.

Several methods have been discussed in the literature to improve the reconstruction of in-line holograms: Several authors have shown that by combining holograms recorded at different electron energies or different tip-sample separations the reconstruction can be improved.[94, 97, 98] Bardon et al. have demonstrated that by dividing the in-line hologram with a reference image, which is recorded with the sample removed from the field of view, an improved reconstruction can be obtained.[6] This method, however, can be expected to produce artifacts, as the sample acts as an extraction anode in the

point projection microscope, and removing it will not necessarily produce a "flat-sky condition" as the authors claim. Huang et al. have proposed an improved reconstruction method for pure amplitude objects.[47] In their method the electron wave is recurrently propagated back and forth, while substituting the amplitude of the wave by the square root of the experimental intensity. While the authors have shown a convincing reconstruction of simulated holograms using a 100 step recurrence, we have to note that the main point of doing holography is to obtain phase images of phase shifting objects. Hence, the applicability of their algorithm to pure amplitude objects only is a severe limitation. Morin et al. have avoided the in-line-reconstruction problems in the point projection microscope by placing an electron biprism a short distance behind the sample and hence recording off-axis holograms.[87]
As it is the goal of this work to utilize in-line holography for defect review, a perfect reconstruction is not necessary. The recorded holograms can simply be compared with the ones obtained from a defect free test structure, without using any reconstructions during this process. Because of this no further improvements to the reconstruction procedure apart from the ones discussed in the literature have been investigated.

3.4 The Point Projection Microscope - Experimental Setup

The point projection microscope consists of the small UHV chamber shown in figure 3.6, which can be evacuated using a turbo pump backed by a rotary fore-pump. With help of an additional 60 l/s ion pump a base pressure of better than $1 \cdot 10^{-9}$ Torr can be reached after 12 hours of baking at 150°C. Both the turbo and the ion pump can be separated from the chamber by gate valves. Under normal operation only the ion pump is working while the turbo and fore-pumps are turned off to reduce vibration. The pressure can be monitored by using a residual gas analyzer or reading the ion pump current. The sample is mounted on an xyz-stage, the position of which can be adjusted by micrometers. Tilt or rotation options can be added to the stage if needed. The tip is mounted on a vacuum feed-through, which allows tilt and motion in one axis. The top flange of the chamber holds a micro-channel plate with a phosphor screen. The phosphor screen can be imaged with a CCD camera. The inside of the chamber is screened by two layers of μ-metal. To insulate the chamber against vibrations the whole setup is placed on a vibration insulating table top, which floats on an air cushion. Vibration of tip and sample can be additionally dampened by using a viton gasket assembly. The nano-tip consist of a 230 μm diameter tungsten wire, which is electro-chemically etched in a sodium hydroxide solution. Recently the prospect of using carbon nano-tubes have been discussed to be used as high brightness nanotip emitters. [18] A review on ultra-sharp field emitters has been published by Gölzhäuser.[41]

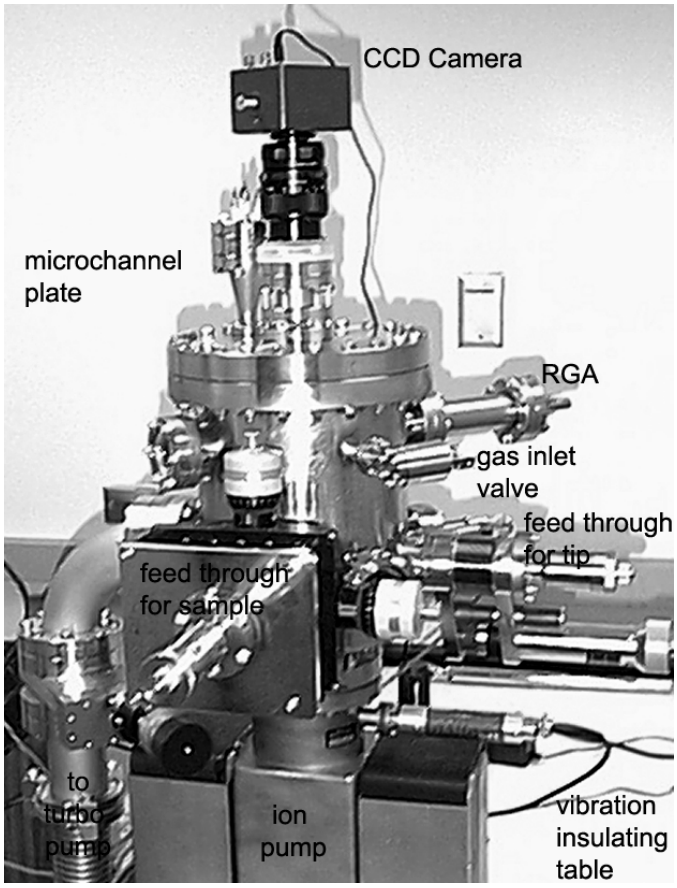

Figure 3.6: Photograph of the point projection microscope showing the vacuum chamber with its main components.

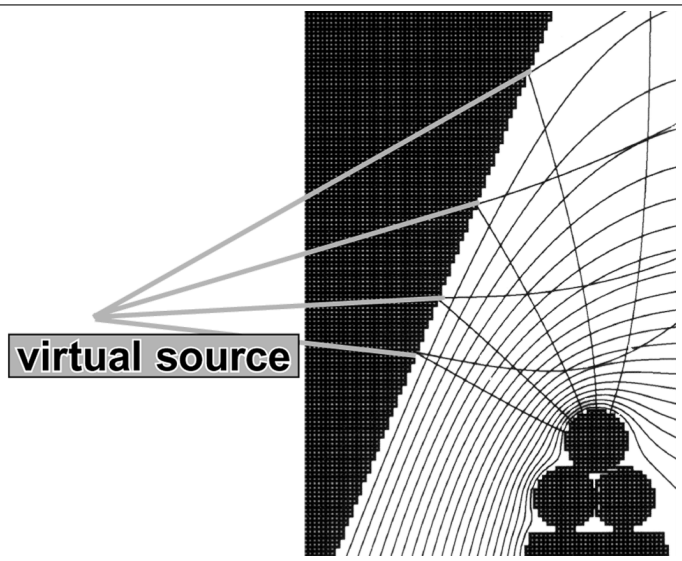

Figure 3.7: Operation of the PPM in reflection mode. A virtual source behind the sample can be assumed, which allows treating the reflection mode like the transmission setup.

3.5 Reflection Mode

Unlike many other groups we did not pursue the transmission imaging of biological samples or macromolecules after successfully constructing a transmission projection microscope. As we will discuss in this chapter, it is our main goal to operate the projection microscope in a reflection mode. This mode of operation was first attempted by Spence. [101] He imaged a GaAs surface at glancing beam incidence and 450 eV beam energy in a RHEED-like geometry. His images, however, were not dominated by sample topography but inelastic diffraction effects. The main idea of the reflection geometry is simple: With the tip close to a conducting sample surface, the reflected electrons seem to originate from a virtual tip behind the sample as illustrated in figure 3.7. The system can then be described analogously to the transmission case by assuming this virtual tip to be the electron source. Thus, the considerations on scaling the magnification and on the interference pattern are the same. At this point it is important to assess how many incident electrons are backscattered at the sample for a given incident beam voltage and incident angle to find optimum operating conditions for the reflection mode. Since we want to record a hologram we are only interested in electrons which are backscattered elastically, because inelastic scattering does not preserve coherency. To this end a Monte Carlo program was written in Visual C++ to calculate the elastic backscattering yield.

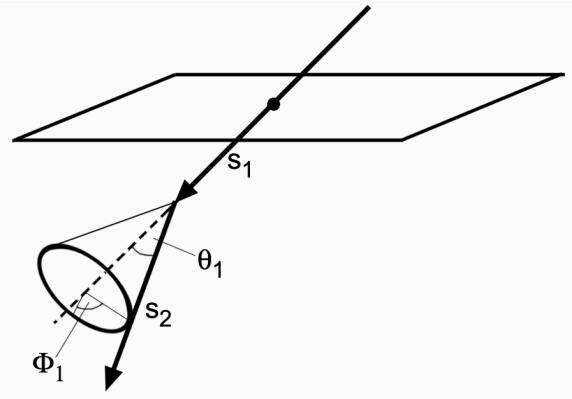

Figure 3.8: Electron trajectory in a solid. The angles Φ and θ as well as the distances s_i are determined by comparing the appropriate cross-sections to random numbers in a Monte Carlo simulation.

3.5.1 Monte Carlo Simulations of Elastic Electron Backscattering

In Monte Carlo simulations of electron beam–solid interactions a large number of electron trajectories is simulated. If a scattering event occurs, the appropriate scattering cross-section is compared against a random number and the trajectory is modified accordingly. Monte Carlo modeling for electron microscopy and microanalysis has been discussed in detail by Joy. [49] The following step by step description will demonstrate how such an algorithm can be used to calculate the elastic backscattering yield. Figure 3.8 illustrates the conventions used for labeling angles and positions.

1. An electron enters the sample at a point $\vec{r} = (0, 0, 0)$ with the velocity $\vec{v} = v_0\hat{n}$ and an energy E. It will travel along a straight line for a distance

$$s_1 \;=\; -\lambda(E)\log(R_1), \tag{3.18}$$

   where R_1 is a random number between zero and one, and $\lambda(E)$ is the total mean free path for an electron of energy E in the material under investigation. The total mean free path can be calculated from the elastic and inelastic mean free path, λ_e and λ_i, according to

$$\frac{1}{\lambda} \;=\; \frac{1}{\lambda_\mathrm{e}} \;+\; \frac{1}{\lambda_\mathrm{i}}. \tag{3.19}$$

2. The probability that an elastic scattering event occurs is given by

$$\frac{\lambda_\mathrm{e}^{-1}}{\lambda^{-1}} \;=\; \frac{1}{1 + \lambda_\mathrm{e}/\lambda_\mathrm{i}}. \tag{3.20}$$

Thus, a second random number R_2 is compared to this ratio. If the random number is smaller than $\lambda_e^{-1}/\lambda^{-1}$ an elastic scattering event is assumed, while for a random number larger than the ratio an inelastic scattering event has occurred. In the latter case the program returns to step one in order to start with the simulation of a new electron trajectory, because an inelastically scattered electron does not contribute to the elastically backscattered yield.

3. In case of an elastic scattering event the new direction of the electron needs to be determined. While its change in azimuth Φ_1 is completely random and can be easily determined by generating another random number R_3

$$\Phi_1 = 2\pi R_3, \tag{3.21}$$

the scattering angle θ_1 results from the Mott cross-section of the electron $\frac{d\sigma}{d\Omega}\big|_{\text{Mott}}$. To this end another random number R_4 is generated and the solution of the equation

$$R_4 = \int_0^{\theta_1} \frac{d\sigma}{d\Omega}\bigg|_{\text{Mott}} \sin\theta' d\theta' \Big/ \int_0^{\pi} \frac{d\sigma}{d\Omega}\bigg|_{\text{Mott}} \sin\theta' d\theta' \tag{3.22}$$

results in the desired scattering angle θ_1. To increase computing speed the integrals in the last equation should be tabulated for different values of θ_1 beforehand. The trajectory of the electron is now altered according to the scattering angles and the whole process is repeated from step one until an inelastic scattering event occurs or the electron leaves the sample. The number of electrons, which are leaving the sample after being scattered elastically only, divided by the number of incident electrons is the elastically backscattered yield.

The Monte Carlo algorithm discussed above requires several key parameters: The Mott cross-section, the elastic mean free path, and the inelastic mean free path of an electron of energy E in the material under investigation. Values for the Mott cross section, which have been compiled by Joy, have been used for the simulations. [48] The elastic mean free path can be calculated from the total Mott cross-section

$$\sigma_E = 2\pi \int_0^{\pi} \frac{d\sigma}{d\Omega}\bigg|_{\text{Mott}} \sin\theta' d\theta' \tag{3.23}$$

according to

$$\frac{1}{\lambda_e} = \frac{N_A \varrho}{A}\,\sigma_E, \tag{3.24}$$

where N_A is Avogadro's number, ϱ the density and A the atomic weight of the target.

Unfortunately, the inelastic mean free path has not been determined experimentally for a wide range of materials, especially at the low beam energies, which are of interest for this work. A good estimate for the inelastic mean free path can be obtained by

integrating the optical loss function of the material in question. The optical loss function

$$\Im\left[\frac{-1}{\epsilon(q,\omega)}\right] \tag{3.25}$$

can be extrapolated from tabulated optical data. Here ϵ is the complex dielectric constant, q the momentum transfer, $\Im$ denotes the imaginary part, and $\hbar\omega$ the energy loss. Following Ding and Shimizu [22] the loss function can be extrapolated from the complex dielectric constant at zero momentum transfer $\epsilon(q=0,\omega)$ according to

$$\Im\left[\frac{-1}{\epsilon(q,\omega)}\right] = \frac{\omega - \frac{\hbar q^2}{2m}}{\omega}\,\Im\left[\frac{-1}{\epsilon(\omega - \frac{\hbar q^2}{2m})}\right] \tag{3.26}$$

Here $\epsilon = \epsilon_1 + i\epsilon_2$ is the complex dielectric constant at zero momentum transfer, m is the electron mass, and all other constants have their usual meaning. The dielectric constants used in the present calculations were taken from Palik [84], who has compiled tables of optical properties for a large number of materials. Figure 3.9 shows the dielectric loss functions for silicon and copper, which have been calculated using the above model. The double differential inelastic mean free path at the energy E is then given by

$$\frac{d\lambda^{-1}}{d(\hbar\omega)dq} = \frac{1}{\pi a_{\mathrm{B}}}\,\Im\left[\frac{-1}{\epsilon(q,\omega)}\right]\frac{1}{Eq}, \tag{3.27}$$

where a_{B} is the Bohr radius. The total inelastic mean free path can now be calculated by integrating the double differential mean free path over all energy losses and momentum losses allowed for a given energy. In case of band-gap materials such as silicon, with a band-gap width E_{gap}, integration is as follows:

$$\frac{1}{\lambda(E)} = \int_{E_{\mathrm{gap}}}^{E}\int_{2m(\sqrt{E}-\sqrt{E+\hbar\omega})}^{2m(\sqrt{E}-\sqrt{E-\hbar\omega})}\frac{d\lambda^{-1}}{d(\hbar\omega)dq}\,dq\,d(\hbar\omega). \tag{3.28}$$

For metals the energy integration is from zero to $E - E_{\mathrm{F}}$ where E_{F} is the Fermi energy. Using this method inelastic mean free paths of silicon, copper, platinum, and gold were calculated for an energy range from 10 eV to 9 keV (figure 3.10).

The Monte Carlo program offers two different modes. In the first mode (see figure 3.11) a sample material can be selected and the incident beam energy is specified, as well as the angles of the incident plane and the number of simulated trajectories. The angular distribution of the elastically backscattered electrons is then calculated and shown in a polar, color-coded plot. If the "record path" box is checked the calculated trajectories are plotted in a three-dimensional plot and can be viewed from different viewpoints. The second mode allows the user to specify the material, a range of incident beam energies and a step size, as well as the angles of the incident beam, the number of electrons simulated per step, and the acceptance angle of the detector. The program will then

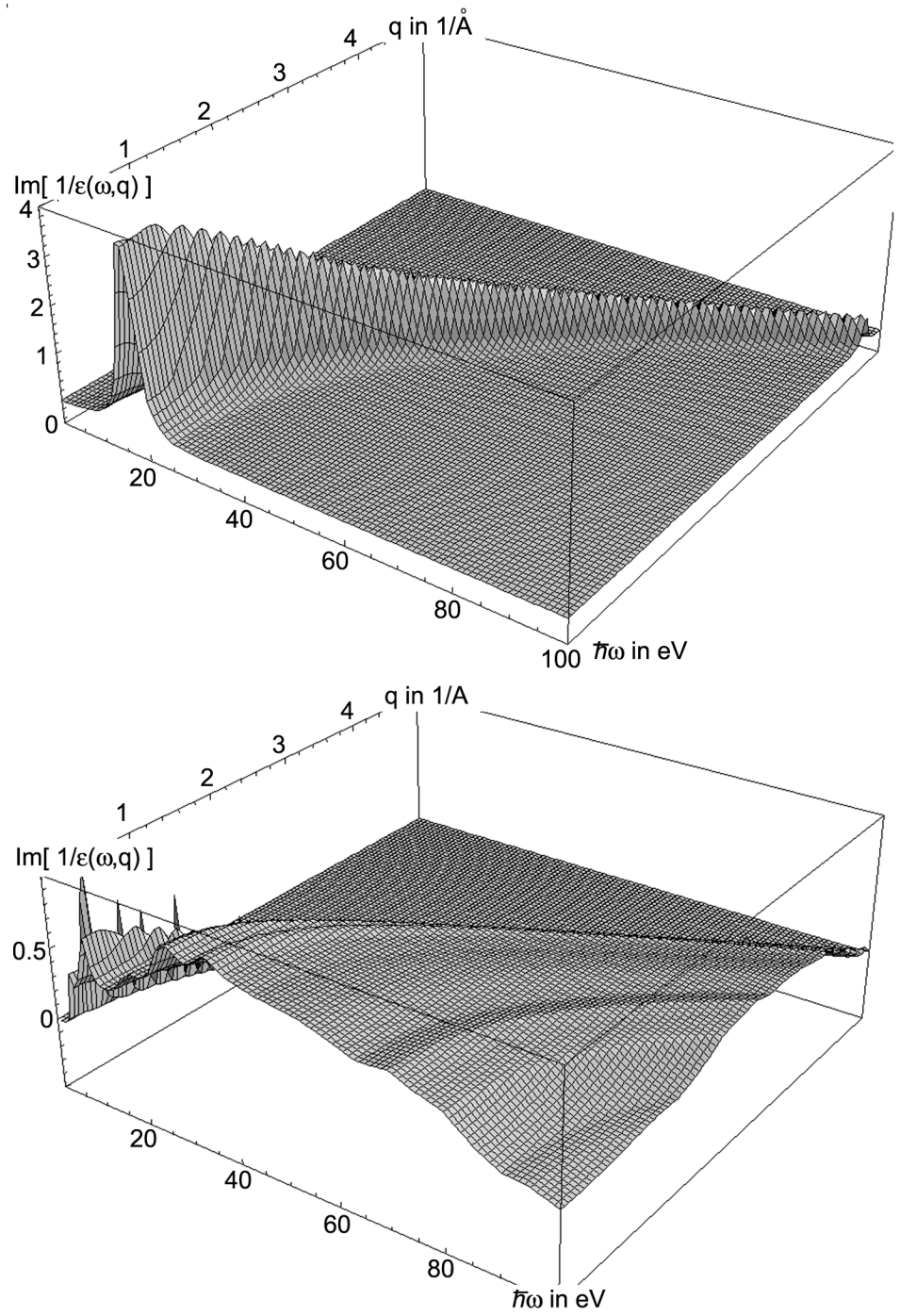

Figure 3.9: Dielectric loss function of silicon (top) and copper (bottom) calculated according to Ding et al. [22] using optical data compiled by Palik [84].

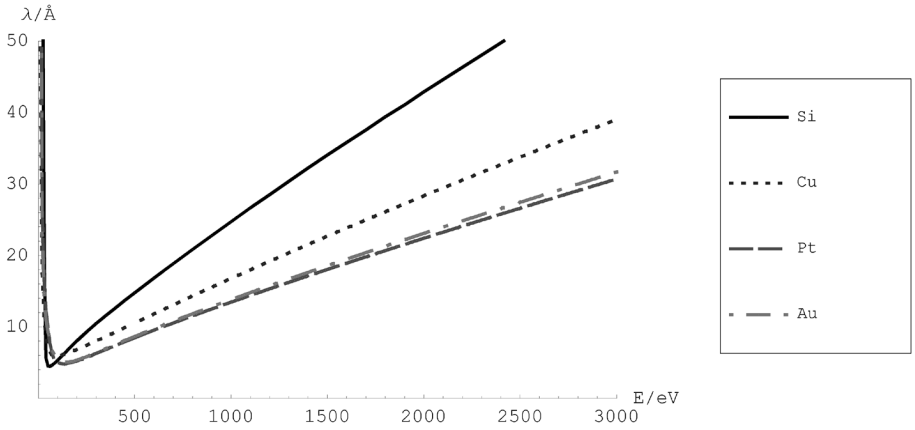

Figure 3.10: Inelastic mean free paths of silicon copper, platinum, and gold calculated from optical data.

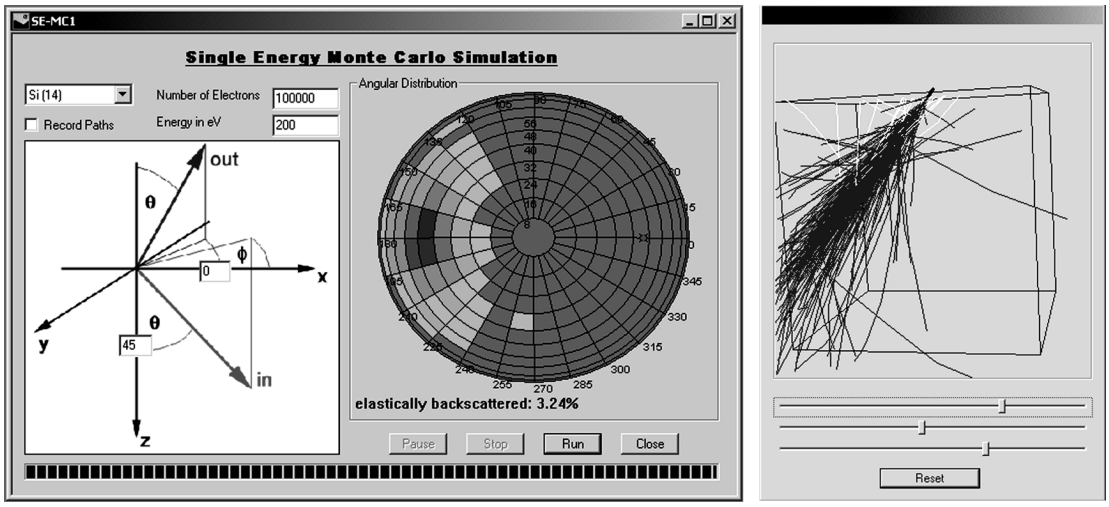

Figure 3.11: Monte Carlo simulation of the angular dependence of the elastically backscattered electrons in silicon for a 45 degree off-normal incident 200 eV energy electron beam. 100000 trajectories are simulated and the angular distribution of the elastically backscattered electrons are displayed. The simulated trajectories can be viewed in a three dimensional plot. Only 3.2% of the incident electrons are backscattered elastically.

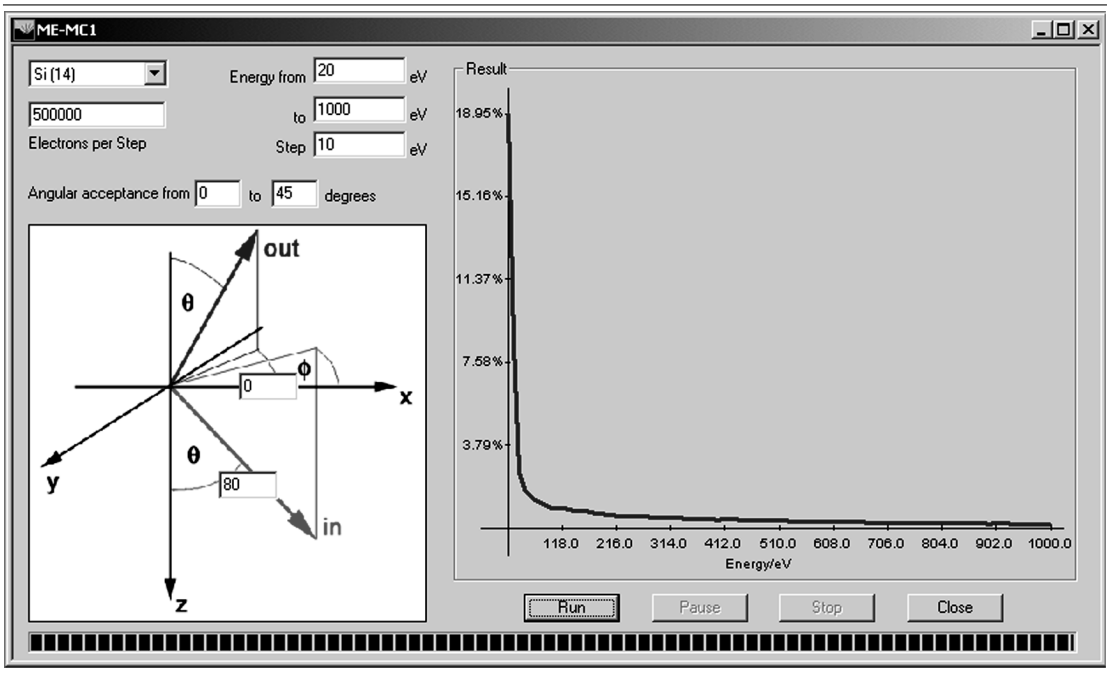

Figure 3.12: Monte Carlo calculation of elastically backscattered yield dependence on the energy of the incident electron beam. 500000 trajectories are simulated for each incident energy between 20 eV and 1000 eV in 10 eV steps. Electrons are incident 80 degrees off-normal onto a silicon sample. A detector, which accepts electrons within an angular range between 0 and 45 degree is assumed. For energies above 100 eV the resulting yield is only a few percent while the yield peaks sharply for low energies.

calculate the number of specified trajectories at each energy step and plot the yield for the given acceptance angle as a function of beam energy, as shown in figure 3.12. As one can see for realistic parameters the yield of elastically backscattered electrons is only a few percent. Only at ultra low beam energies and glancing angles reasonable yields above 10% are predicted.

3.5.2 Problems and Solutions for Reflection Imaging

As seen in the previous section, the yield for elastic backscattering of electrons is extremely low. Only at glancing angles of incidence and at ultra-low beam voltages can yields above 10% be achieved. So far, however, we have not been able to operate our nanotips below 100 V, and especially at high magnifications, where the tip needs to be close to the sample, the tip assembly does not allow for extremely glancing incidence. In addition to this we discovered another problem: Our experimental results show that under off-normal and especially glancing incidence no image of the surface can be obtained

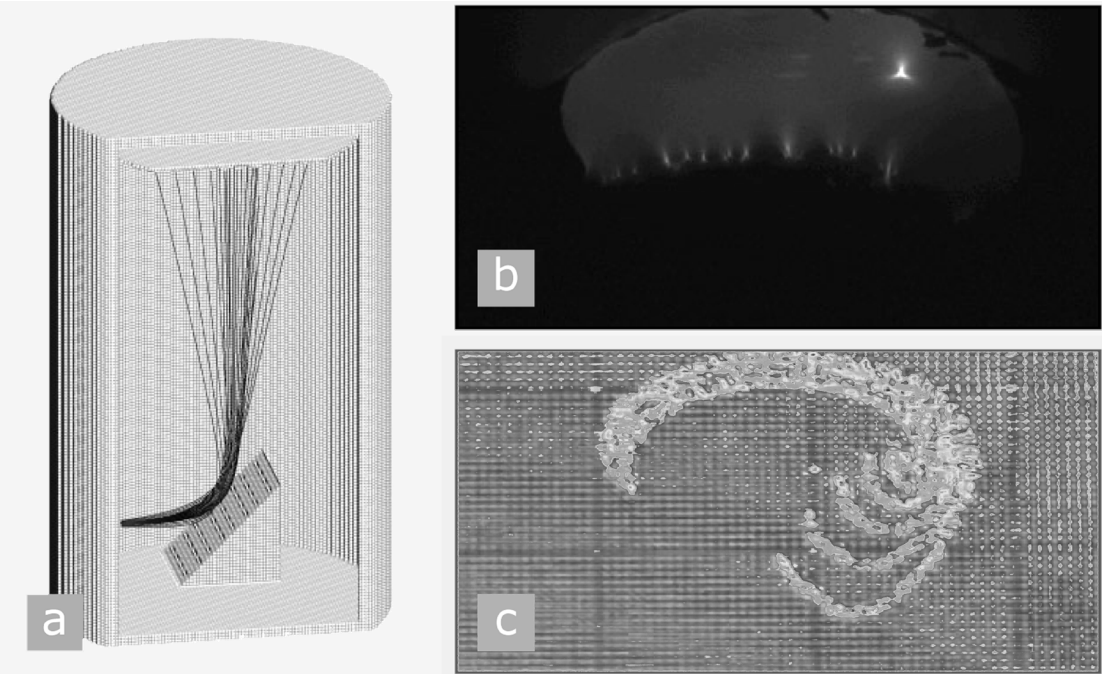

Figure 3.13: Experimental and simulated reflection images at 45 degree beam incidence: (a) experimental setup, (b) experimental image, (c) simulated image.

but a complicated caustic curve results. This finding was confirmed by ray tracing calculations with the SIMION software and is illustrated in figure 3.13. These calculations also predicted that surface imaging requires normal or close to normal beam incidence where the elastically backscattered yield is lowest. A straightforward solution to increasing the backscattered yield is biasing the sample with a negative voltage. This, however, results in another problem: Because the sample acts as the extraction anode for the tip, biasing the sample negatively will result in fewer electrons being emitted. In order to overcome this limitation a separate extraction anode behind the tip is needed, which allows the adjustment of extraction voltage independent of the sample bias. There are, however, two major disadvantages to such an assembly: First, an extraction aperture will act as an einzellens, which introduces aberrations and will decrease the ultimate resolution of the system. Second, with an anode in place the tip cannot be positioned close to the sample any more and high magnifications cannot be achieved. The second problem can be solved by replacing the tip and anode by a more complicated electron gun assembly, which allows one to position a beam cross-over close to the sample surface. Instead of the tip itself, the cross-over will now act as the electron source. This configuration has several advantages: The tip itself can be far away from the sample, which facilitates close to normal incidence onto the sample and also eliminates the problem of

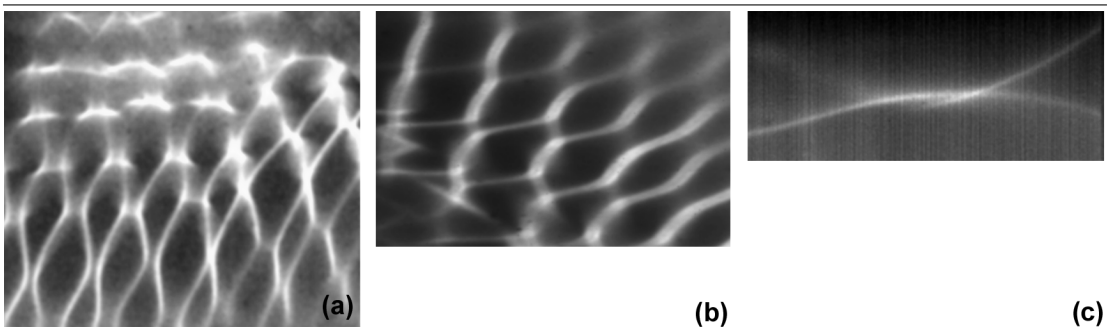

Figure 3.14: First reflection images obtained with the PPM. The images show a copper grid with increasing magnification from (a) to (c).

tip crashes into the sample. The magnification can then be increased electronically by moving the beam cross-over closer to the sample and no more mechanical tip or sample movement is required to change the magnification. There are, however, still some remaining disadvantages: We have to give up the original idea of building a lens-free microscope, which is only resolution limited by the tip size. The aberrations introduced by the gun lenses will now limit the resolution. Also, in order to obtain long electron gun working distances, which is necessary for near-normal incidence, the beam defining aperture in the gun needs to be small in order to reduce aberrations. This results in small convergence angles, which in turn reduces the size of the projected image so that an additional projection lens before the micro-channel plate might be needed. As initial experiments using only an extraction aperture at close to normal incidence have been successful (figure 3.14), a suitable gun is currently being designed in collaboration with the electron microscopy division of the Hitachi High Technology Corporation (figure 3.15).

3.5.3 Outlook – Possible Application for Defect Review

It is our final goal to utilize the point projection microscope for defect review on silicon wafers. Current electron beam tools available for this task face a great number of limitations: As structures of micro-devices decrease rapidly, commonly used scanning electron microscopes need to be operated at smaller and smaller spot sizes. Decreasing the spotsize, however, leads to a reduced beam current and consequently longer image acquisition times to obtain satisfactory signal-to-noise ratios. Newly developed aberration correctors will be able to help solve this problem, but only at the expense of decreased depth of field. This will make the imaging of commonly encountered high aspect ratio structures difficult and might mandate the slow acquisition of through-focal-series. The largest limitation, however, is due to the fact that conventional microscopes need to scan the wafer pixel by pixel, which is an extremely slow process and turns SEMs into a bottleneck of any fab line. The point reflection microscope may offer a solution to many

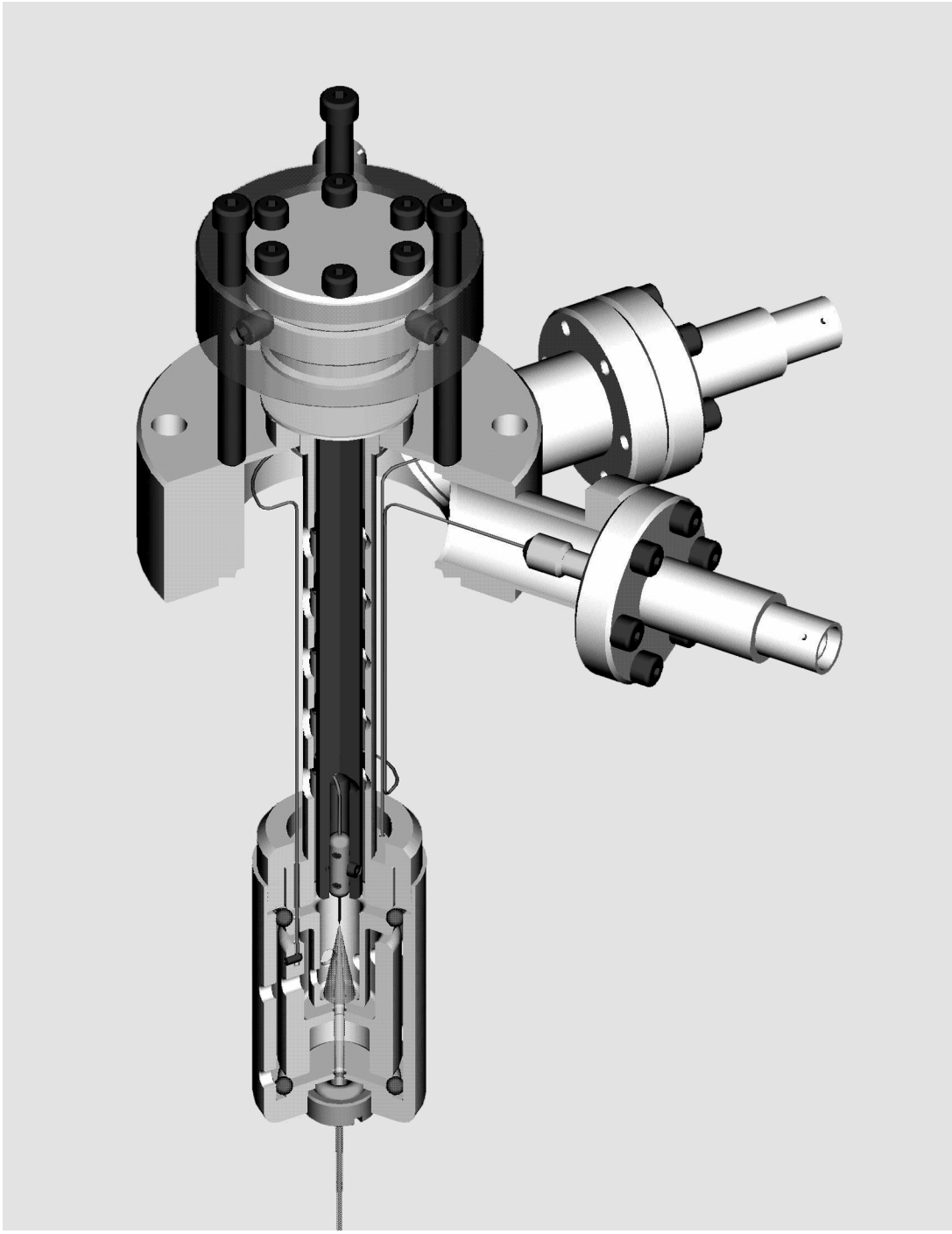

Figure 3.15: Prospective design of an electron gun for the point projection microscope with three electrodes.

of these problems. Because of the (almost) lens-less design electron-optical limitations to the performance will be less dominant. It can operate faster as it acquires a whole image at once and not by pixel by pixel scanning. In addition, since coherent electrons are used to generate the image, the resulting hologram contains three dimensional information of the wafer surface and depth of field problems are avoided. The remaining problem of the image reconstruction does not pose a limitation to a potential use in defect review, as the recorded holograms do not need to be reconstructed to obtain an image. It would be only necessary to compare them to a hologram recorded on a defect-free prototype to find whether or not defects are present. Finally, the low operating voltages will also minimize beam damage to the wafers, especially as the use of beam sensitive organic materials, which have started to replace silicon oxide in semiconductor devices, becomes more and more popular.

Microscopes and telescopes actually confuse the human mind.

Johann Wolfgang Goethe

Off-Axis Holography in the Field Emission TEM 4

4.1 The HF-2000 Field Emission TEM

The Hitachi HF-2000, shown in figure 4.1, is a 200 keV transmission electron microscope. It is equipped with a cold field emission gun, an electron biprism after Möllenstedt and a Gatan slow scan CCD camera to digitally record images. With a spherical aberration coefficient of the objective pole piece of $C_s = 1.2$ mm and a chromatic aberration coefficient of $C_c = 1.4$ mm, the instrument is capable of 0.23 nm point resolution.
The electron source consists of a triple-shielded cold field emission gun, located on a chip, which can be mechanically and electro-magnetically aligned. The virtual source of the gun can be adjusted with a two-electrode gun lens (V1 and V2). Below the gun lens a 6 step accelerating field boosts the electron beam to the operating voltage of 200 keV. The illumination system consists of a double condenser system (C1 and C2) and an astigmatism correction system. Electro-magnetic deflector elements allow for beam tilt adjustment over a 2 degree range. A movable condenser aperture strip contains a 300 μm, a 100 μm, a 50 μm, and a 10 μm aperture. Specimens can be inserted via a side entry concentric goniometer stage. A cold finger in the objective lens helps to reduce sample contamination. The rotation-free imaging system consists of two intermediate (I1 and I2) and two projection lenses (P1 and P2). Images can be viewed on a fluorescent screen and recorded using photographic plates or a Gatan multi-scan CCD camera with a 1024 by 1024 pixel array.
The TEM is equipped with two turbo molecular pumps, dry pumps, three ion pumps, and a liquid nitrogen cooled trap. A column vacuum of $1.5 \cdot 10^{-6}$ Pa and a gun vacuum better than 10^{-8} Pa can be obtained.
The Möllenstedt biprism can be inserted below the first intermediate lens. The biprism fiber is movable in the xy-plane and fully rotatable.

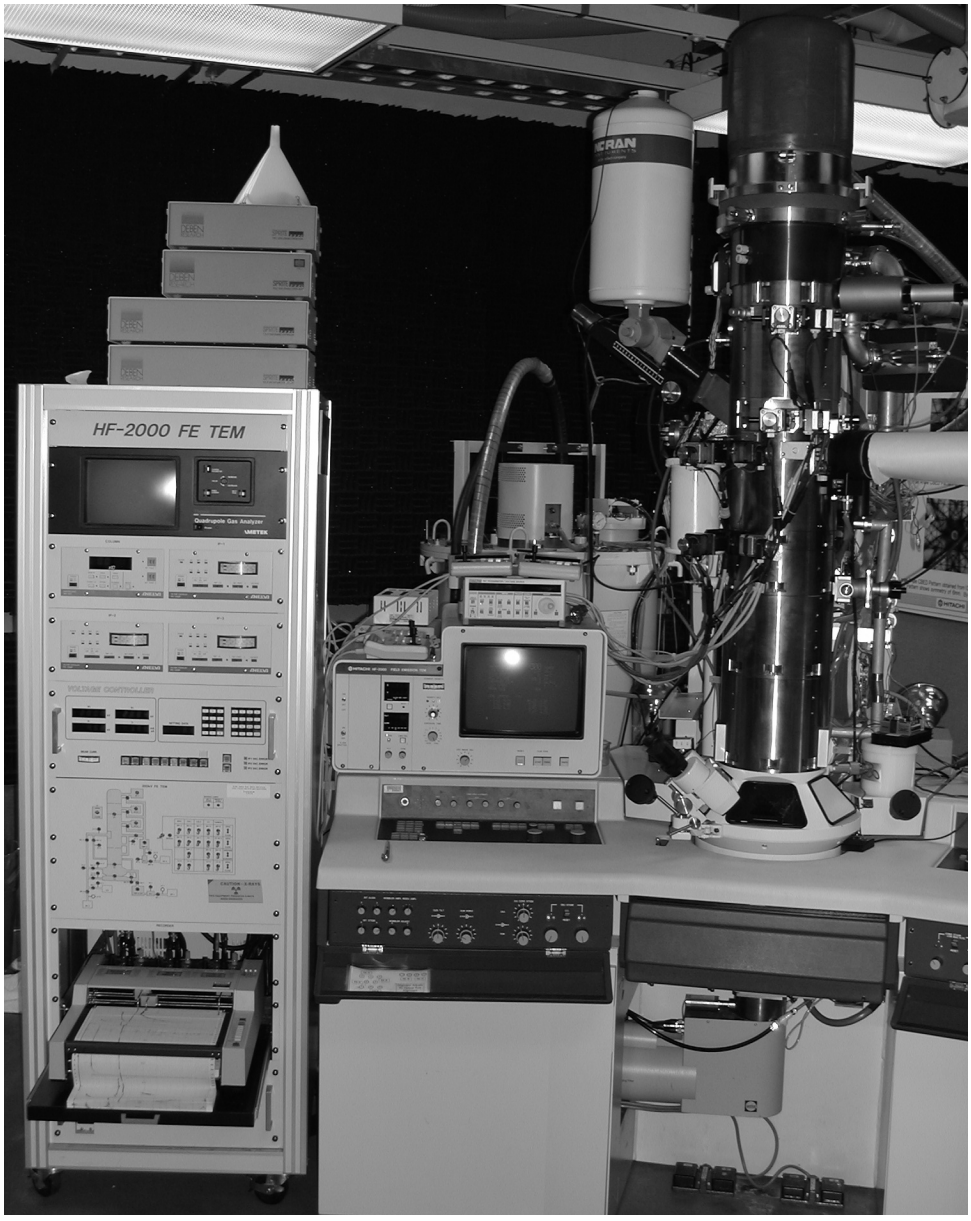

Figure 4.1: The Hitachi HF-2000 cold field emission TEM. The photograph shows the voltage and vacuum control unit on the left side and the main console and microscope column. The camera control units are not shown.

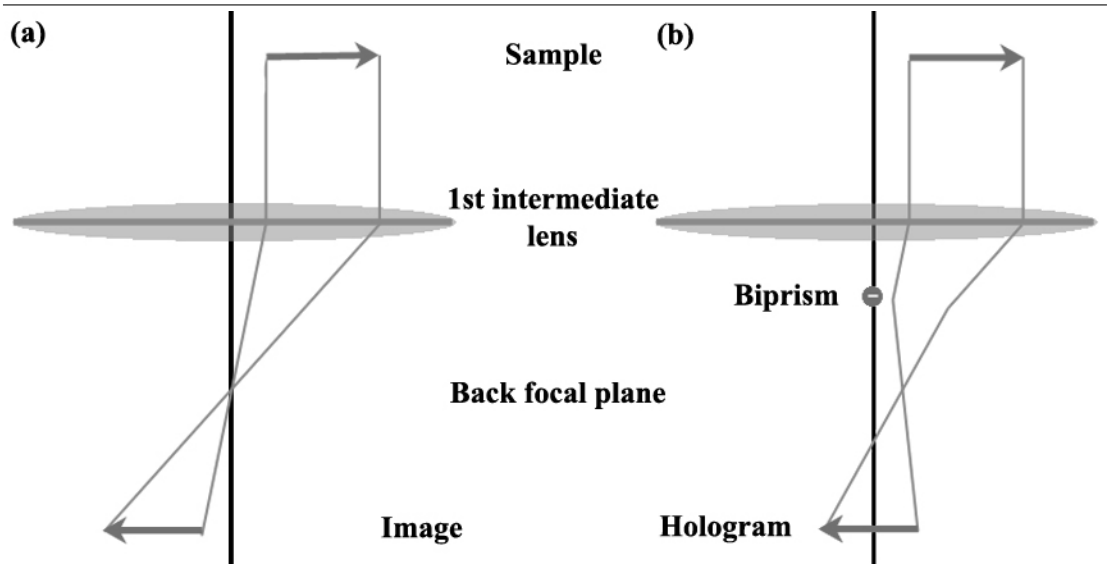

Figure 4.2: Ray paths for low magnification holography in the HF-2000 FE-TEM. The objective lens is turned off, the first intermediate lens forms the hologram and the second intermediate lens together with the projector lenses magnify the hologram. (a) Ray path without biprism. (b) Ray path with a negatively charged biprism.

4.2 Low Magnification Holography Mode

In the standard arrangement for low magnification holography the objective lens of the electron microscope is switched off and the sample is imaged with the first intermediate lens. By de-excitation of the first intermediate lens its focal length is increased, such that the first image plane is located slightly above the second intermediate lens (see figure 4.2). A negatively charged biprism fiber above the back focal plane of the first intermediate lens will deflect electrons on both sides closer to the optical axis, so that rays from both sides of the biprism overlap and form a hologram. In order to achieve the highest possible magnification of the hologram the remaining intermediate lens and all projection lenses are fully excited. An overall magnification of the sample by a factor 2500 can be achieved. Table 4.1 shows typical parameters for this setup.
As discussed before, an increase in fiber voltage increases the overlapping angle and the interference width while decreasing the fringe spacing. Unfortunately, at the same time the spatial coherence decreases, because the distance between the virtual sources is increased. This decrease in fringe contrast ultimately limits the maximum achievable interference width. Frost has developed an improved low magnification mode, in which the objective lens is weakly excited. [33] In this arrangement the objective lens acts like an additional condenser lens rather than an imaging lens. With increasing objective lens current the beam incident on the intermediate lens becomes less divergent or even

Table 4.1: Dependence of biprism voltage U_f, interference width Δ, fringe contrast μ, and point resolution in low magnification holography mode. The lens settings are as follows: C1= 1.30, Obj=0.00, I1=0.86, I2=3.00, P1=3.00, P2=4.50.[33]

U_f in V	Δ in μm	μ in %	point res. in μm
-14.0	3.0	33.3	0.30
-17.0	3.6	26.6	0.33
-20.0	4.2	17.0	0.28
-23.0	4.9	12.7	0.25
-26.0	5.5	10.8	0.22
-29.0	6.1	6.5	0.19
-30.0	6.8	4.0	0.17

convergent. This change in illumination does, in practice, not affect the interference width but decreases the angle under which the two beams overlap by moving the virtual sources upwards. Table 4.2 shows typical results obtained under such a setup.

4.3 Medium Magnification Holography Mode

In order to achieve higher magnifications than the one obtained in the low magnification mode, the objective lens of the microscope has to be used as an imaging lens. Standard high magnification operation of the objective lens and all consecutive lenses, however, results in an overall magnification of the hologram of 500000 to 1.2 million times. This magnification is much too high to image, for example, the semiconductor devices discussed as part of this work, as the field of view is not large enough. Unfortunately, it is not possible to simply turn down the magnification control of the microscope, because this will result not only in a demagnification of the sample but also in a demagnification of the whole hologram, and the effective interference width becomes too small to be useful, as illustrated in figure 4.3.
A way to overcome this problem is to excite the objective lens more strongly than usual as shown in figure 4.4. This decreases its focal length resulting in a smaller than usual image of the specimen. The focal length of the first intermediate lens is then chosen so that it acts as a magnifier, creating a virtual image above the real image of the objective lens. This virtual image is magnified further by a fully excited second intermediate lens. If a negatively charged biprism is now inserted above the back focal plane of the second intermediate lens, rays on both sides of the biprism will be deflected towards each other. Unlike the low magnification case, the second intermediate lens now forms the hologram. The remaining two projection lenses are fully excited to magnify the fine interference fringes as much as possible. This setup allows an overall magnification of 15000 times, which can be slightly varied by changing the sample height. To assess the phase resolution of our instrument in medium magnification mode we record two empty

Table 4.2: Dependence of biprism voltage U_f, interference width Δ, fringe contrast μ, and point resolution in low magnification holography mode with the objective lens weakly excited. The lens settings are as follows: C1= 1.30, Obj=0.37, I1=0.86, I2=3.00, P1=3.00, P2=4.50.[33]

U_f in V	Δ in μm	μ in %	point res. in μm
-40.0	8.4	25.5	0.67
-50.0	10.6	13.7	0.54
-60.0	12.7	8.8	0.48
-70.0	14.8	5.0	0.39
-80.0	16.9	2.5	0.34

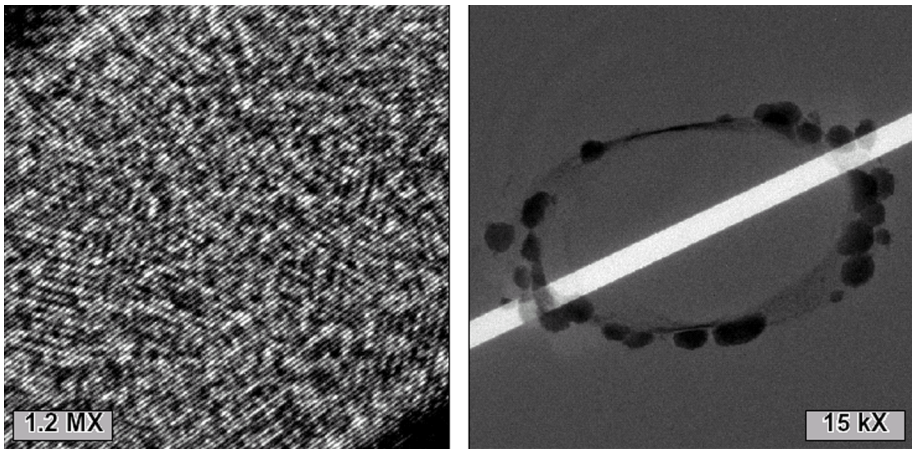

Figure 4.3: If the TEM is operated in its normal imaging mode a very high magnification of 1.2 million times results. This is shown on the left micrograph of a bacterium. In this case the field of view is not large enough to image the entire bacterium. When decreasing the overall magnification to obtain a hologram of the whole bacterium the interference pattern is de-magnified, too, by the same amount as the overall image and the interference width is not large enough to cover the whole field of view.

holograms under indentical conditions. Using one hologram as the image and the other one as the reference image a reconstruction can then be performed, which results in a flat phase image. The standard deviation in the flat part of this phase image gives the limit in phase resolution. In medium magnification mode of the Hitachi HF-2000 a phase resolution of about $2\pi/130$ rad can be measured using this method.
In a second medium magnification setup the objective lens is set to its standard operating value while all the other lenses are adjusted as described in the previous paragraph. In this configuration magnifications around 180000 times are possible. The advantage of this mode is that the objective lens operates at its optimum excitation, and lens aberrations are therefore small.

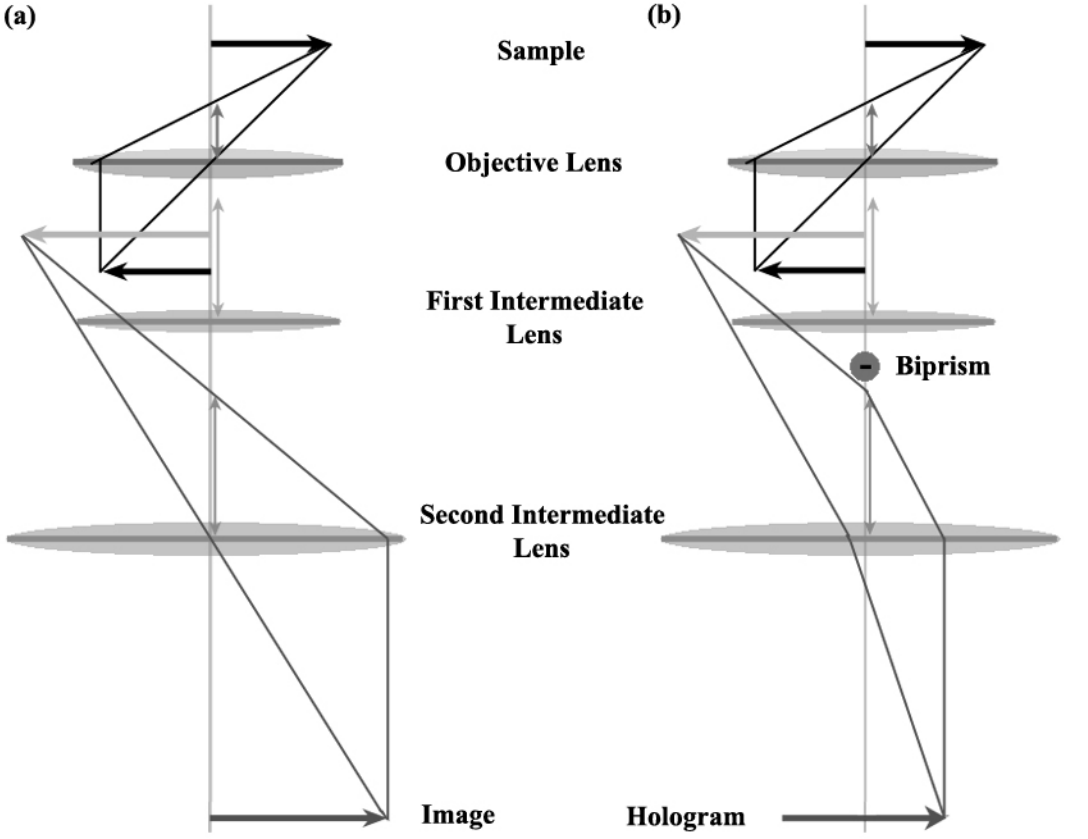

Figure 4.4: Ray paths for medium magnification holography in the HF-2000 FE-TEM. The objective lens is more strongly excited than normal to decrease the magnification of the first image. The second intermediate lens acts as a magnifier, creating a virtual image. The second intermediate lens forms the hologram, which is magnified by the projector lenses. The arrows along the optical axis indicate the location of the focal points. (a) Ray path without biprism. (b) Ray path with a negatively charged biprism.

Perfection is achieved, not when there is nothing more to add,
but then there is nothing left to take away.

Antoine de Saint Exupery

5 TEM Sample Preparation

Electron microscopists have developed numerous ways to thin materials to electron transparency, ranging from simple mechanical and chemical thinning, microtoning and precision cleaving to complicated ion-milling procedures. Despite the success of these methods for conventional electron microscopy, most of them are only of very limited use for electron holography on doped semiconductor devices, due to a number of extra requirements on a suitable specimen. In this chapter these requirements are outlined, followed by a discussion of several methods for holography sample preparation, which were refined or developed as part of this thesis.

5.1 Requirements for Holography Samples

5.1.1 Optimum Sample Thickness

The optimum sample thickness for voltage profiling of doped semiconductor devices can be estimated by minimizing the phase detection limit given by Lichte [61]

$$\delta\Phi = K\frac{1}{C\sqrt{N_{\mathrm{obj}}}} \tag{5.1}$$

Here N_{Obj} is the number of electrons, which have been transmitted through the sample. The constant K depends on properties of the recording media and details of the instrument used. Its exact value has been discussed in [64] and [19], but it is irrelevant for the following discussion. The constant C denotes the fringe contrast as defined in chapter 2, where we also derived the equation

$$C = \frac{I_{\max} - I_{\min}}{I_{\max} + I_{\min}} = \frac{2AA_{\mathrm{obj}}}{A^2 + A_{\mathrm{obj}}^2}. \tag{5.2}$$

The amplitude of the elastically scattered electron wave A is attenuated by the sample according to

$$A_{\mathrm{obj}} = A\, e^{-t/2\lambda_{\mathrm{i}}}. \tag{5.3}$$

Thus, the number of elastically scattered electrons decreases according to

$$N_{\mathrm{obj}} = N\, e^{-t/2\lambda_{\mathrm{i}}}. \tag{5.4}$$

Here t is the sample thickness, λ_{i} the inelastic mean free path, and A and N denote the electron wave amplitude and the number of transmitted electrons with no sample present. The phase shift of the electron wave by a potential V on a sample of thickness t was shown in chapter 2 to be

$$\Phi = C_E V t. \tag{5.5}$$

Our goal is to maximize equation (5.5) while minimizing equation (5.1), which is equivalent to solving the equation

$$\frac{d}{dt}\frac{\Phi}{\delta\Phi} = 0. \tag{5.6}$$

Substituting equations (5.1) through (5.5) into the last equation results in an optimum sample thickness

$$t_{\mathrm{opt}} = 2\lambda_{\mathrm{i}}. \tag{5.7}$$

For 200 keV electrons in silicon this value computes to approximately 200 nm.

5.1.2 Geometrical Limitations

As discussed in chapter 2, part of the electron wave forming the band of interference fringes has to travel through vacuum only, while another part should illuminate the area of interest on the sample. The interference width Δ, however, is very limited and depends on the magnification settings of the microscope. In low magnification mode, with a point resolution of 200 nm, Δ is about 5.5 μm. In medium magnification mode, useful for imaging of semiconductor devices, which offers about 3 nm to 6 nm point resolution, Δ ranges from 200 nm to 800 nm. This puts a severe constraint on the sample: The feature of interest has to be located within a few hundred nanometers of the edge of the sample. The task to locate sub-micron features and exposing them to the sample edge while thinning the sample to 200 nm thickness is of great difficulty, not only if using mechanical techniques for sample preparation but even with highly site-specific tools such as focused ion beam systems (FIBs).
We have seen in chapter 2 that the phase signal measured from the hologram is proportional to the potential throughout the sample times thickness. When trying to map out small potential changes (for example the potential drop over a pn-junction) thickness changes of the sample can mask the potential changes under investigation and make a quantitative analysis difficult. Thus a simple sample topography is desirable.

5.1.3 Surface Amorphization

Several tools for TEM sample preparation such as FIBs utilize 30 to 50 keV ion beams to remove material from the sample. While this stands out as a highly efficient method to thin the area under investigation, the sample surfaces are often amorphized as deep as 25 nm on each side.[56] A detailed study of ion damage in semiconductor materials has been compiled by Barna et al. [7]. According to Rau et al. [90] these layers do not contribute to the voltage signal of a pn-junction and have to be accounted for when interpreting the phase signal. It is thus desirable to minimize these amorphous layers as much as possible during the sample preparation.

5.2 Methods for Sample Preparation

5.2.1 De-Layering of Semiconductor Samples

Todays semiconductor devices are composed of several layers of different materials, which are stacked above the actual CMOS transistors. For example an Intel Pentium III^{TM} processor contains six layers of circuitry. We will give a brief overview about how to remove these layers in order to access the doped source-drain regions, which are of interest for this thesis.

Parallel Lapping: The most straight forward way is to remove layers on a polishing wheel. Great care is necessary to make sure that the sample is polished exactly flat. A polishing cloth, such as the ones commonly used for final polishing of TEM specimens, together with a 0.05 μm colloidal silica suspension should be used. For devices containing copper circuitry a very soft polishing cloth should be chosen as copper tends to smear out.

Packaging Remains: Remains of the packaging materials on the dye can be removed with boiling sulfuric acid.

Silicon Nitride: Most devices are covered by a silicon nitride passivation layer, which can be removed by a 5 minute dip in boiling 80% phosphoric acid at 150°C.

Silicon Oxide: A large variety of different so-called buffered oxide etch solutions are available with different etch rates at room temperature. These solutions mainly contain hydrofluoric acid buffered with ammonium fluoride. Surface reactants are often added to ensure uniform wetting of the etched surfaces.

Tungsten: Tungsten interconnects are most effectively removed using a 1:1 mixture of 30% H_2O_2 and 97% sulfuric acid boiling at 140°C. The sample should be agitated in the solution for about five minutes.

Poly Silicon: A 1:4 mixture of KOH and H_2O at 55°C will remove a poly silicon gate layer in about three minutes.

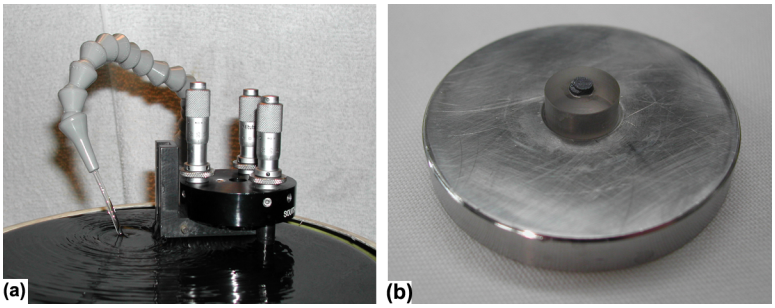

Figure 5.1: Polishing fixtures: (a) Tripod polisher on a polishing wheel. (b) Sample mounted on a glass stub in the parallel lapping fixture.

Silicide: Many forms of silicide layers can be dissolved with a 1:1:1 mixture of acetic acid, ammonium fluoride, and water.

N-Doped Silicon: A 30:1 to 200:1 mixture of HNO_3 and hydrofluoric acid will etch n-doped silicon selectively. The etch speed is very high so a few second dip in the solution followed by a rinse in water is enough.

Recently dry plasma etching systems have become available, which offer more controlled etch rates and better material selectivity. If such a system is available it should be used instead of wet chemical etching.

5.2.2 Tripod Polishing

It is possible to wedge polish silicon to electron transparency. To this end a so-called tripod polisher is used, consisting of a glass stub attached to a metal plate with three teflon feet, the height of which can be adjusted independently by micrometer screws (figure 5.1 (a)). First the sample is polished carefully to remove any layers covering the feature of interest. The exposed surface can then be protected with a thin glass slide glued on with high strength epoxy (Gatan G-1 epoxy^{TM} or Allied epoxy bond 110 two-part adhesive^{TM}). Then a cross-section of one side of the feature of interest is prepared by parallel lapping with a series of lapping films on a polishing wheel ranging from 30 μm to 0.1 μm grain sizes, followed by a final polish with 0.01 μm slurry on a soft polishing cloth. The sample has to be carefully inspected for scratches under an optical microscope in darkfield mode. After this the glass stub and the three feet of the tripod polisher are all adjusted to have the same height and carefully leveled off by parallel lapping with lapping films down to a 3 μm grain size. The sample is bonded to the glass stub with high strength acetone-soluble glue (e.g. Loctite prism 46040 instant adhesive^{TM}), with the polished side facing the stub. The sample is thinned on the stub to about 50 μm thickness. A wedge angle is created by advancing the two rear feet of the polisher. The sample is polished further with finer and finer lapping films. When

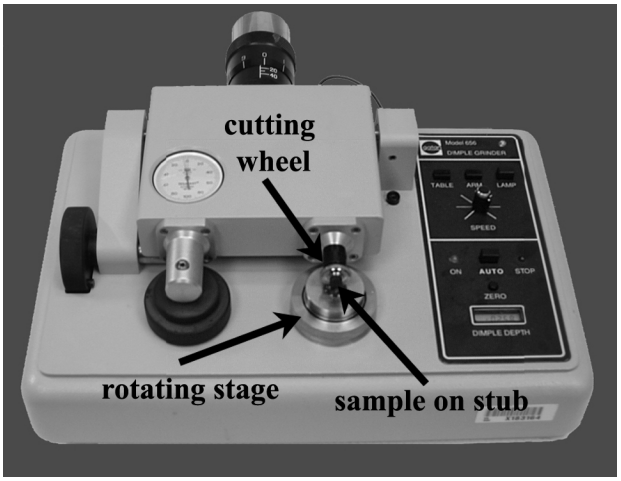

Figure 5.2: With a dimpler silicon samples can be conveniently thinned to electron transparency.

the sample appears orange in transmitted light a short final polish with a 0.01 μm slurry can be done until fringes along the thin edge appear in transmitted light. The sample is soaked in acetone until it floats off the stub, rinsed several times with acetone and finally with ethanol and glued to a TEM grid. With a precision ion polishing system (PIPS) the sample receives a final touch. The PIPS consists of two ion guns, one above and one below the sample, shooting two beams of Ar^+ ions with energies between 8 keV and 2 keV onto the rotating sample. The ion beam of the PIPS has to be modulated not to hit the rotating sample directly on the thin edge. Ion beam voltages between 6 kV down to 2 kV are typically used at glancing beam incidence.
While this method easily produces electron transparent wedge-shaped samples, site specific thinning is extremely difficult. A major problem is posed by the protective glass slide glued on the sample, which has to be removed completely in the final polishing steps (it would charge up under the electron beam in the microscope otherwise), without destroying the area of interest.

5.2.3 Dimpling and Ion Polishing

Dimpling is a standard method for thinning TEM samples, since the technique reliably produces electron transparent TEM specimens. A dimpler, as shown in figure 5.2, consists of a rotating stage holding the sample and a rotating grinding or polishing disk on a weighted arm, which cuts into the sample. Conventional dimpling procedures, however, result in sample shapes inappropriate for electron holography, namely a 3 mm diameter disk of 50 μm height at the rim, which becomes thinner towards the middle, where thicknesses well below 100 nm can be achieved. To produce dimpled samples

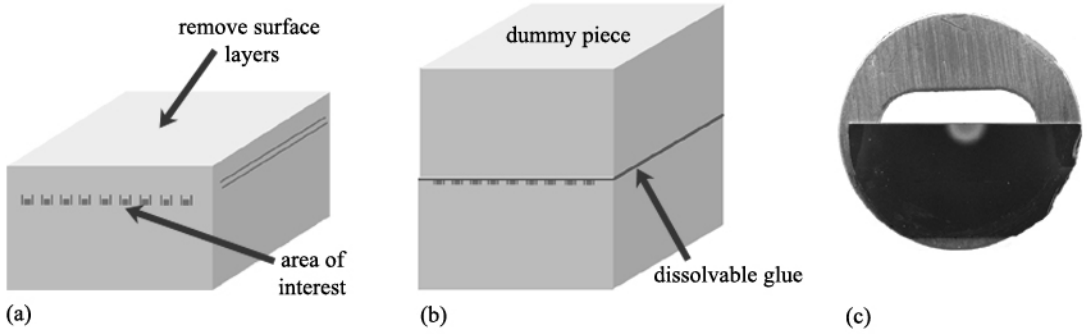

Figure 5.3: Sample preparation for holography by dimpling: (a) Top layers above the area of interest need to be removed by parallel lapping. (b) A dummy silicon or glass piece is glued on with dissolvable high strength glue and the sample is thinned for dimpling. (c) After dimpling the sample can be cleaned by ion polishing.

which allow for a reference wave the following method can be used (see also figure 5.3). As described in section 5.2.2 the area of interest is almost exposed to the surface. Then a polished "dummy" piece of silicon is glued face-to-face on the sample with acetone-soluble high strength glue and cured for at least 24 hours. If site-specific thinning is required, a thick glass slide can be used instead the dummy silicon piece, so that the sample surface can be observed with an optical microscope. The stack is then cross-sectioned with a slow speed saw into several flat pieces. With an utrasonic drill 3 mm diameter disks are cut out of the flat pieces. One side of a disk is then polished with diamond lapping films of decreasing grain size down to 0.1 μm grains, followed by a final polish with a 0.01 μm slurry until no more scratches are visible in an optical microscope or an SEM. The polished side is glued with the acetone-soluble high strength glue to a glass stub, which has been leveled in a parallel lapping fixture with at least a 3 μm lapping film. The parallel lapping fixture should be designed to hold the same size glass stub as the dimpler (see figure 5.1 (b)). After the glue has cured the sample is thinned using the parallel lapping fixture and diamond lapping films down to a 3 μm or 1 μm grain size, until a thickness of 50 μm is reached. The sample on the glass stub is then transferred to the dimpler and aligned with great care so that the dissolvable glue-line is centered. With a grinding wheel and a 3 μm slurry the sample is thinned to about 10 μm thickness. The dimpling is continued using a polishing wheel and a 1 μm slurry until the thinnest area of the specimen appears dark red in transmitted light under an optical microscope. Using a 1/4 μm slurry the sample is dimpled until it exhibits a light orange color in transmitted light and optical fringes appear in the thinnest area. The stub with the sample can then be removed from the dimpler and soaked in acetone until the sample floats off in two parts. After rinses in acetone and then ethanol the two half disks can be glued on one sample grid each and polished in an ion polishing system as

described in section 5.2.2.
The method outlined here produces reproducible large electron transparent areas with the features under investigation close to the sample edge. The specimens have a slowly varying surface topography and are virtually free of scratches and dirt if sufficient care is taken during the preparation.

5.2.4 Sample Preparation with Focused Ion Beam Systems

5.2.4.1 The Focused Ion Beam System

A focused ion beam workstation (FIB) operates similar to a scanning electron microscope (SEM) in that both instruments emit charged particles from a source, focus them into a beam through electromagnetic and electrostatic lenses, and then scan this beam across small areas of the sample using deflection plates or scan coils. Both instruments are used for high resolution imaging by collecting the secondary electron emission produced by the interaction of the beam with the sample surface.
Where a FIB differs from an electron microscope, is that instead of using electrons to form its imaging beam, the FIB uses gallium ions from a field emission liquid metal ion (FE-LMI) source. Within reasonable beam currents an electron beam is non-destructive, but since gallium ions are several orders of magnitude more massive than electrons, a FIB's ion beam mills the sample surface as it images it. Unfortunately, an ion beam will not etch through unlimited thicknesses of material. Depending on such variables as sample composition, mill area, beam parameters, and whether an enhanced etch process is used, the maximum aspect ratio of a FIB milled hole varies from about 3:1 to greater than 10:1. A selection of different size apertures and column electrode settings allows the operator to choose from a variety of different beam specifications ranging from high current and fast milling beams with poor resolution and broad beam profiles to small current and slow milling beams with a small and well defined probe size. Due to its high accuracy the FIB is an ideal tool for site specifically preparing TEM samples to very precise specifications.
A focused ion beam can also be used to deposit material. Some organic and organometallic compounds have high enough vapor pressures so that they may be injected as a gas into the vacuum chamber where they are adsorbed onto the sample surface. If for example a platinum organometallic molecule is injected and struck by the incident gallium ion beam, the chemical bonds holding it together break, releasing the carbon atoms into the FIB's vacuum chamber while the heavier platinum atom is deposited as an electrical conductor onto the sample surface. The deposition process for other materials is similar.
When preparing a TEM specimen with the FIB, the sample needs to be imaged several times with the ion beam. In order to avoid damage of the area under investigation a protective layer of metal has to be deposited on the surface. Mordern dual beam systems combine an SEM-column with the an ion-beam system in one workstation allowing for destruction free monitoring of the ion milling process with the electron beam. For

Figure 5.4: Single and dual beam FIB systems: (a) The Hitachi FB-2000 single beam FIB. (b) The FEI Strata 235 dual beam system.

the specimen preparation for this thesis the FEI Strata 235 dual beam system and the Hitachi FIB FB-2000 single beam system were used (Figure 5.4).

5.2.4.2 Problems - Causes and Cures

When preparing samples for electron holography, we are primarily concerned with the following three issues: Firstly, since FIBs typically work at beam voltages between 30 and 40 keV, they can cause substantial damage to the specimen surface. Especially on single crystal silicon samples both surfaces of the thinned membrane will be amorphized and build dead layers as discussed above. Only recently FIBs have become available, which can operate at 10 keV such as the FEI Stata 235 or the Hitachi FB-2100 dual beam systems. At such reduced beam voltages, however, beam current and beam quality is significantly reduced.
Secondly, the protective metal layer covering the sample does not allow for a reference wave with typical medium magnification settings of the microscope. Even if a wide enough interference width is achieved charging of the metal layer in the electron beam can be observed. This adds an unknown potential distribution making a quantitative evaluation of the phase image difficult. In addition to this the top surface of the sample is usually amorphized significantly during the metal deposition process as discussed in [52] (see figure 5.5).
Thirdly, semiconductor devices consist of a complicated system of different layers and materials next to silicon, including copper, tungsten, SILK^{TM}, silicon nitride, and silicon oxide to name only a few. Since all these materials thin at different rates under the ion beam, shadowing and differential thinning artifacts as shown in figure 5.6 are commonly observed on FIB-milled samples. These “curtaining” or “waterfall” effects result in a

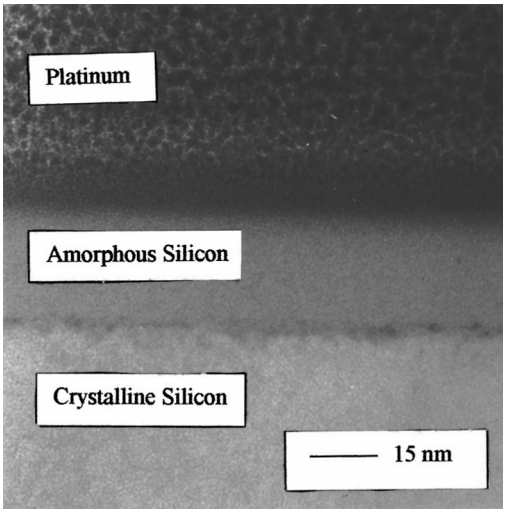

Figure 5.5: Silicon lattice damage from platinum deposition (TEM-image). The amorphous to crystalline boundary is approximately 20 nm thick. (Figure reproduced with friendly permission from Gerald Lucovsky, editor Journal of Vacuum Science and Technology A, [56])

complicated sample topography, making a distinction between potential contributions and thickness contributions to the phase signal difficult. A more detailed description of these and other problems can be found in [56]. To avoid this problem metal layers on semiconductor samples should be removed as far as possible before thinning the sample. A better method is possible, if the FIB is equipped with an in situ micromanipulation system: The area of interest is cut out as a larger piece and attached upside down to a sample grid. The sample can then be thinned with the focused ion beam coming from the substrate side.

In the remainder of this section two procedures for preparing FIB-milled holography TEM samples of semiconductor devices, which have been developed and successfully used with an FEI Stata 235 dual beam system, are outlined in detail.
1. The sample is wedge polished with a tripod polisher as described in section 5.2.2 until the thin edge appears red in transmitted light (about 2-3 μm thickness) and mounted on a TEM grid, which has been cut in half.
2. In the dual beam workstation electron beam and ion beam are carefully aligned, the sample is raised to the eucentric height of the stage, and an area of interest is located. To avoid shadowing effects all metal layers of the device are removed with the ion beam until “metal one”, which is the metal layer right above the transistors, is revealed. This is done with the sample titled 55 degrees to the ion beam.
3. In order to avoid ion beam surface damage a thin layer of platinum is deposited with the *electron* beam, followed by the deposition of a 1.5 μm thick layer using the ion

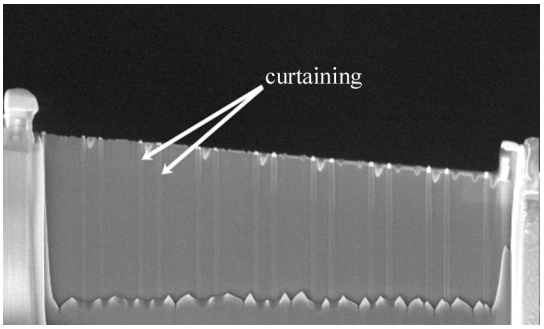

Figure 5.6: SEM image of a FIB-milled specimen. The "waterfalls" are caused by shadowing effects from the slower milling tungsten plugs.

beam.
4. After these preparations the thinning process can start. With the ion beam at 0 degrees with respect to the sample and at 30 keV energy a membrane is thinned into the sample. With decreasing thickness smaller and smaller ion beam apertures are selected starting with a 2700 or 1000 pA aperture until a sample thickness just above 200 nm is reached with a 70 or 11 pA aperture. During the final steps the ion beam is scanned in a special polishing pattern to remove curtaining.
5. In order to achieve an overall flat sample topography versus a wedge shaped one the sample is tilted 2 degrees towards the beam on each side and milled with a 11 pA aperture.
6. To reduce the amount of surface amorphization the membranes are polished for a few seconds with the ion beam at 10 kV and 3 degrees tilt and then at 5 kV and 7 degrees tilt using a 300 pA aperture. When changing the beam voltage for this procedure the ion beam system has to be completely realigned. This should be done on an area of the specimen far away from the thin membrane. Excessive low voltage milling will result in strong curtaining, because differential milling effects between different materials are more pronounced at low voltages.
7. The beam is switched back to 10 keV energy, realigned, and the sample is tilted to a 55 degree angle to the beam. At this point it is recommended to leave the system alone for about 15 minutes to let the stage settle as even slight stage drift will destroy the sample in the following step. After imaging a single frame with the ion beam to locate the features of interest the remaining platinum is milled away as well as any other material above the area of interest. If the sample has a series of transistors next to each other the milling box should be rotated a few degrees, so that the material is removed at an angle exposing the gate oxide on one side of the membrane, while on the other side part of the oxide layer above the transistor is still preserved. This method allows for greater flexibility in choosing the interference width of the holographic fringes, and places the vacuum window as close as possible to the area of interest (Figure 5.7).

An alternative method has been developed, which places the window for the reference wave below the area of interest and leaves the platinum layer intact. For this, after proceeding until step four, a hole is drilled into the sample below the area of interest. This should be done with a rotated milling box as in step seven to increase the chance of hitting the right spot. The edge of the hole adjacent to the area of interest has to be cleaned with small beam apertures and a polishing milling pattern. As the hole is drilled "blindly", i.e. with the feature of interest still buried inside the material, some prior knowledge about the makeup of the sample is necessary. After this, one can proceed with steps five and six described above, leaving out step seven (Figure 5.8).

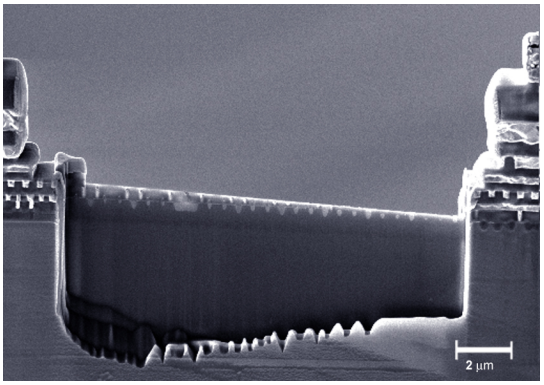

Figure 5.7: SEM micrograph of a FIB-milled sample. The platinum is completely removed and the vacuum reaches the top of the tungsten plugs on the left side while on the right side the spacers are exposed.

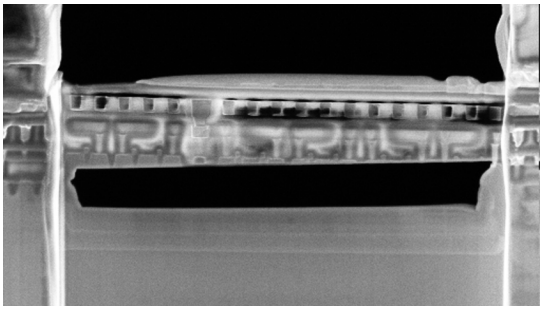

Figure 5.8: SEM micrograph of a FIB-milled sample. In this case the platinum layer is still intact and the hole for the reference wave is located below the area of interest.

Physicists like to think that all you have to do is say, these are the conditions, now what happens next?

Richard Feynman

Holography on Doped Semiconductor Devices 6

Two-dimensional dopant profiling of semiconductor devices has been a highly ranked need in both the simulation and the process integration sections of the International Technology Road Map for Semiconductors since its inception. [1] As early as 1994 Subrahmanyan and Duane have provided important mile-posts for the spatial resolution, dopant concentration accuracy, and range needed for physical two-dimensional dopant profiling of 0.25 μm design rule transistors (table 6.1). [105] Most of these mile-posts have not been met up to today, and IC producers are now calling for dopant profiling technologies to aid with the calibration of their technology computer-aided design (TCAD) process simulators for processes well below the 0.13 μm design rule. As we will discuss, off-axis electron holography has emerged as a viable technique to address this need.

6.1 Voltage Contrast in Doped Semiconductor Devices

In section 2.5 we discussed how the phase of the electron wave is affected by electric potentials. In this chapter we will discuss how this effect can be used to measure the small potential changes dopants cause in semiconductor materials. A summary of this chapter has been published. [109] For simplicity we start off considering a simple step junction consisting of adjacent p-and n-doped areas on a silicon substrate as shown in figure 6.1. We can understand from the band model how such a configuration results in a potential change over the pn-junction: On the p-doped side acceptor levels are located about 50 meV below the conduction band. Hence the Fermi level is raised in the p-doped silicon by an amount depending on the impurity concentration, while it is lowered on the n-doped side, where the donor levels are located just above the valance band. If p-and n-doped materials are brought together the Fermi levels of both sides coincide. This leads to an upward bending of the valence and conduction bands in the

Table 6.1: Summary of 2D dopant profiling requirements for the device simulation of 0.25 μm design rule transistors as disscussed in [105].

		Analysis requirement	
Application	Device Region	Sensitivity (cm^{-3})	Resolution (nm)
Leakage current	Channel	$2 \cdot 10^{17}$	10
	Source/Drain	$1 \cdot 10^{18}$	10
Other circuit effects	Channel	$2 \cdot 10^{17}$	5
(circuit delay, etc.)	Source/Drain	$1 \cdot 10^{18}$	5

p-doped material with respect to the n-doped silicon at the interface, which results in a potential difference (see figure 6.1). These potential changes can be mapped out by holography to high accuracy.
A derivation of the potential drop over a step-pn-junction can be found in many textbooks of condensed matter physics. According to Ashcroft and Mermin [4] the potential V_{pn} over the step junction shown in figure 6.1 is given by

$$V_{\mathrm{pn}}(x) = \begin{cases} V(\infty), & x > d_{\mathrm{n}} \\ V(\infty) - \left(\frac{eN_{\mathrm{d}}}{2\epsilon\epsilon_0}\right)(x-d_{\mathrm{n}})^2, & d_{\mathrm{n}} > x > 0 \\ V(-\infty) + \left(\frac{eN_{\mathrm{a}}}{2\epsilon\epsilon_0}\right)(x+d_{\mathrm{p}})^2, & 0 > x > -d_{\mathrm{p}} \\ V(-\infty), & x < -d_{\mathrm{p}}. \end{cases} \tag{6.1}$$

Here N_{a} and N_{d} denote the dopant concentrations on the p- and n-doped side respectively and d_{p} and d_{n} are the widths of the depletion layers on the p and n side of the junction. By requiring continuity of the potential at $x = 0$ one obtains for the total voltage drop over the junction

$$\Delta V = \left(\frac{e}{2\epsilon\epsilon_0}\right)(N_{\mathrm{d}}d_{\mathrm{p}}^2 + N_{\mathrm{a}}d_{\mathrm{p}}^2). \tag{6.2}$$

The width of the depletion area can be evaluated as follows

$$d_{\mathrm{n,p}} = 105\sqrt{\frac{(N_{\mathrm{a}}/N_{\mathrm{d}})^{\pm 1}}{10^{-18}(N_{\mathrm{d}}+N_{\mathrm{a}})}\epsilon[e\Delta V]_{\mathrm{eV}}}\,\text{Å}. \tag{6.3}$$

Figure 6.2 shows the total voltage drop over one side of a step junction as function of the dopant concentration.
From section 2.5 we know that an electron wave traveling through an area of potential V and thickness t will experience a phase shift as illustrated in figure 6.3. In case of a doped semiconductor this phase shift is given by

$$\Delta\phi(x,y) = C_E\Big(V_0 t + V_{\mathrm{pn}}(t-2t_0)\Big). \tag{6.4}$$

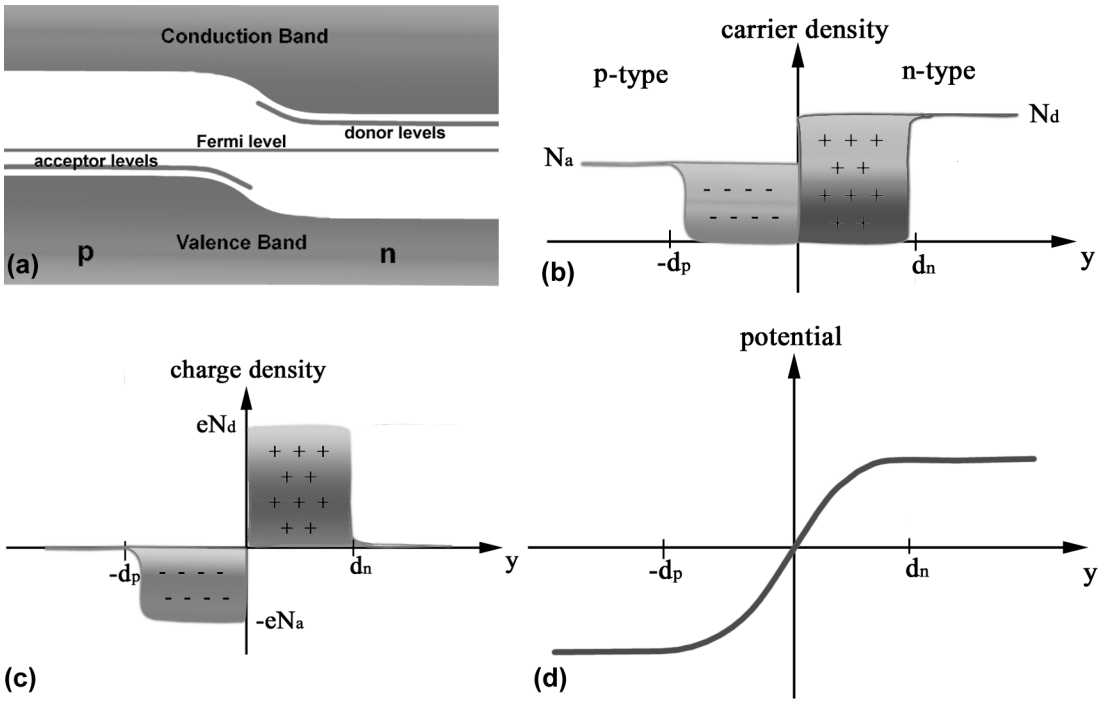

Figure 6.1: The pn step-junction: (a) Simple band model of a pn-junction. The acceptor levels are located about 50 meV above the valence band on the p-doped side, while the donor levels can be found about 50 meV below the conduction band on the n-doped side. As the two sides are brought together the Fermi levels coincide, the bands bend, and a voltage drop over the junction occurs. (b) Carrier density over the step junction. At the junction electrons from the n-site will move to the p-side and occupy available acceptor levels. A negative charge density on the p-doped side and a positive charge density on the n-doped side close to the junction results (c) and a depletion region is formed. (d) Potential over the step junction.

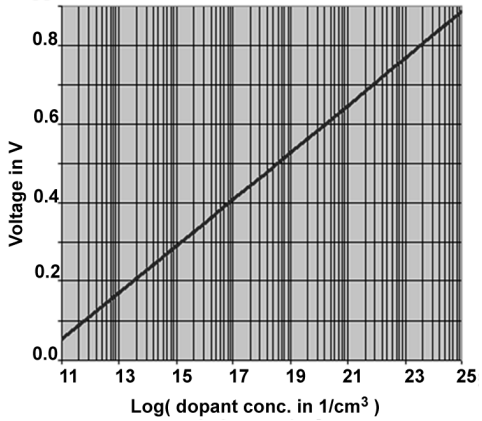

Figure 6.2: Dependence of the total voltage drop over one side of a pn step-junction as a function of dopant concentration.

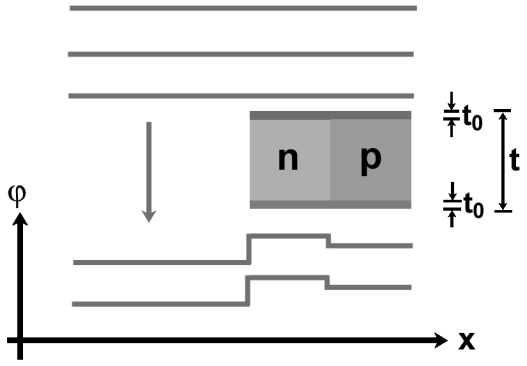

Figure 6.3: Phase change of an electron wave penetrating a doped semiconductor. The shift in phase is affected by both the inner potential of the sample and potential changes due to doping. A dead layer of thickness t_0 can be present on top and bottom of the sample.

Here V_0 is the inner potential of the semiconductor and V_{pn} the potential due to the doping. In order to account for possible dead layers at the sample surfaces, which can result for example from the sample preparation process, the dead layer thickness t_0 has to be subtracted from the overall sample thickness t for both the bottom and the top surface. If during the hologram reconstruction the sideband is chosen so that the phase increases with increasing sample thickness, the phase in n-doped areas will be more advanced and they will appear brighter than the surrounding silicon substrate, while p-doped areas will be darker in the phase image.

6.2 Different Approaches to Thickness Correction

One of the most critical remaining problems concerning dopant profiling with electron holography is the question how to separate sample thickness contributions from contributions of the electrical potential caused by the active dopants to the reconstructed phase image. We will discuss several approaches to solving this problem.

6.2.1 Thickness Correction using the Amplitude Image

As already mentioned in chapter 5 the intensity of an electron wave passing through a sample decays exponentially with the sample thickness according to

$$I = |A|^2 = I_0\, e^{-t/\lambda_{\mathrm{inel}}} \tag{6.5}$$

if diffraction effects can be neglected. Here I_0 is the intensity without the sample, λ_{inel} is the inelastic mean free path, and A is the amplitude of the electron wave. If we solve this equation for the specimen thickness t we obtain

$$t = -2\lambda_{\mathrm{inel}} \log(A/A_0). \tag{6.6}$$

The amplitude of the electron wave can be conveniently obtained from the amplitude image of the reconstructed hologram. The amplitude has to be normalized by dividing it by the vacuum amplitude A_0, which should be chosen to be the average value of all pixels in the reference wave part of the reconstructed amplitude image. Equation 6.6 gives then the desired thickness map of the specimen. This method, which was first proposed by Gajdardziska-Josifovska [38], has the major problem that a wide range of values for the constant λ_{inel} can be found in the literature. This is due to the fact that the majority of these published values have been determined by EELS, where the experimental result for λ_{inel} strongly depends on experimental conditions such a the selection of apertures, beam angles, and specimen tilt. [24] In addition values determined by EELS suffer from the problem that even state-of-the-art EELS spectrometers have an energy resolution of only 1 eV and therefore include a large number of low-loss inelastic events such as phonon scattering in the elastic peak. Hence, they give wrong predictions for the elastic and inelastic mean free paths. On the other hand electron holography is a truly zero loss

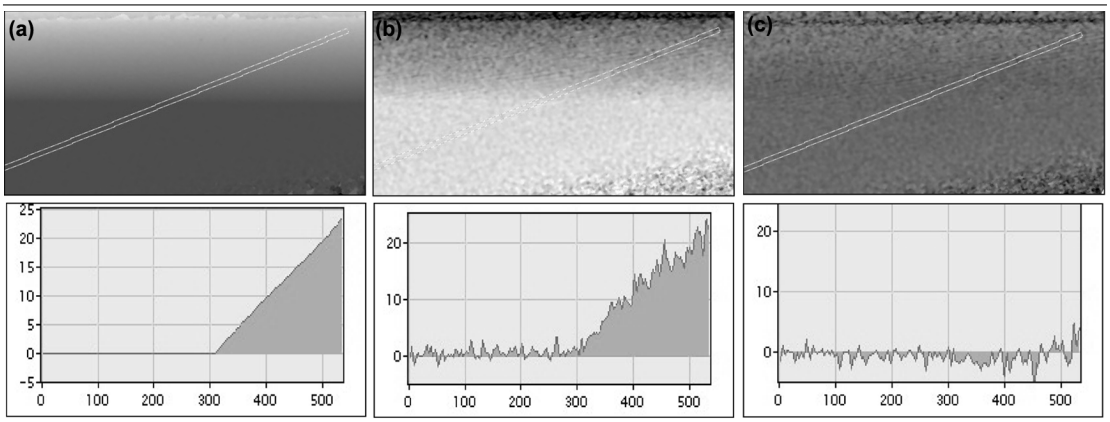

Figure 6.4: Elimination of thickness contributions to the phase image demonstrated on an undoped silicon wedge: (a) Phase image of a silicon wedge with line profile. (b) Logarithm of the amplitude image according to equation (6.6) gives also a wedge shaped thickness profile. (c) The difference between the two images is zero at a constant $K = 2C_E V_0 \lambda_{\text{inel}} = 15.4$ rad.

imaging technique, as only elastically scattered electrons interfere with the unscattered reference wave and contribute to the reconstructed phase and amplitude images. To overcome this problem we substitute the thickness obtained from equation (6.6) into the equation, which describes the phase change of the electron wave

$$\begin{aligned} \phi_{\text{from amplitude image}} &= C_E(V_0 + V_{\text{doping}}) \cdot t & (6.7) \\ &= -2C_E\,(V_0 + V_{\text{doping}})\,\lambda_{\text{inel}} \cdot \log(A/A_0). & (6.8) \end{aligned}$$

We then subtract this phase image from the phase image obtained from the reconstructed hologram to obtain a difference image

$$\Delta\Phi \;=\; \phi_{\text{from reconstruction}} \;-\; \phi_{\text{from amplitude image}}. \qquad (6.9)$$

In an area where no dopant is known to be present and thus any potentials due to doping vanish ($V_{\text{doping}} = 0$) we minimize this difference image (6.9) by varying the constant $K = 2C_E V_0 \lambda_{\text{inel}}$. This overall constant K is then used to calculate ϕ in equation (6.7) and subtracted from the phase image obtained by the hologram reconstruction (see figure 6.4). A short program, which accomplishes this task automatically, is shown in appendix B. Main restrictions to this method result from diffraction effects, which should be avoided at all cost, and Fresnel fringes as they appear in part (c) of figure 6.5. In addition to this the method is severely limited by noise problems as will be shown in the following: The phase image shown in figure 6.5 (a) has a standard deviation in the sample part of about $\Delta\phi = 0.05$ rad. The normalized amplitude image shown in the figure part (b) exhibits a standard deviation of $\Delta A = 0.15$ about an amplitude of

$A = 0.59$. The standard deviation in the $\log(A)$ image is then

$$\Delta\Big(\log(A)\Big) = \frac{\Delta A}{A} = .25. \tag{6.10}$$

In order to obtain the desired thickness map the $\log(A)$ image needs to be multiplied by the constant K, which has a value of 15.3 rad for the images in figure 6.5. This increases the final standard deviation of the thickness map to a value of about 3.8 rad in an area with an overall phase shift of about 8 rad. Compared to the phase image in figure 6.5 (a) with a standard deviation of about 0.07 rad in areas with 8 rad thickness, the level of noise in the thickness map according to equation (6.7) is gigantic. In order to obtain the the line profile shown in figure 6.5 (e), which also suffers from artifacts arising from Fresnel diffraction, about 100 pixels had to be averaged. An obvious solution to the noise problem in the thickness map of the amplitude image seems to smooth it by using a median filter or by filtering out high frequency components in Fourier space. These methods, however, turn out be not very useful. Median filters introduce periodic artifacts and smoothing of the image by high frequency filtering creates artifacts at the sample edges.

6.2.2 Extrapolation

For samples with a simple overall geometry often the best way to eliminate thickness contributions from the phase image is to fit a linear or quadratic function to the phase image in the undoped areas, where the sample thickness is the only contribution to the phase. This function can then be extrapolated into the doped areas and subtracted from the phase image. For the small doped source-drain areas of CMOS transistors, which are often no larger than 100 nm a linear extrapolation of the thickness from the adjacent substrate areas usually works very well.

6.2.3 Convergent Beam Electron Diffraction

Thickness information can also be obtained from analyzing convergent beam electron diffraction patterns (CBED). To obtain a CBED pattern the illumination of the microscope is focussed onto a spot on the sample. The first intermediate lens and all consecutive lenses are adjusted so that the back focal plane of the objective lens, which contains the diffraction pattern of the sample, is imaged. In contrast to conventional selected area diffraction the diffraction spots appear as large discs, which contain fine-structure governed by dynamical diffraction effects. If the sample is tilted to obtain a two-beam condition a set of dark and white fringes will appear in the two visible discs. Kossel and Möllenstedt were the first to link the minimums of this fringe pattern to the specimen thickness [54] and Kelly et al. and Allen [3, 53] have described elaborate data analysis techniques for thickness determination. Finally, Delille et al. have devised an improved fitting method and demonstrated 1% accuracy for thickness determination on a silicon wedge. [20] CBED patterns are ideally recorded with the sample cooled

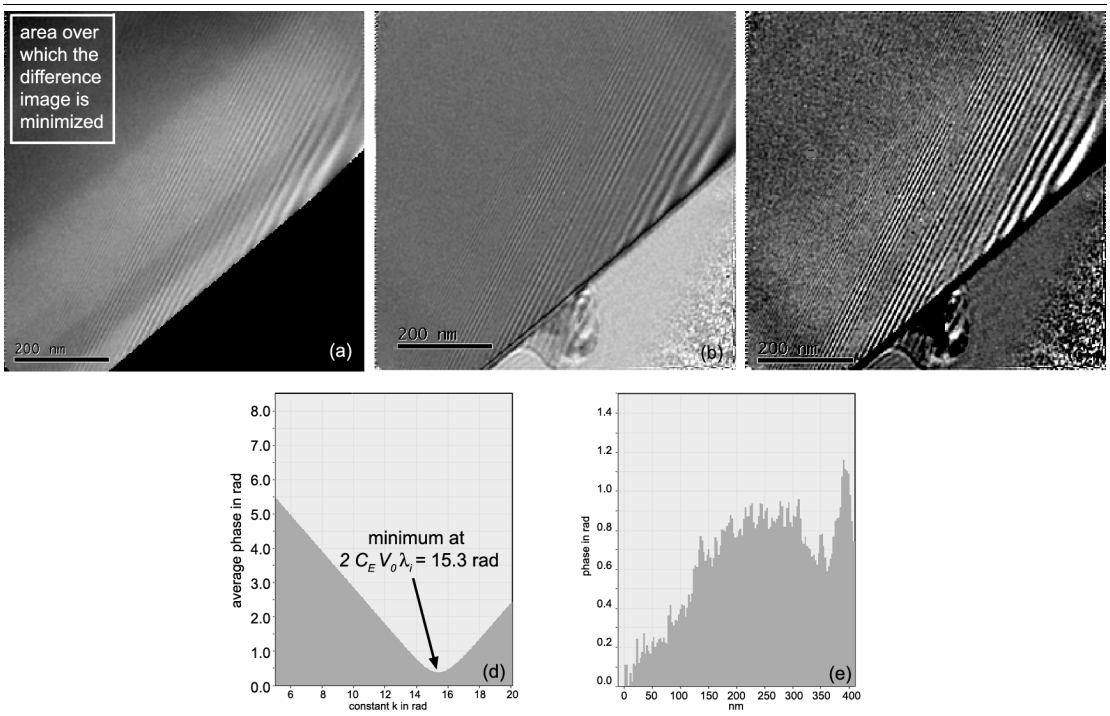

Figure 6.5: Elimination of thickness contributions to the phase image of a silicon sample with 2 blanket boron implants: (a) Phase image of the specimen. The boron implants are visible as brighter areas parallel to the sample edge. (b) Amplitude image of the same area. (c) Thickness-corrected phase image. (c) Average pixel value of the difference image as a function of the constant K. (d) Line profile of the thickness corrected image at $K = 15.3$ rad averaging 100 pixels. The problems due to noise and Fresnel fringes are apparent.

to liquid nitrogen temperature in order to reduce beam damage and to decrease the Debye-Waller factor. To reduce background due to inelastic scattering they should be recorded through an EELS system. Following Delille et al. [20] a linear and a Gaussian background needs to be subtracted from the line profiles of the diffraction discs and a function

$$|\Phi_g|^2(s) = \sin^2\beta \, \sin^2(\pi \Delta k t) \quad \text{with} \quad \beta = \tan^{-1}(1/s\xi_g) \tag{6.11}$$

$$\text{and} \quad \Delta k = \frac{\sqrt{1+(s\xi_g)^2}}{\xi_g} \tag{6.12}$$

is fitted to the result, varying the sample thickness t and the extinction distance ξ_g. The line profiles can be calibrated in terms of the deviation parameter s using

$$s = \frac{\theta}{2\theta_{\mathrm{B}}} \frac{\lambda}{d_{hkl}^2}, \tag{6.13}$$

where θ_{B} is the known Bragg angle, d_{hkl} the spacing of the corresponding lattice planes, and λ the wavelength of the electrons. As dynamical diffraction occurs only on crystalline specimens, the thickness t obtained by this method is the thickness of the crystalline part of the sample only. Diffraction from possible amorphous surface layers will yield rings in the diffraction pattern, which are part of the background. The major disadvantage of this method is that thickness information is obtained at one point only and it is virtually impossible to obtain a thickness map. A further complication arises from the fact that by focusing the illumination onto a small spot on the sample, the specimen contaminates rapidly at this point and knock-off damage occurs at higher beam energies.

6.2.4 Electron Energy Loss Spectroscopy

Instead of using the amplitude image from the reconstructed hologram a zero-loss image can be also obtained with an energy electron loss spectrometer (EELS). If I_t is the total image intensity and I_0 the integrated elastic peak a thickness map can be obtained according to

$$t/\lambda = \log(I_t/I_0) \tag{6.14}$$

where the mean free path $\lambda(\beta)$ depends on the aperture, which limits the maximum recorded scattering angle β. [24] Instrumental background and the unsatisfactory parametrizations of λ limit this method to a 10% error margin. In addition surface excitations will cause an overestimate of the thickness for very thin samples. So far no successful use of thickness maps generated by EELS for thickness correction of holograms has been reported in the literature.

6.3 A Brief Overview of CMOS Technology

As part of this thesis electron holography is applied to real world semiconductor devices it is helpful to discuss the process flow for the production of such devices at this point. Integrated circuits found in todays computer processors are commonly produced in complementary metal oxide semiconductor (CMOS) technology. A so-called n-channel MOS transistor consists of a p-doped silicon substrate, in which n-doped source and drain areas have been implanted at the surface. Located between these source and drain areas is a metal electrode, called the gate, which is insulated from the silicon by a thin oxide layer. In current devices this metal electrode is replaced by a highly doped polycrystalline silicon, but the name "metal oxide semiconductor transistor" remains. With the gate grounded no current can flow between the source and drain regions, as the n-doped source and drain areas form reverse-biased diodes with the p-type substrate in either direction. If however a positive potential is applied to the gate, the resulting electric field attracts electrons from the substrate, a two-dimensional electron gas forms between source and drain region, and current can flow between source and drain. In a p-channel MOS transistor the substrate is n-doped while source and drain consist of p-type silicon. Complementary MOS (CMOS) technology combines both p- and n-channel transistors on the same die. This is done by implanting for example an n-well in the p-doped substrate. The following figure 6.6 will give a simplified step by step overview how CMOS transistors are produced.

Step 1: The production of a CMOS device starts with a highly doped p- or n-type wafer (from here on we assume a p-type substrate), on which a lightly doped epitaxial silicon layer is grown. This layer usually contains a buried oxide layer to reduce current leakage and hence power consumption of the device.

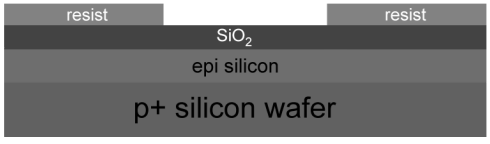

Step 2: A silicon dioxide layer is then grown on the epi-silicon, which will act as a mask for n-well implantation later. The oxide layer is coated with photo resist, which is patterned by exposure with UV light and etching of the exposed areas.

Figure 6.6: CMOS device process flow. Continued on next page...

Step 3: In an etch process the silicon oxide is removed with the remaining resist areas acting as a mask to retain the wanted areas.

Step 4: The n-well is now implanted. During the implantation process the remaining oxide areas act as a mask allowing the incident arsenic or phosphorus ions only to reach the silicon substrate where desired. The wafer is annealed to activate and drive in the implants.

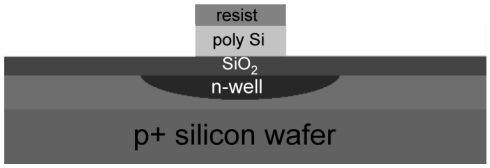

Step 5: The oxide is removed and a new thin oxide layer is grown, which will act as the gate oxide later. The poly silicon layer, which will form the gates of the transistors, is formed on top of the oxide layer and patterned using a second photolithographic process.

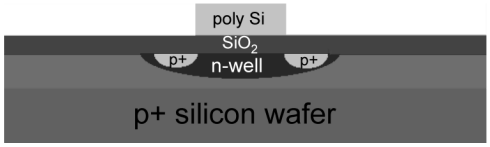

Step 6: A mask for the source and drain implantation is created in another photolithographic process. P-source and drain areas are now implanted. The resist is removed and the process is repeated for the n-type source and drain regions. The implants are activated by a rapid anneal after the removal of all resist.

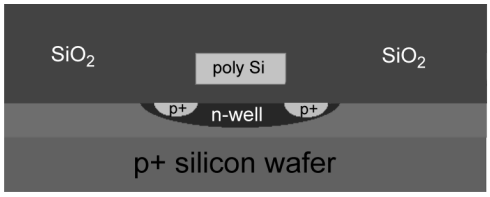

Step 7: A layer of silicon oxide is grown to insulate the transistors from subsequent layers. In current device generations this oxide is more and more replaced by organic dielectrics with low dielectric constants to reduce the overall capacitance of the device and hence allow higher switching speeds.

Figure 6.6 continued

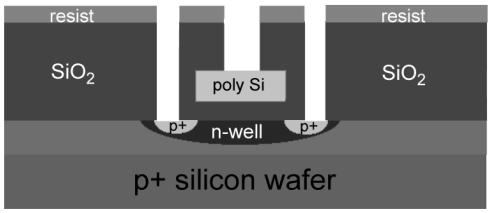

Step 8: In a further photolithographic process followed by an etch the contact holes, which will allow electrical connection to the source and drain areas as well as the gates are formed.

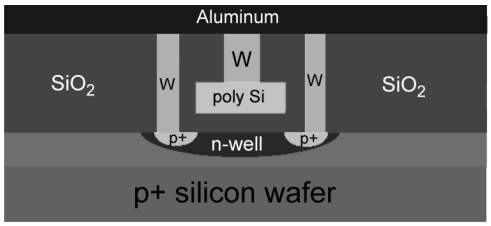

Step 9: The holes are filled with tungsten and an aluminum layer, called the metal 1 layer, is deposited.

Figure 6.6 continued

In many subsequent steps the metal 1 is patterned to form the first layer of the circuitry and many more patterned insulating layers metal layers connected by tungsten vias are produced. The final device is protected with a silicon nitride passivation layer with only the bonding pads exposed. Processes for state of the art devices are much more complicated and involve a wide range of other materials such as titanium silicide and silicon nitride. The aluminum in the metal layers is more and more replaced by copper. Also, the implantation process is more complicated to generate appropriate depth profiles of the source and drain regions.

6.4 Assessing the Sample Quality

Before taking holograms on semiconductor samples for quantitative analysis, a series of quick checks should be performed to assess the quality of the sample.

Reference wave: Check if the feature of interest is close enough to the sample edge or to a hole in the sample to allow for a reference wave at the desired interference width and magnification.

Thickness: Check if the sample has the optimum thickness discussed in section 5.1.1. For a 200 keV instrument the sample thickness should be around 200 nm. To quickly check the sample thickness increase the magnification and record a hologram of the sample edge. The reconstructed phase image should have a phase difference between the vacuum and the feature of interest of about 17.4 rad. This means two 2π phase jumps should be visible with a third one almost reached.

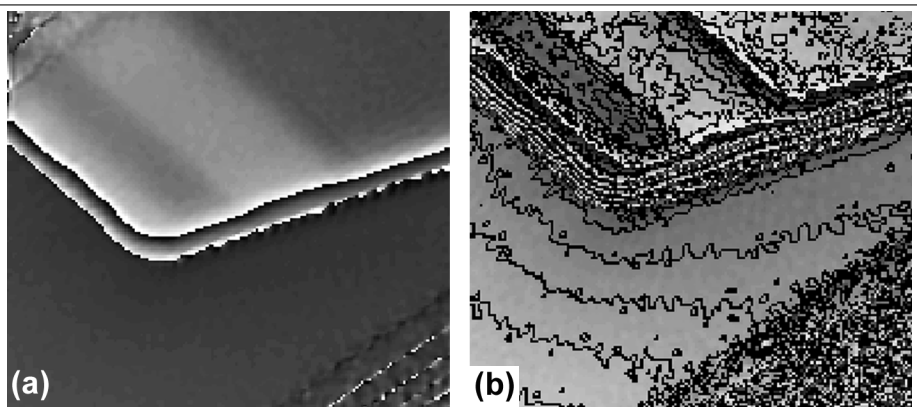

Figure 6.7: Sample charging: (a) Phase image of a silicon sample. Areas containing boron implants appear bright. No problems with sample charging are apparent. (b) Same phase image after 4 times phase magnification by taking the complex image to the power of four and displaying the phase. Charging around the sample edge is now clearly visible as outlined by the 0.2π spaced equipotential lines.

Charging: Uncontrolled charging of the sample should be avoided as much as possible as it will add an unknown contribution to the measured phase shift and makes a quantitative interpretation impossible. As shown by Frost and Voelkl even changes in the objective lens excitation or the choice of the condenser aperture can alter the sample charging and will lead to irreproducible results. [32] Sample charging is best detected by carefully inspecting if the phase in the vacuum part of the hologram is completely flat. Figure 6.7 shows an example where this is not the case and quantitative interpretation of the dopant profiles could be difficult. To detect small phase changes in the vacuum region due to charging it can be helpful to phase magnify the image. This is done by taking the complex image to a power of n and displaying the phase of the result. The resulting phase image is then n times phase magnified. If charging is due to silicon oxide or nitride layers, these layers should be removed by methods described in section 5.2.1. The most common cause of charging, however, is dirt on the sample, which can be removed by further precision ion polishing or in a plasma cleaner. One should note that unwanted potential distributions due to charging as they appear in the vacuum are reduced inside the sample because of the high dielectric constant of silicon of $\epsilon = 11.8$.

Amorphous surface layers: Thick amorphous surface layers can be detected by their characteristic diffraction ring pattern. It is also beneficial to compare the thickness obtained from CBED with the one obtained from the phase image as explained in 6.2.3. Extensive diffraction analysis should be done *after* taking holograms of the

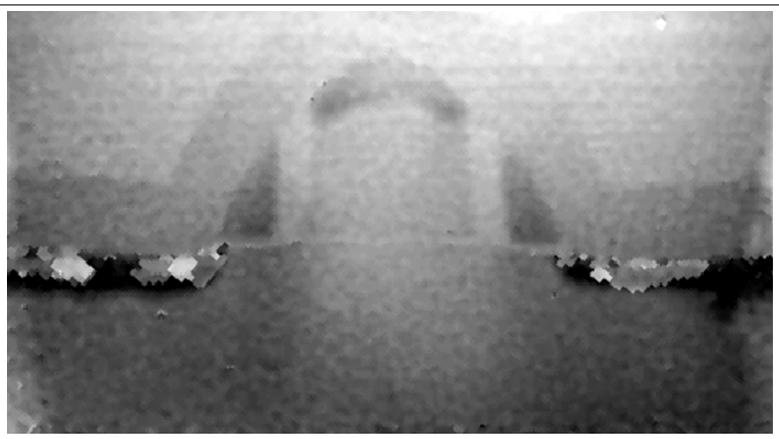

Figure 6.8: Phase image of a transistor. Is the brighter region below the gate due to doping or due to thickness variations, or both?

sample as converging the beam onto the sample will cause contamination, which can lead to charging problems.

Differential milling artifacts: As mentioned in the section on FIB sample preparation 5.2.4 different milling speeds of different materials can cause changes in sample thickness in specimens prepared with both a FIB system or a PIPS. A typical example of such curtaining or waterfall effects was shown in figure 5.6. Problems of this kind can be best detected by observing the sample in an SEM at a low beam energy. The resulting local increase in thickness, which results from shadowing of the ion beam by the transistor gate, can be easily confused with doping contrast (see figure 6.8).

6.5 Activation of Dopants in Silicon

During the implantation process boron, phosphorus, and arsenic dopants are implanted by shooting them into the silicon wafer as a high energy ion beam. The beam energy depends on the desired depth profile. After the implantation process the dopant atoms are however not bound to the silicon lattice yet and do not share electrons or holes with the surrounding silicon atoms, i.e. they are electrically inactive. To activate the dopants the silicon wafer needs to be briefly annealed at a temperature above about 650°C. To investigate this process a wafer was removed from the fabrication line right before the activation described in step 6 in section 6.3. The wafer had been implanted with a high dose boron ion beam ($5{\cdot}10^{16}$ ions/cm^2). A TEM sample was prepared with the dimpling and precision ion polishing method described in section 5.2.3. Great care was taken to cross-section the transistors exactly at the implanted areas. Holograms were then taken

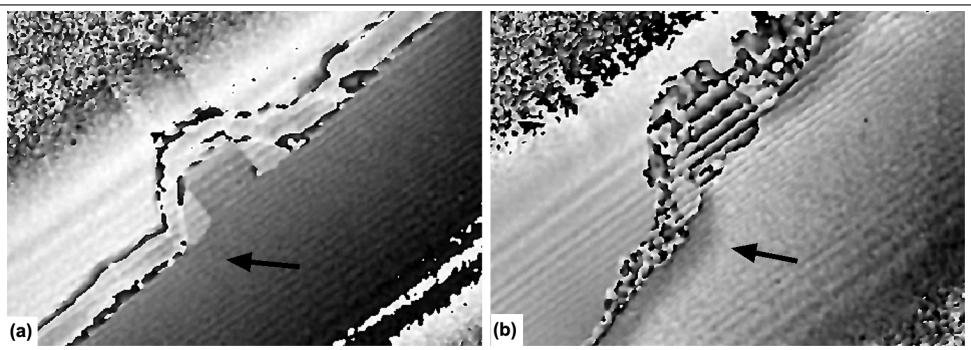

Figure 6.9: Activation of boron doped silicon: (a) Reconstructed phase image of an as-implanted wafer before the activation. No dopant contrast is visible in the source-drain region. (b) After heating the sample to 700°C for three minutes voltage contrast due to dopants becomes clearly visible.

on the as-implanted specimens and no voltage contrast due to active dopants could be detected in the reconstructed phase images. The samples were then transfered to a reaction chamber with pumping, gas purging, and heating capabilities. The chamber was evacuated three times to 15 Torr and backfilled to atmospheric pressure with argon to reduce the oxygen and water vapor content. After this the samples were heated to 700°C in the argon atmosphere, kept at this temperature for three minutes, and cooled down to room temperature. As the epoxy, which was used to glue the samples to a carbon grid, did not withstand the high temperatures used, the silicon pieces needed to be re-glued onto the carbon grid. After this procedure another set of holograms was taken that clearly showed dopant contrast in the source-drain areas as illustrated in figure 6.9. The experiment was reproducible. No activation could be observed with annealing temperatures below 650°C.

6.6 A Real World Example

In this section we will show how off-axis electron holography can be applied to examine dopant distributions in a real world semiconductor device. While there have been a few publications demonstrating the applicability of the method to voltage profiling on large lab-made transistors, blanket implants, and bulk pn-junctions [70, 72, 90], the large number of difficulties associated with sample preparation and specifics of the electron optical setup have barred the method from being applied to state-of-the art semiconductor devices as they can be found in commercial microprocessors. The advances presented in this thesis have now made the successful application of electron holography to voltage profiling of such a device possible: In chapter 5 new methods for sample preparation have been presented, which allow the preparation of samples suitable for holography

with optimum thickness, low surface amorphization, and a hole for the reference wave close to the area of interest. With the use of the FIB methods, which were also discussed in chapter 5, highly site-specific sample preparation of sub-micron device structures is now possible. We also explained how the layer of the microprocessor containing the actual transistors, which is usually covered by many layers of complicated circuitry, can be exposed to the surface by various delayering methods. In chapter 4 we presented a special microscope alignment for a conventional field emission microscope, which allows the holographic imaging of sub-micron devices. In chapter 2 the theoretical background necessary for optimum image recording, reconstruction, filtering, and interpretation was outlined as well as novel approaches to electron biprism technology, which resulted in an improved electron biprism. Finally in the present chapter specifics concerning dopant profiling on CMOS devices were discussed while giving special attention to the problem of thickness correction of phase images. By applying all these findings a voltage profile of the doped areas of a transistor taken from a commercial off-the-shelf Intel Pentium III^{TM} processor was be obtained, as we will present in the following paragraphs. The results have been published in Ultramicroscopy. [110]

An off-the-shelf Intel Pentium III processor was purchased in a computer store. The die was carefully removed from the packaging using a Dremel tool and cleaned in boiling sulfuric acid. The passivation layer and several metal layers were removed by parallel lapping and chemical etching as described in section 5.2.1. The sample was then tripod polished to about 3.5 μm thickness and glued to a copper grid, that had been cut in half. In an FEI Stata 235 dual beam focussed ion beam milling (FIB) system, additional layers were removed with the beam at 30 kV until metal 1, the metal layer above the transistor, was reached. A protective layer of platinum was then deposited inside the dual beam system and electron-transparent membranes of different thicknesses ranging from 100 nm to 300 nm were cut at several positions of the sample where transistors could be found. The membranes were thinned according to both methods described in section 5.2.4.2. The sample was imaged in the medium magnification mode as described in section 4.3. Images were taken with a sampling rate of 3.7 pixels per fringe, 6% fringe contrast and a total interference width of 242 nm. Reference holograms were acquired with each experimental hologram. The holograms were reconstructed using the Holoworks package written by Edgar Völkl for Digital Micrograph^{TM}. To remove 2π phase jumps, the phase image was unwrapped using algorithms developed by Frank Kahl [51]. The membrane, and within the membrane a transistor, with the best properties according to the criteria discussed in the previous section was selected. The thickness of the sample at the gate oxide was determined to be 246 ± 12 nm from the phase difference $\Delta\phi = 21.17$ rad measured relative to the vacuum area. The phase shifts due to source and drain implants are masked by the phase shift resulting from an overall thickness change of the sample (figure 6.10. Since the thickness increase over the region of interest was found to be linear it could be easily subtracted from the image, making the doped areas clearly visible (figure 6.11). Due primarily to the low fringe contrast, the noise level in the phase image was so high that a direct quantitative analysis of the line scans

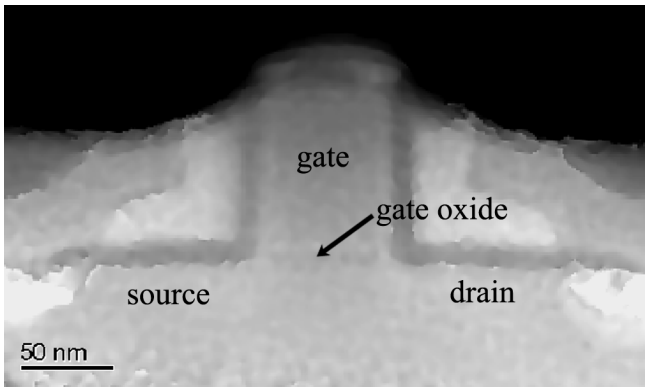

Figure 6.10: Unwrapped phase image of single transistor. Source and drain implants are barely visible due to the large overall contrast change.

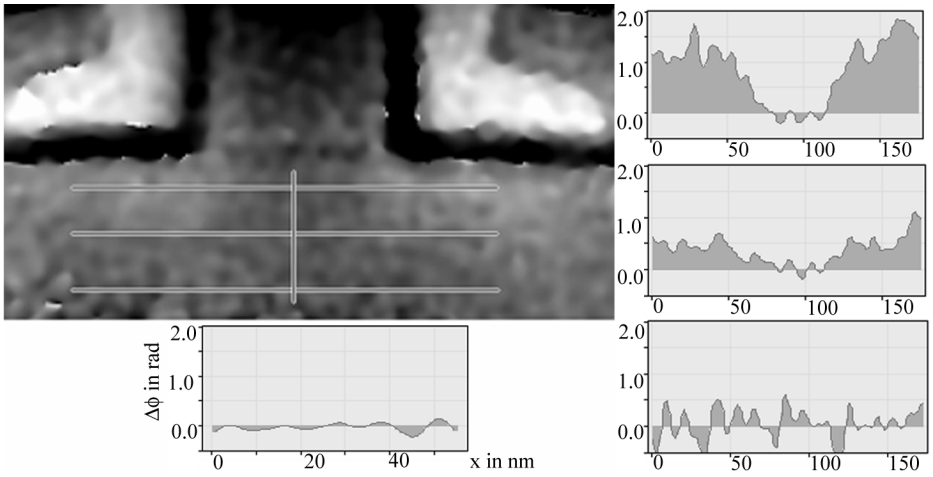

Figure 6.11: After subtracting overall linear thickness changes from the region of interest phase changes due to doping become visible as bright areas. Linescans at different positions show details of the source-drain implants. The line profiles on the right-hand side correspond in consecutive order to the horizontal lines in the phase image. Y-axes show the phase in rad.

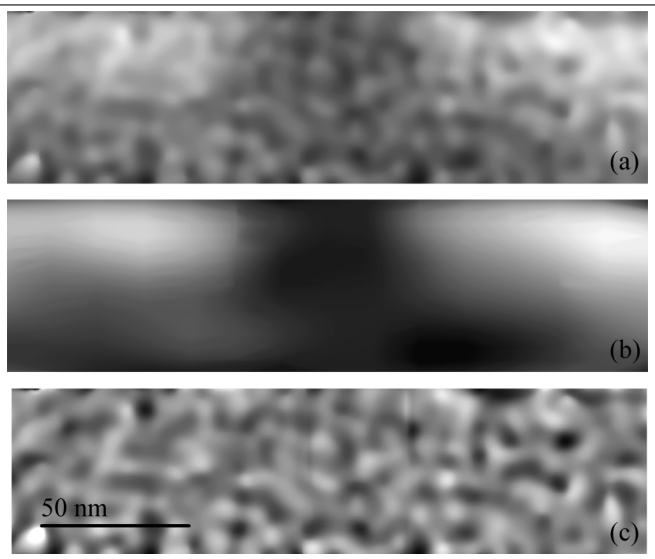

Figure 6.12: Close up of the source-drain region: Raw phase image (a), analytical fit of the data (b), difference between raw-data and fit (c). Bright regions show the source-drain implants.

was not feasible. Because conventional methods of smoothing often introduce spurious periodicities and artifacts, we analytically fitted the data based on physical assumptions about the overall shape of the profile. First, the overall shape perpendicular to the gate can be described by a Gaussian function falling off into the essentially flat substrate area below the transistor, as can be expected from the physics of the ion-implantation process. Second, the gate region is essentially flat since source and drain implants do not reach inside it. This is represented in the fit by an overall multiplication with a linear combination of two arctangent functions, one with a positive argument and the other with a negative one. Additional features of the shape are described by using first, second and third order Fourier components, as well as a linear combination of polynomials of the form $x^n y^m$ with $0 \leq n + m \leq 5$. The fit was optimized to minimize the variance of the difference between fit and raw data over the whole analyzed area. A variance of 0.49 rad^2 about an average of zero, which is half the variance of the raw data in the flat region, was achieved (figure 6.12). Knowing the voltage profile as an analytic function enables us to easily calculate the carrier concentration given by $n = \epsilon_0 \epsilon / e \, \nabla^2 U(x, y)$. Here ϵ_0 denotes the permittivity of free space, e is the electron charge, and ∇^2 is the Laplacian. The dielectric constant ϵ has a value of 11.8 in silicon [9], and the voltage $U(x, y)$ is calculated from the fitted phase profile using $\Delta U(x, y) = \Delta\phi/(C_E t)$. Figure 6.13 shows the voltage profile and carrier density profile over the source drain region. The voltage peaks at 0.88 V with respect to the undoped areas. The maximum carrier density can be computed to be $1.25 \cdot 10^{19}$ carriers per cm^3.

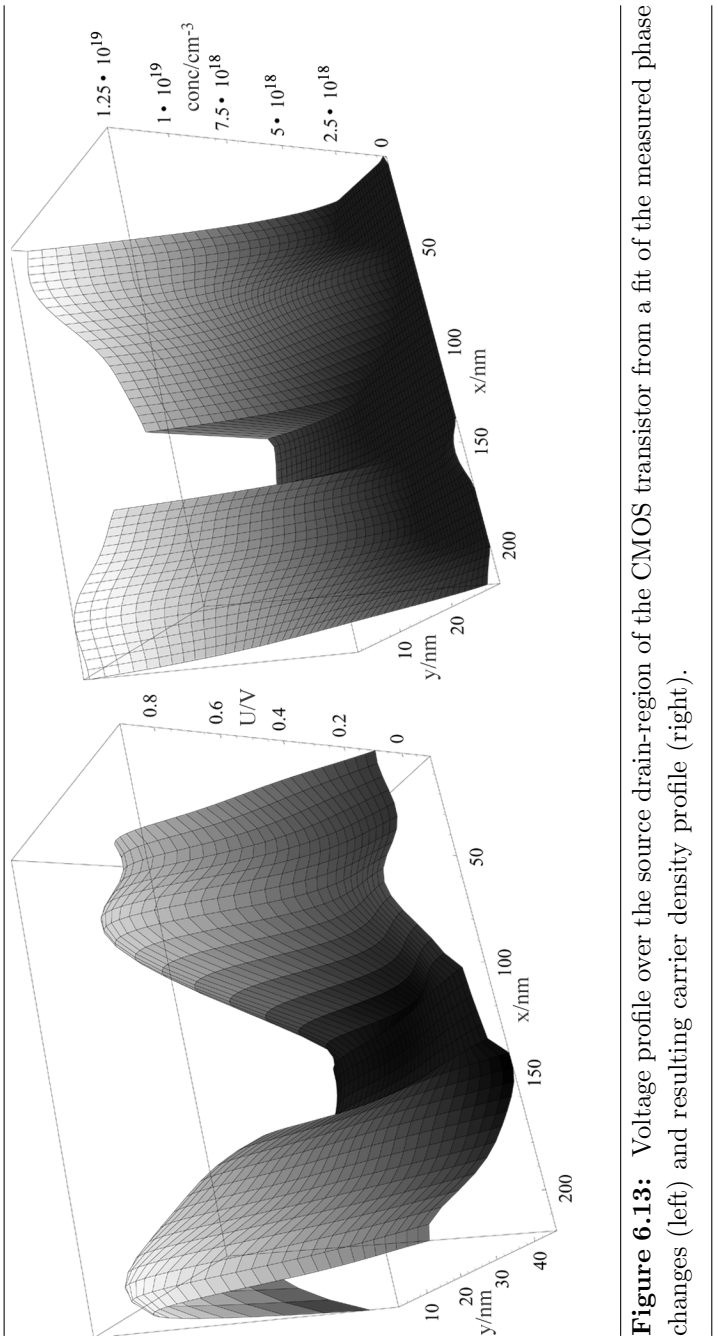

Figure 6.13: Voltage profile over the source drain-region of the CMOS transistor from a fit of the measured phase changes (left) and resulting carrier density profile (right).

This demonstration of voltage profiling on 75 nm gate-architecture commercial CMOS devices shows that off-axis electron holography has now emerged as a viable solution to this long standing problem. It can now be routinely applied to answering questions about the extent and depth of the source-drain implants and the channel length below the gate. While until now computer simulations of semiconductor devices, which are commonly used to guide the process development in the semiconductor industry, had to rely exclusively on one-dimensional SIMS data, computer models of ultra-shallow junctions can now be verified and improved by using two-dimensional voltage profiles obtained by electron holography. An additional benefit is the fact that in contrast to SIMS, which measures the total concentration of the implanted species, electron holography is only sensitive to the electrically active implants as demonstrated in section 6.5. Thus, electron holography will also be a valuable tool to improve existing models of dopant activation. As transmission electron microscopes offer point resolutions well below one nanometer, TEM off-axis holography is ideally suited to meet the dopant profiling needs under the rapidly decreasing design rules of future semiconductor device generations.

6.7 Alternative Electron Microscopical Methods for Two-Dimensional Dopant Profiling

Apart from electron holography other electron microscopical methods have been recently discussed to create two-dimensional profiles of doped semiconductor devices. A group at the Hitachi Central Research Laboratory has succeeded in creating an arsenic map of a CMOS transistor by energy dispersive x-ray spectroscopy (EDX) in a scanning transmission electron microscope (STEM). [112] Since the x-ray signal of the arsenic k-edge is extremly weak for the low dopant concentrations of less than 1 atomic %, the images were acquired over a time of eight hours to get some arsenic x-ray signal above background. This unusually long exposure time could only be achieved by using a sophisticated drift correction system. In contrast to electron holography, which measures only the voltage changes due to electrically active dopant atoms, all arsenic atoms in the sample, whether activated or not, will contribute to the x-ray count. Because of the long exposure times and the poor signal to noise ratio the usefulness of this method for day-to-day device analysis needs in the semiconductor industry remains questionable.

Over the last decade several attempts have been made to image junctions in silicon-based devices using secondary electron contrast in the scanning electron microscope (SEM). [14, 15, 86, 96, 113, 114] In all these studies n-doped regions appear darker than p-doped ones and the intensity is logarithmically proportional to the active dopant concentration. However the contrast mechanism, which is generally related to surface band structure and electron ionization energy, has not been fully understood yet. The current state of understanding has been summarized by Sealy et al. [96]. An additional problem is that the contrast depends strongly on a multitude of parameters including

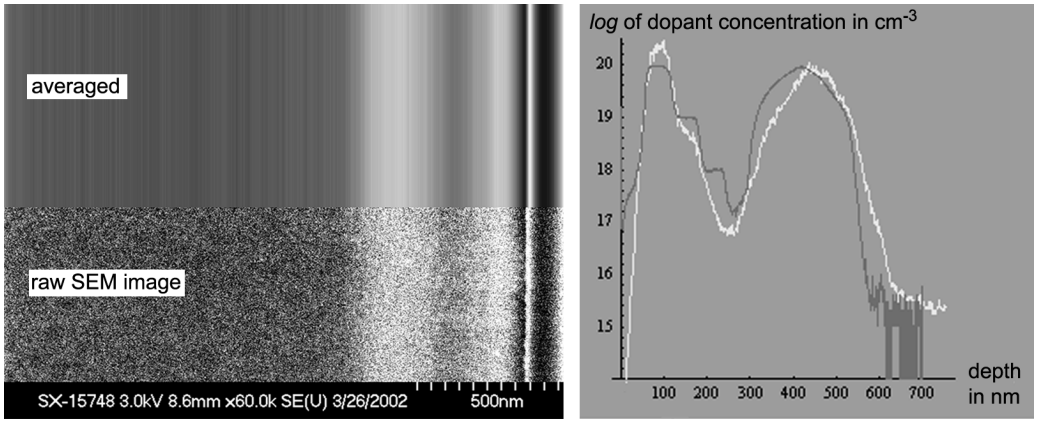

Figure 6.14: Secondary electron doping contrast in the SEM. Left side: SEM micrograph of a silicon wafer with blanket boron implants obtained by the upper SE detector on a S4700 FE-SEM at 3 kV beam voltage. The image shows raw data and vertically averaged data. Right side: Comparison between the secondary electron dopant contrast and the boron concentration obtained by SIMS. The secondary electron dopant contrast has been scaled by an arbitrary constant to match the SIMS profile.

scan speed, beam voltage, beam current, and details of the detection system. It is very sensitive to the surface condition of the sample and prior surface treatment. Figure 6.14 shows an SEM micrograph obtained from a sample, which was prepared from a boron doped silicon wafer. On the right part of the figure the dopant contrast from the micrograph is compared with the logarithm of the dopant concentration, which has been obtained by SIMS profiling. The contrast is here defined according to [114] by

$$C = \frac{1}{2}\frac{(I_{\text{doped}} - I_{\text{ref}}) - (I_{\text{sub}} - I_{\text{ref}})}{(I_{\text{doped}} - I_{\text{ref}}) + (I_{\text{sub}} - I_{\text{ref}})}, \tag{6.15}$$

where I_{doped} denotes the pixel intensity in the doped area, I_{sub} the intensity in the undoped substrate, and I_{ref} is the zero level with the beam blanked. The graph of the contrast in the figure has been scaled by an arbitrary constant to match the SIMS profile. To my knowledge results from this method have only been obtained on test structures like the one shown here and no reliable data taken from real devices has been presented so far. At present an accurate theory is missing, which allows quantitative interpretation of the contrast seen in the micrographs. The development of energy filtered secondary electron detectors for field emission SEMs would also greatly advance this field.

Apart from these methods selective etching of doped areas and spreading resistance profiling have been discussed as possible approaches for dopant profiling. Their practicability and their limitations have been summarized by Diebold et al. [21].

Not all the desirable is obtainable, and not all worth to be discerned is discernible.

Johann Wolfgang Goethe

7 Summary and Outlook

The use of coherent electron beams has opened a unique new way of electron microscopy. It is now possible to determine phase changes of the electron wave with high accuracy. In a reflection geometry this can be utilized to inspect high aspect ratio sub-micron sized structures on surfaces while eliminating depth of field problems found in conventional scanning microscopes and allowing rapid parallel image acquisition. In transmission electron microscopes off-axis electron holography now enables us to obtain quantitative information about potentials and magnetic flux, as well as thickness and compositional information on a sub micron level.

After building a point projection microscope and reaching its anticipated performance in transmission mode as well as successfully obtaining first images in reflection mode with an additional extraction anode, the future road map for the point projection microscope is clear: The new electron gun needs to be assembled, integrated into the system, tested and optimized. An extension of the microscope chamber or the integration of a projection lens might be necessary to gain extra magnification and to fully utilize the existing micro-channel plate.

In the transmission electron microscope we have demonstrated how off-axis electron holography has evolved into a viable tool to map out the small potential changes associated with active dopants in state of the art semiconductor devices. Using the free lens control of the HF-2000 cold field emission TEM a holography setup was obtained, in which current semiconductor devices could be analyzed. Advances were made in TEM sample preparation for electron holography in the areas of both focussed ion beam (FIB) and mechanical sample preparation. The observed voltage contrast was clearly linked to the active dopants in silicon by activation experiments.

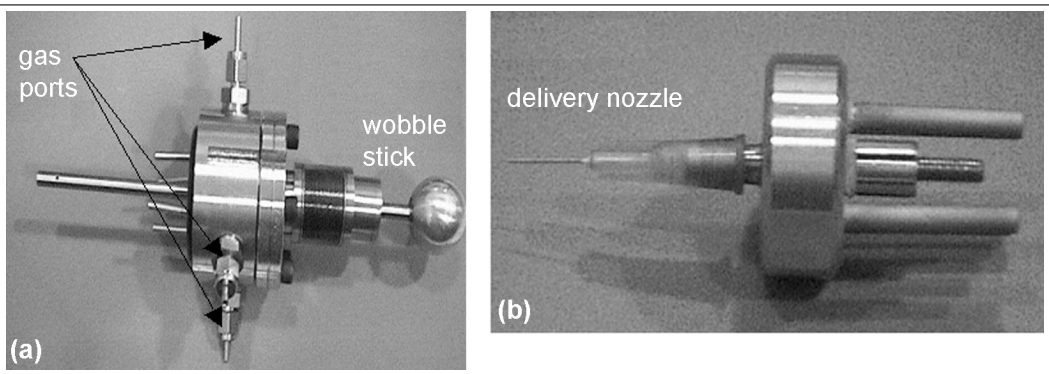

Figure 7.1: Gas injector for e-beam etching in reactive gas atmospheres: (a) Four gas feed throughs allow to leak gases through a small nozzle (b) into the SEM chamber. The nozzle can be positioned in close proximity to the sample by using a wobble stick.

7.1 Room for Improvement

As always, there is still room for improvement in several areas: As semiconductor devices continue to decrease in size, mechanical site-specific precision sample preparation will become more challenging and more and more FIB sample preparation will be required. As high energy ions cause amorphization of the sample surfaces and focussed ion beam systems perform purely at low beam energies, new ways of site specific sample preparation for electron holography have to be investigated. We have already started such efforts in our group using electron beams in connection with reactive gases to generate radicals, which allow site and material specific etching of samples. To this end a gas delivery system for our scanning electron microscope has been constructed, which allows the controlled positioning of a gas jet onto the sample, while imaging it with the electron beam (figure 7.1). First results have been obtained using xenon difluoride and sulfur hexafluoride as gases. In order to remove carbon buildup during the etch process a small amount of water vapor can be included in the gas mixture. A wide variety of materials has been etched including silicon, silicon dioxide, silicon nitride, tantalum, carbon, tantalum nitride, photo-resist material, SILK^{TM}, chrome and copper. Figure 7.2 shows for example a small hole etched into silicon dioxide. The main problem so far is that the ionization cross-section of the gases used peaks at a few hundred electron volts. Because of this a low electron beam energy in this order of magnitude is desired. However, at only a few hundred electron volts beam energy scattering of the primary beam electrons in the gas atmosphere will limit the resolution. If the beam voltage is increased scattering of the primary beam is reduced but the ionization of the gas will now occur primarily by the secondary electrons, which are emitted from the sample, and not by the electrons in the primary beam. The increase in the volume, from which

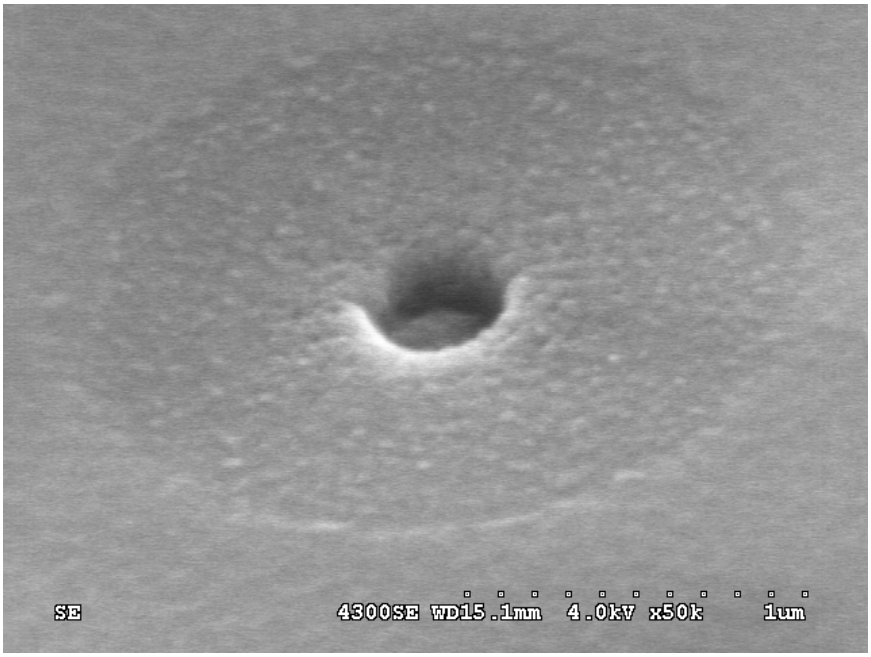

Figure 7.2: Hole with a 300 nm diameter etched in silicon dioxide with the electron beam in a xenon difluoride atmosphere. (Image courtesy of Jason Fowlkes.)

secondary electrons are emitted, with beam energy limits the resolution at high beam energies. Studies are now on the way to optimize a variety of parameters such as gas pressure and composition, beam energy, beam current, scan speed and sample temperature for speed and resolution.

As part of a continued effort to prepare better samples for electron holography the benefits of coating samples with a thin metal layer to reduce charging artifacts need to be further investigated.

Finally, there is room for improvement on the instrumentation side as only little effort has been done to optimize electron microscopes for holography. The addition of a Lorentz lens in some FEI microscopes is a good first step to obtain a more convenient way to change magnification and helps to obtain an excellent field of view in the medium magnification range. Some improvement of the fringe contrast should be possible by better screening of the electron gun and column and re-routing of cables in and around the microscope with minimum cross talk with the beam in mind. New approaches to generating more coherent and brighter electron beams need to be investigated. Recently experiments have shown that field emission from niobium tips in the superconducting state produce electron beams of unsurpassed monochomaticity.[81] This behaviour reflects the small energy gap of superconductors at the Fermi level and the high density of states at the lower edge. Some authors have suggested that because the quantum me-

chanical ground state of a superconductor extends over a macroscopic area, emission of mutually coherent electrons from different areas on the superconductor surfaces may be possible.[83, 122] Promising experiments with EuS coated tungsten tips have been conducted at the University of Tübingen, which exhibit a high degree of spin polarization and a narrow energy width of the emitted electrons.[46]

7.2 Limitations

Off-axis electron holography is ideally suited to image the rapidly decreasing semiconductor devices and allows even for the correction of lens aberrations to increase the image resolution beyond the point resolution of the microscope used. The field of view available in the hologram, however, will decrease with increasing magnification and the hole for the reference wave needs to be closer and closer to the feature of interest. As mentioned in the previous section the preparation of such samples even with focussed ion beam systems will be very challenging. A second problem arises from the fact that transistors are not only shrinking in width but also in thickness. While current transistors are about 250 nm thick future generations will have thicknesses well below 200 nm. Because of this, thinner samples will be required. As the optimum sample thickness for dopant profiling depends on the beam energy, it might become necessary to record holograms at beam energies of 150 kV or lower. In new device manufacturing processes a silicon oxide layer is formed directly below the implanted areas. Charging of this layer in the electron beam might make the interpretation of the voltage profiles increasingly difficult and more research about sample coating to reduce these charging effects is necessary. Recently processes are being discussed in which the silicon layer below the gate is severely strained in order to increase carrier mobility. As strained crystals produce diffraction artifacts in the TEM this might impede the interpretation of the recorded phase images even more.
Nevertheless, off-axis electron holography will continue to prosper as a unique method to obtain quantifiable phase and amplitude information of the transmitted electron wave in the TEM. Its application is not limited only to dopant profiling but to a wide field of problems, in which electric potentials and magnetic flux need to be imaged and quantified on a sub micron scale.

References

[1] International Technology Road Map for Semiconductors. `http://public.itrs.net`, Email: technology.roadmap@sematech.org. 80

[2] Y. Aharonov and D. Bohm. Significance of electromagnetic potentials in the quantum theory. *Phys. Rev.*, 115:485–491, 1959. 27

[3] S.M. Allen. Foil thickness measurements from convergent-beam diffraction patterns. *Philos. Mag. A*, 43:325, 1981. 86

[4] N.W. Ashcroft and N.D. Mermin. *Solid State Physics*. Sounders College Publishing, Orlando, 1976. 81

[5] J. Bardon, A. Degiovanni, V. Georges, and R. Morin. Conducting, semiconducting and insulating objects observed by low-energy electron holography. *Ultramicroscopy*, 92:133–142, 2002. 43

[6] J. Bardon, V. Georges, A. Degiovanni, and R. Morin. Improved low energy electron projection in-line hologram reconstruction: application to the holograms of a tungsten tip. *Micron*, 33:493–497, 2002. 47

[7] Á. Barna, B. Pécz, and M. Menyhard. TEM sample preparation by ion milling/amorphization. *Micron*, 30:267–276, 1999. 70

[8] W. Bayh. Messung der kontinuierlichen Phasenschiebung von Elektronenwellen im kraftfeldfreien Raum durch das magnetische Vektorpotential einer Wolfram-Wendel. *Zeitschrift für Physik*, 169:492–510, 1962. 2, 27

[9] W.E. Beadle, J. Tsai, and R. Plummer, editors. *Quick Reference manual for Silicon Integrated Circut Technology*. John Wiley and Sons, New York, 1985. 97

[10] C. Beeli, B. Doudin, J.-Ph. Ansermet, and P. Stadelmann. Off-axis electron holography of single ferromagnetic nanowires. *Materials Characterization*, 42:175–182, 1999. 3

[11] M. Born and E. Wolf. *Principles of Optics*. Pergamon, 5th edition, 1975. 11

[12] R. Buhl. *Zeitschrift für Physik*, 155:395–412, 1959. 2

[13] R. Burge, J. Dainty, and J. Thom. The spatial coherence of electron beams. In *Proceedings EMAG 1975, Bristol, J.Venables (editor)*, page 221, London, 1975. Academic Press. 11

[14] M.R. Castell, D.D. Perovic, and H. Lafontaine. Electronic contribution to secondary electron compositional contrast in the scanning electron microscope. *Ultramicroscopy*, 69:279–287, 1997. 99

[15] M.R. Castell, T.W. Simpson, I.V. Mitchell, D.D. Perovic, and J.-M. Baribeau. Deactivation and diffusion of boron in ion-implanted silicon studied by secondary electron imaging. *Appl. Phys. Lett.*, 74:2304–2306, 1999. 99

[16] J.M. Cowley. Chromatic coherence and inelastic scattering in electron holography. *Ultramicroscopy*, 57:327–331, 1995. 12, 16

[17] L. Cser, G. Török, G. Krexner, I. Sharkov, and B. Faragó. Holographic imaging of atoms using thermal neutrons. *Phys. Rev. Lett.*, 89:175504–1, 2002. 2

[18] N. de Jonge, Y. Lamy, K. Schoots, and T.H. Oosterkamp. High brightness electron beam from a multi-walled carbon nanotube. *Nature*, 420:393–395, 2002. 48

[19] D.J. de Ruijter and J.K. Weiss. Detection limits in quantitative off-axis electron holography. *Ultramicroscopy*, 50:26, 1993. 34, 68

[20] D. Delille, R. Pantel, and E. Van Capellen. Crystal thickness and extinction distance determination using energy filtered CBED pattern intensity measurement and dynamical diffraction theory fitting. *Ultramicroscopy*, 87:5–18, 2001. 86, 88

[21] A.C. Diebold, M.R. Kump, J.J. Kopanski, and D.G. Seiler. Characterization of two-dimensional dopant profiling: Status and review. *J. of Vac. Sci. Technol. B*, 14(1):196–201, 1996. 100

[22] Z.J. Ding and R. Shimizu. Inelastic collisions of kV electrons in solids. *Surface Science*, 222:313–331, 1989. 53, 54

[23] D. Van Dyck, H. Lichte, and J.C.H. Spence. Inelastic scattering and holography. *Ultramicroscopy*, 81:187–194, 2000. 12, 15

[24] R.F. Egerton. *Electron Energy-Loss Spectroscopy*. Plenum, New York, 1986. 84, 88

[25] R.H. Fowler and L. Nordheim. Electron emission in intense electric fields. In *Proc. Roy. Soc. London*, volume A119, page 173, 1928. 18

[26] S. Frabboni, G. Matteucci, G. Pozzi, and M. Vanzi. Electron holographic observations of the electrostatic field associated with thin reverse biased p-n junctions. *Phys. Rev. Lett.*, 55:2196–2201, 1985. 3

[27] B.G. Frost. An electron holographic study of electric charging and electric charge distributions. *Ultramicroscopy*, 75:105–113, 1998. 3

[28] B.G. Frost. Image-plane off-axis electron holography: low-magnification arrangements. *Meas. Sci. Technol.*, 10:333–339, 1999. 22, 35

[29] B.G. Frost, D.C. Joy, and A.E. Thesen. A low voltage point source microscope for interferometry. In D. Herr, editor, *Proceedings: Conference on Metrology, Inspection and Process Control for Microlithography XVI, Santa Clara, CA*, volume 4689. SPIE, 2002. 41

[30] B.G. Frost and G. Matteucci. Low magnification electron holograms. In E. Völkl, L.F. Allard, and D.C. Joy, editors, *Introduction to Electron Holography*, page 183. Kluwer Academic / Plenum Publishers, New York, 1999. 38

[31] B.G. Frost, N.F. van Hulst, E. Lunedei, G. Matteucci, and E. Rikkers. Study of the leakage field of magnetic force microscopy thin-film tips using electron holography. *Appl. Phys. Lett.*, 68:1865, 1996. 3

[32] B.G. Frost and E. Voelkl. A study of electric charging using low-magnification electron holography. *Materials Characterization*, 42:221–227, 1999. 3, 92

[33] B.G. Frost, E. Voelkl, and L.F. Allard. An improved mode of operation of a transmission electron microscope for wide field off-axis holography. *Ultramicroscopy*, 63:15–20, 1996. 63, 64, 65

[34] Q. Fu, H. Lichte, and E. Völkl. Correction of aberrations of an electron microscope by means of electron holography. *Phys. Rev. Lett.*, 67:2319–2322, 1991. 3

[35] D. Gabor. A new microscopic priciple. *Nature*, 161:777–778, 1948. 1, 3, 42

[36] D. Gabor. *Rev. Mod. Phys.*, 28:260, 1956. 16

[37] M. Gajdardziska-Josifovska and A. Carim. Applications of electron holography. In E. Völkl, L.F. Allard, and D.C. Joy, editors, *Introduction to Electron Holography*, page 267. Kluwer Academic / Plenum Publishers, New York, 1999. 29

[38] M. Gajdardziska-Josifovska and M.R. McCartney. Elimination of thickness dependence from medium resolution electron holograms. *Ultramicroscopy*, 53:291–296, 1994. 84

[39] M. Gajdardziska-Josifovska, M.R. McCartney, W.J. de Ruiter, D.J. Smith, J.K. Weiss, and J.M. Zuo. Accurate measurements of mean inner potential of crystal wedges using digital electron holograms. *Ultramicroscopy*, 50:285, 1993. 3

[40] V. Georges, J. Bardon, A. Degiovanni, and R. Morin. Imaging charged objects using low-energy-electron coherent beams. *Ultramicroscopy*, 90:33–38, 2001. 43

[41] A. Gölzhäuser. Nanolithography and electron holography with ultrasharp field emitters. *Applied Surface Science*, 141:264–273, 1999. 48

[42] A. Gölzhäuser, B. Völkel, M. Grunze, and H.J. Kreuzer. Optimization of the low energy electron point source microscope: imaging of macromolecules. *Micron*, 33:241–255, 2002. 4, 42

[43] A. Gölzhäuser, B. Völkel, B. Jäger, M. Zharnikov, H.J. Kreuzer, and M. Grunze. Holographic imaging of macromolecules. *J. of Vac. Sci. Technol. A*, 16(5):3025–3028, 1998. 4, 42

[44] R. Gomer. *Field Emission and Field Ionization*. Harvard University Press, 1961. 19, 20

[45] P. Hariharan. *Optical Holography - Principles, techniques, and applications*. Cambridge University Press, Cambridge and New York, second edition, 1996. 2

[46] F. Hasselbach. Polarisierte Feldelektronenquellen. `http://info.physik.uni-tuebingen.de/hasselbach`. 104

[47] X.M.H. Huang, J.M. Zuo, and J.C.H. Spence. Wavefront reconstruction for in-line holograms formed by pure amplitude objects. *Applied Surface Science*, 148:229–234, 1999. 48

[48] D.C. Joy. Mott scattering cross-sections. `http://pciserver.bio.utk.edu/metrology`. 52

[49] D.C. Joy. *Monte Carlo Modeling for Electron Microscopy and Microanalysis*. Oxford University Press, New York and Oxford, 1995. 51

[50] D.C. Joy, Y.-S. Zhang, X. Zhang, T. Hashimoto, R.D. Bunn, L.F. Allard, and T.A. Nolan. Practical aspects of electron holography. *Ultramicroscopy*, 51:1–14, 1993. 22

[51] Frank Kahl. Private communication. Email: kahl@ceos-gmbh.de. 31, 32, 95

[52] N.L. Kato, N. Miura, and N. Tsutsui. A plasma-polymerized protective film for transmission electron microscopy specimen preparation by focused ion beam etching. *J. of Vac. Sci. Technol. A*, 16:1127, 1998. 75

[53] P.M. Kelly, A. Jostsons, R.G. Blake, and J.G. Napier. The determination of foil thickness by scanning transmission electron microscopy. *Phys. Stat. Sol. A*, 31:771, 1975. 86

[54] W. Kossel and G. Möllensted. *Ann. Phys.*, 5:113, 1939. 86

[55] H.-J. Kreutzer, K. Nakamura, A. Wierzbicki, H.-W. Fink, and H. Schmid. Theory of the point source microscope. *Ultramicroscopy*, 45:381–403, 1992. 46

[56] R.M. Langford and A.K. Petford-Long. Preparation of transmission electron microscope cross-section speciments using focussed ion beam milling. *J. of Vac. Sci. Technol. A*, 19:2186, 2001. 70, 76

[57] M. Lehmann and H. Lichte. Tutorial on off-axis electron holography. *Microscopy and Microanalysis*, 8:447–466, 2002. 3

[58] M. Lehmann, H. Lichte, D. Geiger, G. Lang, and E. Schweda. Electron holography at atomic dimensions-present state. *Materials Characterization*, 42:249–263, 1999. 3

[59] E.N. Leith and J. Upatnieks. Reconstructed wavefonts and communication theory. *Journal of the Optical Society of America*, 52:1123–1130, 1962. 1

[60] H. Lichte. Electron image plane off-axis holography of atomic structures. In T. Mulvey and C. J. R. Sheppard, editors, *Advances in Optical and Electron Microscopy*, volume 12, pages 25–91. Academic Press, London, 1991. 3, 17

[61] H. Lichte. Electron holography: optimum position of the biprism in the electron microscope. *Ultramicroscopy*, 64:79, 1996. 22, 68

[62] H. Lichte and B. Freitag. Inelastic electron holography. *Ultramicroscopy*, 81:177–186, 2000. 10, 12, 14, 15

[63] H. Lichte, D. Geiger, A.Z. Harscher, E. Heindl, M. Lehmann, D. Malamidis, A. Orchowski, and W.-D. Rau. Artefacts in electron holography. *Ultramicroscopy*, 64:67–77, 1996. 35, 37

[64] H. Lichte, K.-H. Herrmann, and F. Lenz. Electron noise in off-axis image plane holography. *Optik*, 77:125, 1987. 34, 68

[65] H. Lichte, M. Reibold, K. Brand, and M. Lehmann. Ferroelectric electron holography. *Ultramicroscopy*, 93:199–212, 2002. 3

[66] X. Lin and V.P. Dravid. Mapping the potential of graphite nanotubes with electron holography. *Appl. Phys. Lett.*, 69:1014–1016, 1996. 3

[67] C.-M. Chan M.A. Van Hove, W.H. Weinberg. *Low-Energy Electron Diffraction.* Springer, Berlin, 1986. 28

[68] C. Martin, E. Arakawa, T. Callcott, and R.J. Warmack. Attenuation lengths of low-energy electrons in free-standing carbon films. *Journal of Electron Spectroscopy and Related Phenomena*, 42:171, 1987. 43

[69] G. Matteucci, G. Missiroli, E. Nichelatti, A. Migliori, M. Vanzi, and G. Pozzi. Electron holography of long-range electric and magnetic fields. *Journal of Applied Physics*, 69:1835–1842, 1991. 3

[70] M.R. McCartney, F.A. Ponce, J. Cai, and D.P. Bour. Mapping electrostatic potential across an AlGaN/InGaN/AlGaN diode by electron holography. *Appl. Phys. Lett.*, 76:3055–3057, 2000. 3, 94

[71] M.R. McCartney, D.J. Smith, R.F.C. Farrow, and R.F. Marks. Off-axis electron holography of epitaxial FePt films. *Journal of Applied Physics*, 82:2461–2465, 1997. 3

[72] M.R. McCartney, D.J. Smith, R. Hull, J.C. Bean, E. Voelkl, and B. Frost. Direct observation of potential distribution across Si/Si p-n junctions using off-axis electron holography. *Appl. Phys. Lett.*, 65:2603–2605, 1994. 3, 94

[73] A. Mohan. *New Innovations for Contrast Enhancement in Electron Microscopy.* PhD thesis, University of Tennessee, 1997. 24

[74] G. Möllenstedt. The history of the electron biprism. In E. Völkl, L.F. Allard, and D.C. Joy, editors, *Introduction to Electron Holography*, page 3. Kluwer Academic / Plenum Publishers, New York, 1999. 2, 20

[75] G. Möllenstedt and H. Düker. *Naturwissenschaften*, 42:41, 1955. 2, 20

[76] G. Möllenstedt and H. Düker. *Zeitschrift für Physik*, 140:377–397, 1956. 17, 20

[77] G. Möllenstedt and H. Lichte. Doppler shift of electron waves. In *Proceedings of the Ninth International Congress on Electron Microscopy*, volume I, page 178, Toronto, 1987. 16

[78] R. Morin and A. Gargani. Ultra-low-energy-electron projection holograms. *Phys. Rev. B*, 48:6643, 1993. 43

[79] G.A. Morton and E.G. Ramberg. Point projector electron microscope. *Phys. Rev.*, 56:705, 1939. 3, 41

[80] Y. Murakami, D. Shindo, K. Oikawa, R. Kainuma, and K. Ishida. Magnetic domain structures in Co-Ni-Al shape memory alloys studied by Lorentz microscopy and electron holography. *Acta Materialia*, 50:2173–2184, 2002. 3

[81] K. Nagaoka, T. Yamashita, M. Yamada, H. Fujii, R. Seo, K. Matsuda, S. Uchiyama, and C. Oshima. Field emission energy spectra from superconduction and normal states of a niobium tip. *Ultramicroscopy*, 79:51–57, 1999. 103

[82] A. Orchowski. Päparation einer mono-atomaren Feldemissionskathode als Punktquelle für Elektronen und Ionen. Master's thesis, Institut für Angewandte Physik, Universität Tübingen, 1991. 18, 19, 20

[83] C. Oshima. Monochromatic field electron emission from a Nb superconductor. *Ultramicroscopy*, 78:27–32, 1999. 104

[84] E.D. Palik. *Handbook of Optical Constants.* Academic Press, San Diego, 1998. 53, 54

[85] J.B. Pendry. *Low Energy Electron Diffraction.* Academic Press, Boston, 1974. 28

[86] D.D. Perovic, M.R. Castell, A. Howie, C. Lavoie, T. Tiedje, and J.S.W. Cole. Field-emission SEM imaging of compositional and doping layer semiconductor superlattices. *Ultramicroscopy*, 58:104–113, 1995. 99

[87] P. Morin M. Pitaval and E. Vicario. Low energy off-axis holography in electron microscopy. *Phys. Rev. Lett.*, 76:3979–3982, 1996. 48

[88] G. Radi. *Acta Cryst. A*, 26:41, 1970. 29

[89] W.D. Rau and H. Lichte. High resolution off-axis electron holography. In E. Völkl, L.F. Allard, and D.C. Joy, editors, *Introduction to Electron Holography*, page 201. Kluwer Academic / Plenum Publishers, New York, 1999. 34

[90] W.D. Rau, P. Schwander, F.H. Baumann, W. Höppner, and A. Ourmazd. Two-dimensional mapping of the electrostatic potential in transistors by electron holography. *Phys. Rev. Lett.*, 82:2614, 1999. 3, 29, 70, 94

[91] L. Reimer. *Transmission Electron Microscopy*. Springer, Berlin, 1989. 28, 29

[92] F.M. Ross and W.M. Stobbs. Computer modelling for Fresnel contrast analysis. *Phil. Mag.*, 63:37, 1991. 29

[93] J.J. Sakurai. *Modern Quantum Mechanics*. Addison-Wesley Publishing Company, New York, 1995. 27

[94] D.K. Saldin, G.R.B. Harp, B.L. Chen, and B.P. Tonner. Theoretical principles of holographic crystallography. *Phys. Rev. B*, 44:2480–2492, 1991. 47

[95] H. Schmid. *Ein Elektronen-Interferometer mit 300 µm weit getrennten kohärenten Teilbündeln zur Erzeugung hoher Gangunterschiede und Messung der Phasenschiebung durch das magnetische Vektorpotential bei metalisch abgeschirmtem Magnetfluss*. PhD thesis, Universität Tübingen, 1985. 16

[96] C.P. Sealy, M.R. Castell, and P.R. Wilshaw. Mechanism for secondary electron dopant contrast. *Journal of Electron Microscopy*, 49(2):311–321, 2000. 99

[97] M.R.A. Shegelski and S. Faltus. Reconstruction of in-line holograms by lateral tomography. *Ultramicroscopy*, 77:135–140, 1999. 47

[98] M.R.A. Shegelski, S. Faltus, T. Clark, and H.J. Kreuzer. Improvement in the reconstruction of in-line holograms by energy sampling and tomography. *Ultramicroscopy*, 74:169–178, 1998. 47

[99] J.C.H. Spence. On the accurate measurement of structure-factor amplitudes and phases by electron diffraction. *Acta Cryst.*, A49:231–260, 1993. 28

[100] J.C.H. Spence. STEM and shadow-imaging of biomolecules at 6 eV beam energy. *Micron*, 28(2):101–116, 1997. 4, 42

[101] J.C.H. Spence and J.M. Cowly. Electron holography at low energy. In E. Völkl, L.F. Allard, and D.C. Joy, editors, *Introduction to Electron Holography*, page 311. Kluwer Academic / Plenum Publishers, New York, 1999. 50

[102] J.C.H. Spence, X. Zhang, and W. Qian. On the reconstruction of low voltage point projection holograms. In A. Tonomura, L.F. Allard, G. Pozzi, D.C. Joy, and Y.A. Ono, editors, *Electron Holography*, pages 267–276. Elsevier Science B.V., 1995. 43, 46, 47

[103] J.C.H. Spence and J. M. Zuo. *Electron Microdiffraction*. Plenum Press, New York, 1992. 29

[104] J.C.H. Spence and J. M. Zuo. Does electron holography energy-filter? *Ultramicroscopy*, 69:185–190, 1997. 12

[105] R. Subrahmanyan and M. Duane. In D.K. Schroder, J.L. Benton, and P. Rai-Choudhury, editors, *Proceedings of the Symposium on Diagnostic Techniques for Semiconductor Materials and Devices.*, volume 94-33, page 65. ECS, 1994. 80, 81

[106] L.W. Swanson and G.A. Schwind. A review of the Zr/O Schottky cathode. In J. Orloff, editor, *Charged Particle Optics*, chapter 2, pages 77–102. CRC Press, Boca Raton and New York, 1997. 18

[107] M. Tegze and G. Faigel. X-ray holography with atomic resolution. *Nature*, 380:49, 1996. 2

[108] A.E Thesen, B.G. Frost, and D.C. Joy. Low voltage nanotip interferomentry. In E. Voelkl et al., editor, *Proceedings: Conference on Microscopy and Microanalysis, Quebec, Canda*. Microscopy Society of America, 2002. 41

[109] A.E. Thesen, B.G. Frost, and D.C. Joy. Two-dimensional dopant profiling of ultrashallow junctions by electron holography. *J. of Vac. Sci. Technol. B*, 20, 2002. 3, 80

[110] A.E. Thesen, B.G. Frost, and D.C. Joy. Holographic voltage profiling of 75nm gate architecture CMOS devices. *Ultramicroscopy*, 94:277–281, 2003. 3, 95

[111] A. Tonomura, T. Matsuda, R. Suzuki, A. Fukuhara, N. Osakabe, H. Umezaki, J. Endo, K. Shinagawa, Y. Sugita, and H. Fujiwara. Observation of the Aharonov-Bohm effect by electron holography. *Phys. Rev. Lett.*, 48:1443, 1982. 2, 27

[112] R. Tsuneta, M. Koguchi, K. Nakamura, and A. Nishida. A specimen-drift-free EDX mapping system in STEM for observing two-dimensional profiles of low dose elements in fine semiconductor devices. *Journal of Electron Microscopy*, 53(3):167–171, 2002. 99

[113] R. Turan, D.D. Perovic, and D.C. Houghton. Mapping electrically active dopant profiles by field-emission scanning electron microscopy. *Appl. Phys. Lett.*, 69:1593–1595, 1996. 99

[114] D. Venables, H. Jain, and D.C. Collins. Seconday electron imaging as two-dimensional dopant profiling technique: Review and update. *J. of Vac. Sci. Technol. B*, 16(1):362–366, 1998. 99, 100

[115] E. Völkl and M. Lehmann. The reconstruction of off-axis electron holograms. In E. Völkl, L.F. Allard, and D.C. Joy, editors, *Introduction to Electron Holography*, page 125. Kluwer Academic / Plenum Publishers, New York, 1999. 30

[116] Y.C. Wang, T.M. Chou, M. Libera, and T.F. Kelly. Transmission electron holography of silicon nanospheres with surface oxide layers. *Appl. Phys. Lett.*, 70:1296–1298, 2001. 3, 29

[117] Z. Wang, T. Hirayama, K. Sasaki, H. Saka, and N. Kato. Electron holographic characterization of electrostatic potential distributions in a transistor sample fabricated by focused ion beam. *Appl. Phys. Lett.*, 80:246–248, 2002. 3

[118] U. Weierstall, J.C.H. Spence, M. Stevens, and K.H. Downing. Point-projection electron imaging of tobacco mosaic virus at 40 eV electron energy. *Micron*, 30:335–338, 1999. 4, 42

[119] J.K. Weiss, W.J. de Ruiter, M. Gajdardziska-Josifovska, M.R. McCartney, and D.J. Smith. Applications of electron holography to the study of interfaces. *Ultramicroscopy*, 50:301–311, 1993. 3

[120] D.B. Williams and C.B. Carter. *Transmission Electron Microscopy*, volume I Basics. Plenum Press, New York and London, 1996. 18

[121] D.B. Williams and C.B. Carter. *Transmission Electron Microscopy*, volume II Diffraction. Plenum Press, New York and London, 1996. 38

[122] F. Zhou. Coherence and incoherence of inelastically scattered electron waves. *Ultramicroscopy*, 92:293–304, 2002. 9, 12, 13, 104

Appendices

The software Digital Micrograph^{TM} by Gatan Inc. is commonly used in microanalysis laboratories for image acquisition, manipulation, and analysis. It also features an extensive scripting language, in which algorithms for image data manipulation can be programmed. The Holoworks software by Edgar Völkl used for the hologram reconstruction in this thesis, for instance, is written in this scripting language. A large number of Digital Micrograph^{TM} scripts, useful for the analysis and manipulation of electron holograms, has been written as part of this thesis, and a selection is listed in this appendix.

Fresnel Fringe Removal A

The following script is useful for removing Fresnel fringe artifacts from electron holograms. The script receives a hologram and a reference hologram as input images. Both holograms are Fourier transformed. The sideband is detected according to the preferences set in Holoworks. Then all pixels on a line between the center of Fourier space and the sideband are dampened using a Gaussian function, as discussed in section 2.9.1. The width of the dampened area and the strength of the attenuation can be altered using the four cursor keys. The distance from the dampened area to the center of the sideband can be changed using the "a" and "s" keys. After the corresponding pixels have been attenuated in both the Fourier transform of the hologram and the reference image, an inverse Fourier transform is applied and the real components are displayed. A record of the filter parameters is written to the image history. Some code written by Edgar Völkl has been incorporated into this script.

```
//********************************************************************************
// Provides a simple filter for removing Fresnel fringes
//
// Fourier transforms hologram and finds sideband in Fourier space
// allows user do damp Fresnel fringes and does an inverse Fourier transformation
//********************************************************************************

Image info, aperture, display, phaseImage, amplitudeImage, ampl,
number annot0, annot1, annot2, calibrate, sampleRateX, sampleRateY, TWS, ROd
number maxXD, maxYD, zoomD, topOval, leftOval, bottomOval, rightOval, sizeSidebandSmall
number centerCut, XYratio, XYratio2
number leftarrow, rightarrow, uparrow, downarrow, DMversion, orderButter
number rXinner, rYinner, rXouter, rYouter, deltaMaxX, deltaMaxY
number displayWindowSizeX, displayWindowSizeY, infoTextAnnotation
number posXFFT, posYFFT, windowSizeXFFT, windowSizeYFFT, scaleXF, scaleYF
number objectApproximationNumber, tab, finalzoom
number displayCenterX, displayCenterY
number finalSizeX, finalSizeY, Dx, Dy

string pixelsizeUnit, nr, typeOfAperture, objectApproximation, History, platform, UseProperScaling;
string displayPhaseImage, displayAmplitudeImage, displayComplexImage, UseUpperLowerSideband;
string pixelSizeUnitF, sidebandSearchAuto, hardAperture, UseHelpWindows;
string SubtractAverageH, UseAutomatedPhaseOffset, DisplayScaleMarks;

image frontHol, frontRef;
ComplexImage frontFHol;
number topHol, bottomHol, leftHol, rightHol;
number calibrateHol;

//
// Solve version issues:
//

GetPersistentNumberNote("Private:Configuration:ApplicationVersion", DMversion)
if( DMVersion < 340) Throw("Needs DigitalMicrograph version 3.4.0 or higher")
```

```
uparrow = 30; downarrow = 31; leftarrow = 28; rightarrow = 29;  tab = 9;
OpenResultsWindow();
Result("\n\Fresnel Remover   " + datestamp() + "\n");

//
// limiting parameters for aperture to be used:
//

number radiusLimitSelectionSizeFactor = 1/3; //1/3 of selection size; avoid bleeding between sidebands
number radiusLimitFinalImageSizeFactor = 0.7;//sqrt(2)/2  limit subsampling problems in final image

//
// Get (or define) basic reconstruction parameters:
//

if( !GetPersistentNumberNote( "Holography:size of reconstructed images", finalSizeParameter) );
        finalSizeParameter = 0.25;
if( !GetPersistentNumberNote( "Holography:size of centerCut", centerCut) );
        centerCut = 0.1;
if( !GetPersistentStringNote( "Holography:object approximation", objectApproximation ) );
        objectApproximation = "weak";
if( !GetPersistentStringNote( "Holography:Display phase image", displayPhaseImage) );
        displayComplexImage = "no";
if( !GetPersistentStringNote( "Holography:Display complex image", displayComplexImage) );
        displayComplexImage = "no";
if( !GetPersistentStringNote( "Holography:Display amplitude image", displayAmplitudeImage) );
        displayAmplitudeImage = "no";
if( !GetPersistentStringNote( "Holography:Use upper or lower sideband", UseUpperLowerSideband) );
        UseUpperLowerSideband = "upper";
if( !GetPersistentStringNote( "Holography:Use proper scaling if available", UseProperScaling) );
        UseProperScaling = "yes";
if( !GetPersistentStringNote( "Holography:Use help windows", UseHelpWindows) );
        UseHelpWindows = "yes";
if( !GetPersistentStringNote( "Holography:search sideband manually", sidebandSearchAuto) );
        sidebandSearchAuto = "yes";
if( !GetPersistentStringNote( "Holography:Subtract average from hologram", SubtractAverageH) );
        SubtractAverageH = "yes";
if( !GetPersistentStringNote( "Holography:Use automated phase offset", UseAutomatedPhaseOffset) );
        UseAutomatedPhaseOffset = "yes";
if( !GetPersistentStringNote( "Holography:Display scale marks", DisplayScaleMarks) );
        DisplayScaleMarks = "yes";

//
// Get front image basic data:
//

If (! GetTwoImagesWithPrompt("Image 1 = Hologram, Image 2 = Reference",
                             "Fresnel Remover", frontHol, frontRef))
  Exit(0);

zoom = GetZoom( frontRef );
GetWindowPosition( frontRef, posX, posY );
GetSelection( frontRef, top, left, bottom, right );
XYratio = (right-left)/(bottom-top);
GetSize(frontRef, sizeX, sizeY);
GetScreenSize( screenwidth, screenheight );
GetScale( frontRef, scaleX, scaleY);
pixelSizeUnit = GetUnitString( frontRef );
if(pixelSizeUnit != "")
calibrate = 1;

//
// Check X and Y direction for power of two
//

size = bottom - top;
while( size / 2 >= 1 )
    size = size/2;
if( size != 1 )
    Throw( "Only for images of the power of two!" );
```

```
size = right - left;
while( size / 2 >= 1 )
    size = size/2;
if( size != 1 )
    Throw( "Only for images of the power of two!" );

//
// Make sure final image is not smaller than 1 pixels in any direction
// this constraint can be modified any time
//

finalSizeX = (right - left) * finalSizeParameter;
finalSizeY = (bottom - top) * finalSizeParameter;
if( finalSizeX < 1 )
    Throw("A final image size of less than 1 pixels in any direction is not supported.");
if( finalSizeY < 1 )
    Throw("A final image size of less than 1 pixels in any direction is not supported.");

//
// Do Fourier transform, determine scaling parameters,
// one time use for "useProperScaling"
//

if(UseUpperLowerSideband == "upper")
    OpenAndSetProgressWindow( "Searching for:", "   upper sideband", "" );
else
    OpenAndSetProgressWindow( "Searching for:", "   lower sideband", "" );

frontF := RealFFT( frontRef[top, left, bottom, right] );

if(pixelSizeUnit != "")
{
    scaleXF = 1/( scaleX * (right - left) );
    scaleYF = 1/( scaleY * (bottom - top) );
    pixelSizeUnitF = "1/" + pixelSizeUnit;
    SetScale( frontF, scaleXF, scaleYF);
    SetUnitString( frontF, pixelsizeunitF);
}
else
    UseProperScaling = "no";


//
// find position of sideband from image tetra => (maxX, maxY)
//

centerCut = Trunc((right-left) * centerCut);
//number of pixels to be cut from center in x-direction;

tetra := frontF[ 0, 0, (bottom - top)/2+1, right-left ] + 0;
if(XYratio <= 1)
    tetra[  (bottom-top-centerCut)/2, (right-left-centerCut*XYratio)/2,\
            (bottom - top)/2+1, (right-left+centerCut*XYratio)/2 + 1 ] = 0;
else
    tetra[  (bottom-top-centerCut/XYratio)/2, (right-left-centerCut)/2,\
            (bottom - top)/2+1, (right-left+centerCut)/2 + 1 ] = 0;

tetra[ (bottom-top)/2, (right-left)/2, (bottom-top)/2+1, right-left ] = 0;

maximum = max( modulus( tetra ), maxX, maxY );
number emergency
if( (UseUpperLowerSideband == "lower" && maxX == 0) ||
    (UseUpperLowerSideband == "lower" && maxY == 0) )
{
    emergency = 1;
    UseUpperLowerSideband = "upper"
    Result("  sideband coincides with Nyquist frequency\n  => temporarily work with ''upper'' sideband")
}
if(UseUpperLowerSideband == "lower")
{
    maxX = (right-left) - maxX;
```

```
    maxY = (bottom-top) - maxY;
    Result("  Center of lower sideband found at (" + maxX + "," + maxY + ")\n");
}
else
    Result("  Center of upper sideband found at (" + maxX + "," + maxY + ")\n");
DeleteImage( tetra );


////////////////////////////////////////////////////////////////////////////////////
//                                                                                //
//  Position of upper or lower sideband detected as (maxX, maxY) in basic FFT (frontF)  //
//                                                                                //
////////////////////////////////////////////////////////////////////////////////////

//
// maxX and maxY are in reference to "frontF"  !
// maxXnew and maxYnew  are in reference to "display" !
// 1) create image for display
// 2) create info window
// 3) select position of sideband -> interactively
// 4) automatically (dependent on 3) )
//

if(UseUpperLowerSideband != "lower")
    display := log(modulus(frontF[0, 0, (bottom-top)*0.75, (right-left)]));
else
    display := log(modulus(frontF[(bottom-top)*0.25, 0, bottom-top, (right-left)]));
if( (right-left) > 4096 || (bottom - top) > 2048)
    zoomD = 0.125;
else
if( (right-left) > 2048 || (bottom - top) > 1024)
    zoomD = 0.25;
else
if( (right-left) > 1024 || (bottom - top) > 512)
    zoomD = 0.5;
else
if( (right-left) < 256 || (bottom - top) < 128)
    zoomD = 2;
else
    zoomD = 1;
setZoom(display, zoomD);
setName(display, "Select Sideband Position")
DisplayAt(display, posX + 14, posY + 21);
GetWindowSize(display, displayWindowSizeX, displayWindowSizeY)
maxXnew = maxX;
if(UseUpperLowerSideband != "lower")
    maxYnew = maxY;
else
    maxYnew = maxY - (bottom-top)*0.25;
displayCenterX = (right-left)/2;
displayCenterY = (bottom - top)*0.375;

if(sidebandSearchAuto != "yes")
{
SetSelection(display, maxYnew - 10, maxXnew - 10, maxYnew + 11, maxXnew + 11);
DoEvents();
if(UseHelpWindows == "yes")
{
    info := CreateFloatImage("info", 110, 160)
    info = 1;
    SetSurvey(info,0);
    SetLimits(info, 0,1);
    infoTextAnnotation = CreateTextAnnotation(info, 0, 0,
      "SELECT\nSIDEBAND :\n\narrow keys\nmove selection\n\nspace bar\ncontinues\nscript");
    SetAnnotationBackground(info, infoTextAnnotation, 1);
    SetAnnotationSize(info, infoTextAnnotation, 11);
    DisplayAt(info, posX + 26 + displayWindowSizeX, posY + 21);
    SetZoom(info, 1.1)              // necessary because of bug?
}
ShowImage(display);//(makes the image "display" the frontmost image)
key = 0;
```

```
ii = 0;
while(key != 32 && key != 13 && key != 3)// return, enter and spacebar keys
{
  key = GetKey();
  if(key == 0)
  {
    ii += 1;
    if(ii == 6)
    {
      if(UseUpperLowerSideband == "upper")
      {
         if(maxXNew == (right-left)/2 && maxYnew == (bottom-top)/2)
           OpenAndSetProgressWindow("Warning !", "autocorrelation selected!", "")
         else
           if(UseProperScaling == "no")
             OpenAndSetProgressWindow("center at:", "(" + maxXnew + "," + maxYnew + ")" ,\
             "I = " + exp(average(display[maxYnew, maxXnew, maxYnew+1, maxXnew+1])));
           else {
             OpenAndSetProgressWindow("center at: " + \
             Trunc(100000/  Sqrt( (((right-left)/2-maxXnew)*scaleXF)**2 + \
               (((bottom-top)/2-maxYnew)*scaleYF)**2 ) )/100000 + \
               " " + pixelSizeUnit, \
               "(" + maxXnew + "," + maxYnew + ")", \
               "I = " + exp(average(display[maxYnew, maxXnew, maxYnew+1, maxXnew+1])));
           }
      }
      else
      {
        if(maxXNew == (right-left)/2 && maxYnew == ((bottom-top)/2- (bottom-top)*0.25))
          OpenAndSetProgressWindow("Warning !", "autocorrelation selected!", "")
        else
          if(UseProperScaling == "no")
           OpenAndSetProgressWindow("center at:", "(" + maxXnew + "," + \
             (maxYnew+(bottom-top)*0.25) + ")" ,\
             "I = " + exp(average(display[maxYnew, maxXnew, maxYnew+1, maxXnew+1])));
           else
           {
             OpenAndSetProgressWindow("center at: " + \
             Trunc(100000/  Sqrt( (((right-left)/2-maxXnew)*scaleXF)**2 + \
               (( maxYnew - (bottom-top)/2 + \
               (bottom-top)*0.25 )*scaleYF)**2 ) )/100000 + " " + pixelSizeUnit, \
               "(" + maxXnew + "," + (maxYnew+(bottom-top)*0.25) + ")", \
               "I = " + exp(average(display[maxYnew, maxXnew, maxYnew+1, maxXnew+1])));
           }
      }
    }
    DoEvents();
  }
  else
  if(key == leftarrow)
  {
    if(maxXnew > 10) maxXnew += -1;
    if(maxYnew == ((bottom-top)/2 - (bottom-top)*0.25) && \
                  maxXnew < (right-left)/2 && UseUpperLowerSideband == "lower")
       maxYnew += 1;
    SetSelection(display, maxYnew - 10, maxXnew - 10, maxYnew + 11, maxXnew + 11);
    i = 0;
    DoEvents();
  }
  else
  if(key == rightarrow)
  // IF GOING ONTO THE RIGHT SIDE and at (bottom-top)/2, the selection
  // should jump up one pixel according to definition of upper sideband!
  {
    if(maxXnew < ((right-left)-11)) maxXnew += 1;
    if(maxYnew == (bottom-top)/2 && maxXnew > (right-left)/2 && \
                  UseUpperLowerSideband == "upper")
      maxYnew += -1;
    SetSelection(display, maxYnew - 10, maxXnew - 10, maxYnew + 11, maxXnew + 11);
    ii = 0;
    DoEvents();
```

```
  }
  else
  if(key == uparrow)
  {
    if(UseUpperLowerSideband == "lower")
    {
      if(maxYnew > ((bottom-top)/2 - (bottom-top)*0.25) && maxXnew >= (right-left)/2)
        maxYnew += -1;
      else
      {
        if(maxYnew > ((bottom-top)/2 + 1 - (bottom-top)*0.25) && maxXnew <= (right-left)/2)
          maxYnew += -1;
      }
    }
    else
    {
      if(maxYnew > 10) maxYnew += -1;
    }
    SetSelection(display, maxYnew - 10, maxXnew - 10, maxYnew + 11, maxXnew + 11);
    ii = 0;
    DoEvents();
  }
  else
  if(key == downarrow)
  {
    if(UseUpperLowerSideband == "lower")
    {
      if(maxYnew+11 < ((bottom-top) - (bottom-top)*0.25) )
        maxYnew += 1;
    }
    else
    {
      if(maxYnew < (bottom-top)/2 && maxXnew <= (right-left)/2 )
        maxYnew += 1;
      else
      {
        if(maxYnew < ((bottom-top)/2-1) && maxXnew >= (right-left)/2 )
          maxYnew += 1;
      }
    }
    SetSelection(display, maxYnew - 10, maxXnew - 10, maxYnew + 11, maxXnew + 11);
    ii = 0;
    DoEvents();
  }
  else
  if(key != 32 && key!= 13 && key != 3)
  {
    if(!TwoButtonDialog("Would you like to continue or exit the script:\n\n" + \
                        "'Reconstruct++.s'  ?\n ", "Cont", "exit"))
    {
       Result("aborted\n\n");
       Throw(-128);
    }
  }
}

if(UseUpperLowerSideband == "lower")
{
  if(maxX != maxXnew || maxY != (maxYnew + (bottom-top)*0.25) )
  {
    Result("    hand-selected at (" + maxXnew + "," + (maxYnew + (bottom-top)*0.25) + ")\n");
  }
}
else
{
  if(maxX != maxXnew || maxY != maxYnew )
  {
    Result("    hand-selected at (" + maxXnew + "," + maxYnew + ")\n");
  }
}
if(UseHelpWindows == "yes")
```

```
    DeleteImage(info);

//
//  Center new selection automatically?
//
//

if(UseUpperLowerSideband == "upper")
{
  if(maxXnew != maxX || maxYnew != maxY)
  {
    if(TwoButtonDialog("automatically center selection onto the maximum" + \
                       " value within the selection?","yes","no"));
    {
      maximum = exp(max( display[maxYnew-10, maxXnew-10, maxYnew+11, maxXnew+11], deltaMaxX, deltaMaxY ));
      maxX = maxXnew - 10 + deltaMaxX;
      maxY = maxYnew - 10 + deltaMaxY;
      maxXnew = maxX;
      maxYnew = maxY;
      SetSelection(display, maxYnew - 10, maxXnew - 10, maxYnew + 11, maxXnew + 11);
      OpenAndSetProgressWindow("center at:","(" + maxX + "," + maxY + ")" ,\
                               "I = " + exp(average(display[maxY, maxX, maxY+1, maxX+1])));
      DoEvents();
      Delay(8);
      Result("    final center at  (" + maxX + "," + maxY + ")\n")
    }
    else
    {
      maxX = maxXnew;
      maxY = maxYnew;
    }
  }
}
else
{
  if(maxXnew != maxX || (maxYnew + (bottom-top)*0.25 ) != maxY)
  {
    if(TwoButtonDialog("automatically center selection onto the maximum" + \
                       " value within the selection?","yes","no"));
    {
       maximum = exp(max( display[maxYnew-10, maxXnew-10, maxYnew+11, maxXnew+11], deltaMaxX, deltaMaxY ));
       maxX = maxXnew - 10 + deltaMaxX;
       maxY = maxYnew - 10 + deltaMaxY + (bottom-top)*0.25;
       maxXnew = maxX;
       maxYnew = maxY - (bottom-top)*0.25;
       SetSelection(display, maxYnew - 10, maxXnew - 10, maxYnew + 11, maxXnew + 11);
       OpenAndSetProgressWindow("center at:","(" + maxX + "," + maxY + ")" ,\
                                "I = " + exp(average(display[maxYnew, maxXnew, maxYnew+1, maxXnew+1])));
       DoEvents();
       Delay(8);
       Result("    final center at  (" + maxX + "," + maxY + ")\n")
    }
    else
    {
       maxX = maxXnew;
       maxY = maxYnew + (bottom-top)*0.25;
    }
  }
}
ClearSelection(display);
}


////////////////////////////////////////////////////////////////////////
//                                                                    //
//  Sideband is now found in Reference Hologram (maxX, maxY) in frontF    //
//  Now: Fourier Transform Hologram                                   //
//                                                                    //
////////////////////////////////////////////////////////////////////////

number sizeXHol, sizeYHol, scaleXHol, scaleyHol;
```

```
string pixelSizeUnitHol;

GetSelection( frontHol, topHol, leftHol, bottomHol, rightHol );
GetSize(frontHol, sizeXHol, sizeYHol);
GetScale( frontHol, scaleXHol, scaleYHol);
pixelSizeUnitHol = GetUnitString( frontHol );
if ( !(PixelSizeUnit == PixelSizeUnitHol) )
{
    OKDialog("Hologram and Reference must have same pixel size unit");
    Exit(0);
}
if ( !( (scaleX == scaleXHol) && (scaleY == scaleYHol) ) )
{
    OKDialog("Hologram and Reference must have same pixel size unit");
    Exit(0);
}
if(pixelSizeUnit != "")
    calibrateHol = 1;

if ( ! ( (sizeX==sizeXHol) && (sizeY==sizeYHol) ) )
{
    OKDialog("Hologram and Reference need to have same size");
    Exit(0);
}

//  Check X and Y direction for power of two

size = bottomHol - topHol;
while( size / 2 >= 1 )
    size = size/2;
if( size != 1 )
    Throw( "Only for images of the power of two!" );

size = right - left;
while( size / 2 >= 1 )
    size = size/2;
if( size != 1 )
    Throw( "Only for images of the power of two!" );

//
//  Make sure final image aren not smaller than 1 pixels in any direction
//  this constraint can be modified any time
//

finalSizeX = (rightHol - leftHol) * finalSizeParameter;
finalSizeY = (bottomHol - topHol) * finalSizeParameter;
if( finalSizeX < 1 )
    Throw("A final image size of less than 1 pixels in any direction is not supported.");
if( finalSizeY < 1 )
    Throw("A final image size of less than 1 pixels in any direction is not supported.");

//
//  Do Fourier transform after subtraction of image average,
//  determine scaling parameters,
//  one time use for "useProperScaling"
//

frontFHol := RealFFT( frontHol[top, left, bottom, right] );

if(pixelSizeUnit != "")
{
    SetScale( frontFHol, scaleXF, scaleYF);
    SetUnitString( frontFHol, pixelsizeunitF);
}

////////////////////////////////////////////////////////////////////////////
//                                                                        //
//  Now we did FT on Hologram                                             //
//                                                                        //
//  << Cut out Fresnel Fringes in Hologram >>                             //
//                                                                        //
```

```
////////////////////////////////////////////////////////////////////////

number mySizeX, mySizeY, mywidth=20, myZero=0, myoffset=0, mytop, myleft;
number Akey = 97, Skey = 115;
image mydisplay1, mydisplay2, mymask, fullmask;

mydisplay1 := modulus(frontFHol[Min(maxY, sizeY/2), Min(maxX, sizeX/2), \
                                Max(maxY, sizeY/2), Max(maxX, sizeX/2)]);
mysizeX = Abs(maxX-sizeX/2);
mysizeY = Abs(maxY-sizeY/2);

mymask := CreateFloatImage("Line Mask", mysizeX, mySizeY);
mymask = 1;
if (maxX<sizeX/2) // Sideband on left side
{
    if  (UseUpperLowerSideBand=="upper")
            mymask[myOffset*mySizeY/mySizeX, myOffset, mySizeY, mySizeX] = \
                    1-Exp(-(icol - irow*mySizeX/mySizeY)**2/mywidth-myzero);
    else
            mymask[0,myOffset,mySizeY-myOffset*mySizeY/mySizeX, mySizeX] = \
                    1-Exp(-(icol+myOffset + (irow-mySizeY)*mySizeX/mySizeY)**2/mywidth-myzero);
}
else                        // Sideband on right side
{
    if (UseUpperLowerSideBand=="upper")
            mymask[myOffset*mySizeY/mySizeX ,0, mySizeY, mySizeX-myOffset] = \
                    1-Exp(-(icol+myOffset + (irow-mysizeY)*mySizeX/mySizeY)**2/mywidth-myzero);
    else
            mymask[0,0, mySizeY-myOffset*mySizeY/mySizeX, mySizeX-myOffset] = \
                    1-Exp(-(icol - irow*mySizeX/mySizeY)**2/mywidth-myzero);
}
mydisplay2 = mydisplay1*mymask;
SetZoom(mydisplay2, 4);
SetName(mydisplay2, "Sideband of Hologram");
ShowImage(mydisplay2);
OpenAndSetProgressWindow("Filter Width: "+mywidth, "Filter Opacity: "+myZero, \
                         "Dist. to SB center: "+myOffset*Sqrt(1+(mySizeY/mysizeX)**2));

if(UseHelpWindows == "yes")
{
    info := CreateFloatImage("info", 110, 160)
    info = 1;
    SetSurvey(info,0);
    SetLimits(info, 0,1);
    infoTextAnnotation = CreateTextAnnotation(info, 0, 0,
        "Cut out\nFresnel Fringes:\n\narrow keys\n adapts selection\n\na and" + \
        " s keys\n selects region\n\nspace bar\ncontinues script");
    SetAnnotationBackground(info, infoTextAnnotation, 1);
    SetAnnotationSize(info, infoTextAnnotation, 11);
    DisplayAt(info, posX + 26 + displayWindowSizeX, posY + 21);
    SetZoom(info, 1.1)              // necessary because of bug?
}

key = 0;
while(key != 32 && key != 13 && key != 3)// return, enter and spacebar keys
{
    key = GetKey();
    if (key==uparrow || key==downarrow || key==leftarrow || key==rightarrow \
            || key==Akey || key==SKey)
    {
        if (key == downarrow)
        {
            if (mywidth <= 0.1) mywidth = Max(mywidth-0.01, 0.01);
            else if (mywidth <= 0.5) mywidth = mywidth-0.05;
            else if (mywidth <= 1.5) mywidth = mywidth-0.1;
            else if (mywidth <= 5.0) mywidth = mywidth-0.5;
            else if (mywidth <= 10) mywidth = mywidth-1;
            else if (mywidth <= 20) mywidth = mywidth-2;
            else if (mywidth <= 40) mywidth = mywidth-5;
            else mywidth = mywidth-10;
        }
```

```
        if (key == uparrow)
        {
            if (mywidth < 0.09999999) mywidth = mywidth+0.01;
            else if (mywidth < 0.4999) mywidth = mywidth+0.05;
            else if (mywidth < 1.4999) mywidth = mywidth+0.1;
            else if (mywidth < 5.0) mywidth = mywidth+0.5;
            else if (mywidth < 10) mywidth = mywidth+1;
            else if (mywidth < 20) mywidth = mywidth+2;
            else if (mywidth < 40) mywidth = mywidth+5;
            else mywidth = mywidth+10;
    }
    if (key == leftarrow)
        myZero = myZero + .05;
    if (key == rightarrow)
        myZero = Max(myZero = myZero-.05, 0);
    if (key == Skey)
        myOffset = Min(myOffset+1, mySizeX-2);
    if (key == Akey)
        myOffset = Max(myOffset-1, 0);
    mymask = 1;
    if (maxX<sizeX/2)
    {
        if  (UseUpperLowerSideBand=="upper")
            mymask[myOffset*mySizeY/mySizeX, myOffset, mySizeY, mySizeX] = \
                  1-Exp(-(icol - irow*mySizeX/mySizeY)**2/mywidth-myzero);
        else
            mymask[0,myOffset,mySizeY-myOffset*mySizeY/mySizeX, mySizeX] = \
                  1-Exp(-(icol+myOffset + (irow-mySizeY)*mySizeX/mySizeY)**2/mywidth-myzero);
    }
    else
    {
        if (UseUpperLowerSideBand=="upper")
            mymask[myOffset*mySizeY/mySizeX ,0, mySizeY, mySizeX-myOffset] = \
                   1-Exp(-(icol+myOffset + (irow-mysizeY)*mySizeX/mySizeY)**2/mywidth-myzero);
        else
            mymask[0,0, mySizeY-myOffset*mySizeY/mySizeX, mySizeX-myOffset] = \
                   1-Exp(-(icol - irow*mySizeX/mySizeY)**2/mywidth-myzero);
    }
    mydisplay2 = mydisplay1*mymask;
    UpdateImage(mydisplay2);
    OpenAndSetProgressWindow("Filter Width: "+mywidth, "Filter Opacity: "+myZero, \
                             "Dist. to SB center: "+myOffset*Sqrt(1+(mySizeY/mysizeX)**2));
  }
}
if (maxX<sizeX/2)
    myleft = Nearest(maxX+myOffset);
else
    myleft = Nearest(sizeX-maxX+myOffset);
if (UseUpperLowerSideBand=="upper")
    mytop = Nearest(maxY+myOffset*mySizeY/mySizeX);
else
    mytop = Nearest((sizeY-maxY)+myOffset*mySizeY/mySizeX);

fullMask := CreateFloatImage("Full Mask", sizeX-2*myleft, sizeY-2*mytop);

if ( ((maxX<sizeX/2) && (UseUpperLowerSideband=="upper")) || \
                        ((maxX>sizeX/2) && (UseUpperLowerSideband=="lower")) )
    fullMask = 1-Exp(-(icol - irow*mySizeX/mySizeY)**2/mywidth-myzero);
else
    fullMask = 1-Exp(-(icol + (irow-sizeY+2*mytop)*mySizeX/mySizeY)**2/mywidth-myzero);
frontFHol[mytop, myleft, sizeY-mytop, sizeX-myleft] = \
    frontFHol[mytop, myleft, sizeY-mytop, sizeX-myleft] * fullMask;
DeleteImage(mydisplay1); DeleteImage(mydisplay2);
DeleteImage(FullMask);
if(UseHelpWindows == "yes") DeleteImage(info);
Result("Fresnel Fringes removed from Hologram with");
Result("\n  Filter Width: "+mywidth+", Filter Opacity: "+myZero+", \
       Dist. to SB center: "+myOffset*Sqrt(1+(mySizeY/mysizeX)**2) );
```

```
////////////////////////////////////////////////////////////////////////////////
//                                                                            //
//      Fringes are now erased from FT image (hologram).                      //
//      Now erase them from reference hologram.                               //
//                                                                            //
//                                                                            //
////////////////////////////////////////////////////////////////////////////////

mydisplay1 := modulus(frontF[Min(maxY, sizeY/2), Min(maxX, sizeX/2), \
                             Max(maxY, sizeY/2), Max(maxX, sizeX/2)]);
mysizeX = Abs(maxX-sizeX/2);
mysizeY = Abs(maxY-sizeY/2);

mydisplay2 = mydisplay1*mymask;
SetZoom(mydisplay2, 4);
SetName(mydisplay2, "Sideband of Reference");
ShowImage(mydisplay2);
OpenAndSetProgressWindow("Filter Width: "+mywidth, "Filter Opacity: "+myZero, \
                         "Dist. to SB center: "+myOffset*Sqrt(1+(mySizeY/mysizeX)**2));

if(UseHelpWindows == "yes")
{
    info := CreateFloatImage("info", 110, 160)
    info = 1;
    SetSurvey(info,0);
    SetLimits(info, 0,1);
    infoTextAnnotation = CreateTextAnnotation(info, 0, 0,
      "Cut out\nFresnel Fringes:\n\narrow keys\n adapts selection\n\na and" + \
      " s keys\n selects region\n\nspace bar\ncontinues script");
    SetAnnotationBackground(info, infoTextAnnotation, 1);
    SetAnnotationSize(info, infoTextAnnotation, 11);
    DisplayAt(info, posX + 26 + displayWindowSizeX, posY + 21);
    SetZoom(info, 1.1)              // necessary because of bug?
}

key = 0;
while(key != 32 && key != 13 && key != 3)// return, enter and spacebar keys
{
    key = GetKey();
    if (key==uparrow || key==downarrow || key==leftarrow || key==rightarrow \
                     || key==Akey || key==SKey)
    {
    if (key == downarrow)
    {
        if (mywidth <= 0.1) mywidth = Max(mywidth-0.01, 0.01);
        else if (mywidth <= 0.5) mywidth = mywidth-0.05;
        else if (mywidth <= 1.5) mywidth = mywidth-0.1;
        else if (mywidth <= 5.0) mywidth = mywidth-0.5;
        else if (mywidth <= 10) mywidth = mywidth-1;
        else if (mywidth <= 20) mywidth = mywidth-2;
        else if (mywidth <= 40) mywidth = mywidth-5;
            else mywidth = mywidth-10;
     }
     if (key == uparrow)
     {
        if (mywidth < 0.09999999) mywidth = mywidth+0.01;
        else if (mywidth < 0.4999) mywidth = mywidth+0.05;
        else if (mywidth < 1.4999) mywidth = mywidth+0.1;
        else if (mywidth < 5.0) mywidth = mywidth+0.5;
        else if (mywidth < 10) mywidth = mywidth+1;
        else if (mywidth < 20) mywidth = mywidth+2;
        else if (mywidth < 40) mywidth = mywidth+5;
        else mywidth = mywidth+10;
      }
      if (key == leftarrow)
        myZero = myZero + .05;
      if (key == rightarrow)
        myZero = Max(myZero = myZero-.05, 0);
      if (key == Skey)
        myOffset = Min(myOffset+1, mySizeX-2);
```

```
      if (key == Akey)
        myOffset = Max(myOffset-1, 0);

      mymask = 1;
      if (maxX<sizeX/2)
      {
            if  (UseUpperLowerSideBand=="upper")
                mymask[myOffset*mySizeY/mySizeX, myOffset, mySizeY, mySizeX] = \
                      1-Exp(-(icol - irow*mySizeX/mySizeY)**2/mywidth-myzero);
            else
                mymask[0,myOffset,mySizeY-myOffset*mySizeY/mySizeX, mySizeX] = \
                      1-Exp(-(icol+myOffset + (irow-mySizeY)*mySizeX/mySizeY)**2/mywidth-myzero);
      }
      else
      {
            if (UseUpperLowerSideBand=="upper")
                  mymask[myOffset*mySizeY/mySizeX ,0, mySizeY, mySizeX-myOffset] = \
                        1-Exp(-(icol+myOffset + (irow-mysizeY)*mySizeX/mySizeY)**2/mywidth-myzero);
             else
                  mymask[0,0, mySizeY-myOffset*mySizeY/mySizeX, mySizeX-myOffset] = \
                        1-Exp(-(icol - irow*mySizeX/mySizeY)**2/mywidth-myzero);
      }
      mydisplay2 = mydisplay1*mymask;
      UpdateImage(mydisplay2);
      OpenAndSetProgressWindow("Filter Width: "+mywidth, "Filter Opacity: "+myZero, \
                              "Dist. to SB center: "+myOffset*Sqrt(1+(mySizeY/mysizeX)**2));
  }

}
if (maxX<sizeX/2)
    myleft = Nearest(maxX+myOffset);
else
    myleft = Nearest(sizeX-maxX+myOffset);
if (UseUpperLowerSideBand=="upper")
    mytop = Nearest(maxY+myOffset*mySizeY/mySizeX);
else
    mytop = Nearest((sizeY-maxY)+myOffset*mySizeY/mySizeX);

fullMask := CreateFloatImage("Full Mask", sizeX-2*myleft, sizeY-2*mytop);

if ( ((maxX<sizeX/2) && (UseUpperLowerSideband=="upper")) || \
     ((maxX>sizeX/2) && (UseUpperLowerSideband=="lower")) )
    fullMask = 1-Exp(-(icol - irow*mySizeX/mySizeY)**2/mywidth-myzero);
else
    fullMask = 1-Exp(-(icol + (irow-sizeY+2*mytop)*mySizeX/mySizeY)**2/mywidth-myzero);

frontF[mytop, myleft, sizeY-mytop, sizeX-myleft] = \
    frontF[mytop, myleft, sizeY-mytop, sizeX-myleft] * fullMask;

DeleteImage(mydisplay1); DeleteImage(mydisplay2);
DeleteImage(myMask); DeleteImage(FullMask);
DeleteImage(display);
if(UseHelpWindows == "yes")     DeleteImage(info);
Result("\nFresnel Fringes removed from Reference Image with");
Result("\n  Filter Width: "+mywidth+", Filter Opacity: "+myZero+", \
       Dist. to SB center: "+myOffset*Sqrt(1+(mySizeY/mysizeX)**2) );

image frontFF := CreateFloatImage(GetName(frontRef)+"-FF", sizeX, sizeY);
frontFF = Real(IFFT(frontF));
SetScale( frontFF, scaleX, scaleY);
SetUnitString( frontFF, pixelsizeunit);

CopyHistoryHW2(frontRef, frontFF);
AddStringToList(frontFF, "History", "Fresnel Fringe Filter:");
AddStringToList(frontFF, "History", "  FFT - erase Fresnel fringes - IFFT");
AddStringToList(frontFF, "History", "  Fresnel Filter width = "+mywidth+", Opacity = "+myZero+",")
AddStringToList(frontFF, "History", "    Distance to sideband center = " + \
                myOffset*Sqrt(1+(mySizeY/mysizeX)**2));

ShowImage(frontFF);
DeleteImage(frontF);
```

```
image frontFFHol := CreateFloatImage(GetName(frontHol)+"-FF", sizeX, sizeY);
frontFFHol = Real(IFFT(frontFHol));
SetScale( frontFFHol, scaleX, scaleY);
SetUnitString( frontFFHol, pixelsizeunit);

CopyHistoryHW2(frontHol, frontFFHol);
AddStringToList(frontFFHol, "History", "Fresnel Fringe Filter:");
AddStringToList(frontFFHol, "History", "  FFT - erase Fresnel fringes - IFFT");
AddStringToList(frontFFHol, "History", "  Fresnel Filter width = "+mywidth+", Opacity = "+myZero+",")
AddStringToList(frontFFHol, "History", "    Distance to sideband center = " + \
               myOffset*Sqrt(1+(mySizeY/mysizeX)**2));

ShowImage(frontFFHol);
DeleteImage(frontFHol);
Result("\n\n");
CloseProgressWindow();
```

B Thickness Correction

As discussed in section 6.2.1 the amplitude image can be used to create a thickness map of the sample. The following script accomplishes this talk. To this end the script processes a reconstructed amplitude and phase image. For normalization purposes a rectangular area in the amplitude image has to be selected. In addition to this an area in the phase image, in which no other potentials except the inner potential contribute to the phase shift, has to be marked. The constant $K = 2C_E V_0 \lambda_{\text{inel}}$, which was introduced in section 6.2.1, is calculated by minimizing the difference between the thickness map obtained from the phase image and the thickness map obtained from the amplitude image in the marked area. A thickness map is then calculated. Finally the thickness contribution is subtracted from the phase image, and the result is displayed on the screen.

```
number count = 0
number Max   = 400
number step  = .05
number const = 1E-10

image  ampl, phas, shiftedphas, elpot, logAmpl, minphase
number top, left, bottom, right, sizeX, sizeY, stop, sleft, sbottom, sright, val
number minConst = 1E100
number min = 1E100

if ( !GetTwoImagesWithPrompt("Amplitude = image0 (with selected area), " + \
                             "phase = image1","Electrostatic Potential", ampl, phas) )
  exit(0)
if ( !GetSelection( ampl, top, left, bottom, right ) )
{
  OkDialog("Please select a vacuum area in the amplitude image first !")
  exit(0)
}
if ( !GetSelection( phas, stop, sleft, sbottom, sright ) )
{
  OkDialog("Make selection in the phase image first!")
  exit(0)
}

logAmpl = - log(ampl / average( ampl[top, left, bottom, right] ) )

shiftedphas = phas - average( phas[top, left, bottom, right] )
SetName(shiftedphas, "Phase with Offset Removed")

image plot := RealImage("Find Constant c at  Minimum",4,Max+1,1)
SetDisplayType( plot, 4 )             // line plot image display style
CreateTextAnnotation(plot, 5,5,"phase = - c * log(A/Ao)")
ImageSetDimensionCalibration(plot, 0, const, step, "rad", 1)

while (count <Max)
{
  count++
  elpot = shiftedphas - (const * logAmpl)
```

```
  val = Integrate(abs(elpot[stop, sleft, sbottom, sright])) / ((sright-sleft)*(sbottom-stop))
  plot[count,0] = val
  if (val < min)
  {
    min = val
    minConst = const
  }
  const += step
}

minphase = shiftedphas - minConst * logAmpl
SetName(minphase, "Phase Image at Minimum")
ShowImage(minphase)
ShowImage(plot)

DeleteImage(shiftedphas)
DeleteImage(elpot)
DeleteImage(logAmpl)

Result("\n\n")
Result("The constant c at the minimum is ")
Result(minConst)
Result(" rad")
Result("\n")
```

Removal of Linear Phase Changes

C

Thickness changes over the field of view are often linear in good approximation. In order to remove these linear contributions to the phase image, the following script can be very helpful. A line-profile in the direction of the linear phase increase is marked on the phase image. The script fits a line to this line-profile and subtracts the corresponding linear increase from the phase image.

```
image profile1;
image frontimage, newimage;

number sizeX, sizeY;            // Image size
number io, is, xs,ox, count;    // Intensity origin and scale, x origin and scale
number m,b, sx, sy, sxx, sxy;   // slope and axis offset, sums
number p1x1, p1y1, p1x2, p1y2;  // position of line profile1 in frontimage
number d1x, d1y;
string name;

if ( !GetTwoImagesWithPrompt("Image one = Unwrapped phase image. \n Image two = line profile", \
                                        "Sample thickness correction", frontimage, profile1) )
  exit(0);

GetSize(profile1, sizeX, sizeY);

io = ImageGetIntensityOrigin(profile1);
is = ImageGetIntensityScale(profile1);
xs = ImageGetDimensionScale(profile1,0);
ox = ImageGetDimensionOrigin(profile1,0);
name = Getname(frontimage);

GetAnnotationRect(frontimage, GetNthAnnotationID(frontimage, 0),\
                                  p1y1, p1x1, p1y2, p1x2);

count = 0;
sxy = 0;
sxx = 0;
sx  = 0;
sy  = 0;

while (count<sizeX)
{
  sxy = sxy + (GetPixel(profile1, count,0)+io)*is * (ox+count*xs);
  sy  = sy  + (GetPixel(profile1, count,0)+io)*is;
  sx  = sx  + (ox+count*xs);
  sxx = sxx + ((ox+count*xs)*(ox+count*xs));
  count++;
}

m = ( sizeX*sxy - sx*sy)/(sizeX*sxx - sx*sx);
b = (sy-m*sx)/sizeX;

Result("\n y="+m+"*x+"+b+"\n");

d1x = p1x2-p1x1;
d1y = p1y2-p1y1;
```

```
newimage =  frontimage - \
  (d1x*(icol-p1x1) + d1y*(irow-p1y1)) * m * sizeX / (d1x*d1x+d1y*d1y) - b;
SetName(newImage, name+" w/o plane");
ShowImage(newimage);
```

Index D

Aharonov-Bohm effect, 27
aperture function, 30

band model, 80
biprism, 20
branching, 37
brightness, 17
Butterworth filter, 30

CBED, 86
Cittert-Zernike theorem, 10
coherence, 9
    inelastic scattering, 12
    moving fringes, 15
    spatial, 10
    temporal, 10
coherent current, 17
cold field emission, 17
convergent beam electron diffraction, 86
curtaining, 75

de-layering, 70
dead layer, 84
depletion layer, 81
dielectric loss function, 53
differential thinning, 75
diffraction, 38
dimpling, 72
dual beam systems, 74

e-beam etching, 102
EELS, 88
elastic backscattering, 51
electron energy loss spectroscopy, 88
electron sources, 17
elliptic illumination, 17

epoxy, 71
extended Schottky emission, 20

FE-LMI, 74
Fermi level, 80
FIB, 74
    curtaining, 75
    differential thinning, 75
    dual beam systems, 74
    low voltage milling, 77
    platinum deposition, 75
    waterfall, 75
field emission, 17
field emission from superconductors, 103
field emission liquid metal ion source, 74
focused ion beam, *see* also FIB, 74
Fowler-Nordheim equation, 18
Fresnel diffraction, 36
Fresnel fringes, 36
Fresnel integral, 37
fringe branching, 37
fringe contrast, 8
fringe spacing, 7

HF-2000, 61
hologram, 7
    empty, 6
    fringe spacing, 7
    off-axis, 6
    reconstruction, 30
    recording, 32
Howie-Whelan equations, 39

in-line hologram formation, 43
index of refraction, 28
inelastic mean free path, 52

inner potential, 28
ion polishing, 72, 73

lapping, 71
low magnification holography, 63
low voltage milling, 77

medium magnification holography, 64
Monte Carlo simulation, 51

n doping, 81
n-doped silicon selective etch, 71

optimum thickness, 68

p doping, 81
packaging removal, 70
phase jumps, 31
phase resolution, 34
phase shift
    electric potentials, 27
    electro-magnetic fields, 26
    magnetic flux, 27
phase unwrap, 31
PIPS, 72, 73
plate biprism, 22
platinum deposition, 75
pn-junction, 80
point projection microscope, 41
polishing, 71
poly siliocn removal, 70
PPM, 41

reconstruction
    in-line hologram, 46
    off-axis hologram, 30
reference hologram, 31
removal of
    packaging, 70
    poly silicon, 70
    silicides, 71
    silicon oxide, 70
    tungsten, 70
resolution of small details, 32

sample
    dimpling, 72
    FIB, 74
    geometrical limitations, 69
    optimum thickness, 68
    surface amorphization, 70, 75
    tripod polishing, 71
Schottky emission, 20
Schrödinger's equation, 25
sideband, 30
silicide removal, 71
silicon oxide removal, 70
step junction, 80
surface amorphization, 70, 75

thermal field emission, 20
thickness correction, 84
tripod polishing, 71
tungsten removal, 70
two-beam condition, 38

waterfall, 75
WKB approximation, 18, 26

Young's double slit, 42

Vita

Alexander Thesen was born in Trier, Germany on January 8, 1976. After completing the elementary school, he attended the Stefan-George Gymnasium in Bingen with English as his first foreign language, Latin as his second, and French as a third foreign language. His main subjects in the last three years before graduation were Physics, Mathematics, and English. He was awarded first prizes in the competition "Jugend forscht" twice in 1993 and 1995 and also received a first prize in the competition "Jugend musiziert" in 1995. He graduated best of his year with a 4.0 GPA in 1995.

In the same year Alexander Thesen continued his education at the Johannes-Gutenberg University in Mainz, Germany majoring in physics. Apart from the standard physics curriculum he attended extra curricular Japanese and computer classes. In summer 1996 he participated as an intern in an experiment on the determination of the neutrino rest mass at the Institute of Physics in Mainz. The student body elected him into the department council of the Physics Department in 1996. In 1997 he was employed as an assistant to Prof. Drechsel at the Institute of Nuclear Physics in Mainz. During this year Alexander Thesen also passed his pre-diploma examination with an overall grade of "very good with distinction". This success was followed by his acceptance into the German National Merit Foundation (Studienstiftung des Deutschen Volkes).

In the following year Alexander Thesen received a Fulbright Scholarship to continue his studies at the University of Tennessee in Knoxville, USA for one year. His decision to remain at the University of Tennessee in order to pursue the full Ph.D. program was honored by the Physics Department with the "UT-ORNL Select Graduate Fellowship for an Outstanding Applicant in Condensed Matter Physics" in 1999. Although initially conducting his thesis work in surface science with Prof. Plummer, he continued his reaseach in the field of electron microscopy with Prof. David Joy in 2001. His thesis work focussed primarily on two-dimensional dopant profiling with electron holography and the design of a point projection and reflection microscope. In summer 2001 Alexander Thesen interned four months with Advanced Micro Devices in California working on device metrology. His research was recognized in 2002 with a first place student poster award of the Microscopy Society of America. Alexander Thesen has published research papers in Ultramicroscopy and the Journal of Vacuum Science and Technology as well as contributed papers to several conferences. He has maintained close ties to the semiconductor industry and presented his work at two international SEMATECH lab manager meetings.

Alexander Thesen is planning to graduate from the University of Tennessee in Spring 2003 with a Ph.D. degree in Physics.